AEOLIAN SEDIMENT AVAILABILITY AND TRANSPORT

BAS HOONHOUT

ISBN: 978-94-6332-152-5

AEOLIAN SEDIMENT AVAILABILITY AND TRANSPORT

PROEFSCHRIFT

ter verkrijging van de graad van doctor
aan de Technische Universiteit Delft,
op gezag van de Rector Magnificus prof. ir. K.Ch.A.M. Luyben;
voorzitter van het College voor Promoties,
in het openbaar te verdedigen op
vrijdag 24 maart 2017 om 12:30 uur.

door

Bastiaan Martin HOONHOUT
civiel technisch ingenieur, TU Delft
geboren te Amsterdam

This dissertation has been approved by the promotor prof. dr. ir. M.J.F. Stive and copromotor dr. ir. S. de Vries.

Composition of the doctoral committee:

Rector Magnificus	Chairman
prof. dr. ir. M.J.F. Stive	Delft University of Technology
dr. ir. S. de Vries	Delft University of Technology

Independent members:

prof. dr. ir. A.J.H.M. Reniers	Delft University of Technology
prof. dr. ir. A.W. Heemink	Delft University of Technology
prof. dr. ir. J.A. Roelvink	UNESCO-IHE
prof. dr. ir. B.G. Ruessink	Utrecht University
dr. P. Ruggiero	Oregon State University
prof. dr. ir. S.G.J. Aarninkhof	Delft University of Technology, reserve member

Dr. ir. J. S. M. van Thiel de Vries has contributed as supervisor greatly to the design and realization of this research.

This research was funded by the ERC-Advanced Grant 291206 – Nearshore Monitoring and Modeling (NEMO) and Deltares.

CONTENTS

DEFINITIONS

WIND TRANSPORT CAPACITY [kg/m/s] Transport capacity of the wind over an idealized bed. The wind transport capacity is an upper limit of the (sediment) transport capacity that includes the influence of bed surface properties.

(SEDIMENT) TRANSPORT CAPACITY [kg/m/s] Transport capacity of the wind over a given bed. The (sediment) transport capacity accounts for the impact velocity threshold. The (sediment) transport capacity is an upper limit of the actual sediment transport.

EQUILIBRIUM SEDIMENT TRANSPORT Sediment transport capacity.

SATURATED SEDIMENT TRANSPORT Sediment transport capacity.

VELOCITY THRESHOLD [kg/m/s] Impact velocity threshold at which sediment transport is sustained over a given bed. The threshold depends on bed surface properties that may hamper saltation, e.g. roughness, moist, salt, and represents the difference between the wind and (sediment) transport capacity.

SEDIMENT AVAILABILITY [kg/m^2] Sediment currently available for entrainment (following Kocurek and Lancaster, 1999). The sediment availability includes the fluid velocity threshold at which sediment transport is initiated. Sediment availability may result in sediment supply if wind is sufficient.

SEDIMENT ENTRAINMENT [kg/m^2/s] Entrainment of currently available sediment by the wind and contributing to the sediment supply.

SEDIMENT SUPPLY [kg/m/s] Transport of entrained sediment from one location to another, e.g. from marine sources to intertidal beach or from intertidal beach to dunes.

TRANSPORT-LIMITED Transport is determined by the wind transport capacity. An increase in wind speed will result in an increase in sediment transport as long as sediment is still available. If insufficient sediment is available, the coastal system becomes availability-limited.

AVAILABILITY-LIMITED Transport is determined by the availability of aeolian sediment. An increase in wind speed will not result in an increase in sediment transport as no additional sediment is available. A decrease in wind speed can result in a transport-limited coastal system as the sediment availability might be able to fulfill the demand from the reduced wind.

SUPPLY-LIMITED Availability-limited.

FETCH-LIMITED Transport is determined by the available fetch and therefore a wider beach or more oblique wind will result in an increase in sediment transport. In

this thesis fetch is only considered a limiting factor on an idealized bed with maximum sediment availability (i.e. flat, dry, loose and homogeneous). The coastal system is considered fetch-limited if and only if the available fetch is shorter than the fetch necessary for the development of a saturated saltation cascade in these idealized conditions. In all other cases where the available fetch influences the sediment transport, the coastal system is considered availability-limited.

SEDIMENT SORTING Spatial sorting of (sandy) sediment, either horizontally or vertically, due to differences in (sediment) transport capacity between sediment fractions.

BEACH ARMORING Emergence of non-erodible roughness elements from the bed that shelter (sandy) sediment from wind erosion, resulting in spatiotemporal differences in sediment availability.

SAND MOTOR Artificial sandy 21 Mm^3 mega nourishment constructed along the Delfland coast in 2011 with the purpose to feed the entire Dutch coast for two decades. *Dutch: Zandmotor*.

SAND ENGINE Sand Motor.

ACRONYMS

2DH	Two-Dimensional in a Horizontal plane
2DV	Two-Dimensional in a Vertical plane
ATV	All-Terrain Vehicle
AEOLIS	Aeolian sediment transport with Limited Supply
BMI	Basic Model Interface
DN	Deployment Number
KNMI	Koninklijk Nederlands Meteorlogisch Instituut
MCMC	Markov Chain Monte Carlo
MSL	Mean Sea Level
MEGAPEX	Mega Peturbation EXperiment
NEMO	Nearshore Modeling and Monitoring
R^2	R-squared or Coefficient of Determination
RMSE	Root Mean Square Error
RTK-GPS	Real-Time Kinematic Global Positioning System

Symbol	Units	Description
α	-	Factor to convert from wind velocity to shear velocity.
β	-	Ratio between drag coefficients of bare surface and roughness elements.
θ_u	-	Wind direction.
Γ	-	Implicitness parameter.
γ	-	Maximum wave height over depth ratio.
ζ	-	Bed interaction factor.
η	m+MSL	Still water level.
$\hat{\eta}$	m+MSL	Local water level.
κ	-	Von Kármán constant.
λ	-	Roughness density.
ξ	-	Surf similarity parameter.
ρ_a	kg/m^3	Air density.
ρ_p	kg/m^3	Grain density.
ρ_w	kg/m^3	Water density.
σ	-	Ratio between surface area and frontal area of roughness elements.
Φ	kg/m/s	Space-integrated entrainment function.
ϕ	$kg/m^2/s$	Entrainment function.
Ψ	kg/s	Sediment transport potential.
A	-	Empirical coefficient.
A_c	m^2	Surface area of control area.
C	-	Empirical coefficient to account for grain size distribution width.
C_c	kg/m^3	Sediment concentration in the air as used by de Vries et al. (2014b). Relates to c as $c = hC_c$.
c	kg/m^2	Sediment concentration in the air.
c_{sat}	kg/m^2	Saturated sediment concentration in the air.
D	kg/m^2	Total deposition.
D_n	m	Reference median grain size (250 μm).
d	m	Water depth.
d_{50}	m	Median grain size.
d_n	m	Nominal grain size.
E	kg/m^2	Total erosion.
E_v	m/s	Evaporation rate.
F	m	Available fetch.
$\hat{F}$	m	Effective fetch.
F_c	m	Critical fetch.
$f_{\Delta z_d}$	-	Depth of disturbance factor.

Symbol	Units	Description (continued)
f_{θ_u}	-	Factor to include wind direction in sediment transport capacity.
$f_{u_{*th},M}$	-	Factor to include the influence of moisture to the shear velocity threshold u_{*th}.
$f_{u_{*th},R}$	-	Factor to include the influence of roughness elements to the shear velocity threshold u_{*th}. Relates to R_t as $R_t = \frac{1}{f_{u_{*th},R}}$.
$f_{u_{*th},S}$	-	Factor to include the influence of salt to the shear velocity threshold u_{*th}.
g	m/s^2	Gravitational constant.
H	m	Offshore wave height.
$\hat{H}$	m	Local wave height.
h	m	Height of saltation layer.
i	-	Cross-shore grid index.
j	-	Alongshore grid index.
K^+	-	Hydrodynamic addition mask.
$K^\times$	-	Hydrodynamic multiplication mask.
k	-	Grain size fraction index.
k_0	-	Index of smallest non-erodible grain size fraction.
l	-	Diagonal index.
m	-	Factor to account for difference between mean and maximum shear stress.
m_a	kg/m^2	Sediment availability.
n	-	Time step index.
n_k	-	Number of grain size fractions.
n_{pc}	-	Number of counted particles.
n_x	-	Number of grid cells in cross-shore direction.
n_y	-	Number of grid cells in alongshore direction.
p	-	Porosity.
p_g	kg/kg	Geotechnical mass content of water.
p_s	mg/g	Salt content.
p_V	m^3/m^3	Volumetric water content.
Q	m^3	Cumulative sediment transport capacity.
q	kg/m/s	Sediment transport rate.
q_{sat}	kg/m/s	Saturated sediment transport rate.
R	m	Wave runup height.
R_t	-	Ratio between velocity threshold on bare surface $u_{*th,S}$ and on surface including roughness elements $u_{*th,R}$.
S_k	-	Degree of saturation of grain size fraction k.
$\hat{S}_k$	-	Effective degree of saturation of grain size fraction k, including the bed interaction parameter ζ.
T	s	Adaptation time scale in advection equation.
t	s	Time.
Δt^n	s	Size of time step n.
u_*	m/s	Shear velocity.
u_z	m/s	Wind velocity at height z.

Symbol	Units	Description (continued)
$u_{*th,R}$	m/s	Shear velocity threshold of surface including roughness elements.
$u_{*th,S}$	m/s	Shear velocity threshold of bare surface.
u_{*th}	m/s	Shear velocity threshold.
u_{th}	m/s	Wind velocity threshold.
$u_{z,x}$	m/s	Wind velocity component in x-direction and at height z.
$u_{z,y}$	m/s	Wind velocity component in y-direction and at height z.
V	m^3	Sediment volume.
$V_{40\%}$	m^3	Sediment volume normalized to 40% porosity.
ΔV^n	m^3	Change in sediment volume in time step n.
w_k	-	Weighting factor for grain size fraction k in right-hand-side of the advection equation.
w_k^{air}	-	Weighting factor for grain size fraction k based on the grain size distribution in the air.
w_k^{bed}	-	Weighting factor for grain size fraction k based on the grain size distribution in the bed.
x	m	Cross-shore distance.
$\Delta x_{i,j}$	m	Size of grid cell i,j in cross-shore direction.
y	m	Alongshore distance.
$\Delta y_{i,j}$	m	Size of grid cell i,j in alongshore direction.
z	m	Height above the bed.
z'	m	Thickness of inner boundary layer.
z_b	m+MSL	Bed level.
Δz_d	m	Depth of disturbance.

LIST OF FIGURES

LIST OF TABLES

ABSTRACT

This thesis explores the nature of aeolian sediment availability and its influence on aeolian sediment transport. The aim is to improve large scale and long term aeolian sediment transport estimates in (nourished) coastal environments. The generally poor performance of aeolian sediment transport models with respect to measurements in coastal environments is often accredited to limitations in sediment availability. Sediment availability can be limited by particular properties of the bed surface. For example, if the beach is moist or covered with non-erodible elements, like shells. If sediment availability is limited, the aeolian sediment transport rate is governed by the sediment availability rather than the wind transport capacity.

Aeolian sediment availability is rather intangible as sediment availability is not only affected by aeolian processes, but also by marine and meteorological processes that act on a variety of spatial and temporal scales. The Sand Motor 21 Mm^3 mega nourishment is used to quantify the spatiotemporal variations in aeolian sediment availability and its effect on aeolian sediment transport. The Sand Motor was constructed in 2011 along the Dutch coast. Aeolian sediment accumulation in the Sand Motor region is low compared to the wind transport capacity, while the Sand Motor itself is virtually permanently exposed to wind and accommodates large fetches. Aeolian sediment availability is therefore likely to dominate aeolian sediment accumulation.

Multi-annual bi-monthly measurements of the Sand Motor's topography are used for a large scale aeolian sediment budget analysis. The analysis revealed that aeolian sediment supply from the dry beach area, that is almost permanently exposed to wind, diminished a half year after construction of the Sand Motor. The reduction in aeolian sediment supply is likely due to the development of a beach armor layer. In the subsequent years, two-third of the aeolian sediment deposits originate from the low-lying beaches that are frequently flooded and therefore often moist.

The importance of the low-lying beaches in the Sand Motor region is tested during a six-week field campaign. Gradients in aeolian sediment transport are measured during the field campaign as to localize aeolian sediment source and sink areas. A consistent supply from the intertidal beach area was measured that was temporarily deposited at the higher dry beach. The temporary deposits were transported further during high water, when sediment supply from the intertidal beach ceased, resulting in a continuous sediment supply to the dunes. The temporary deposition of sediment at the dry beach was likely promoted by the presence of a berm that affects the local wind shear. Moreover, the berm edge coincided with the onset of the beach armor layer that might have further promoted deposition of sediment.

The measurements on spatiotemporal variations in aeolian sediment availability and supply inspired an attempt to capture the characteristics of aeolian sediment availability in coastal environments in a comprehensive model approach. The resulting model simulates spatiotemporal variations in bed surface properties and their combined influence on aeolian sediment availability and transport. The implementation of multi-fraction aeolian sediment transport in the model introduces the recurrence

relation between aeolian sediment availability and transport through self-grading of sediment.

The model was applied in a four-year hindcast of the Sand Motor mega nourishment as first field validation. The model reproduces the multi-annual aeolian sediment erosion and deposition volumes, and the relative importance of the intertidal beach area as source of aeolian sediment well. Seasonal variations in aeolian sediment transport are incidentally missed by the model. The model accuracy is reflected in a R^2 value of 0.93 when comparing time series of measured and modeled total aeolian sediment transport volumes in the four years since construction of the Sand Motor. The results suggest that indeed significant limitations in sediment availability, due to soil moisture content and beach armoring, govern aeolian sediment transport in the Sand Motor region. A comparison with a simulation without limitation in sediment availability suggests that aeolian sediment availability in the Sand Motor region is limited to about 25% of the wind transport capacity. Moreover, both spatial and temporal variations in aeolian sediment availability as well as the recurrence relation between aeolian sediment availability and transport are essential to accurate long term and large scale aeolian sediment transport estimates.

SAMENVATTING

Dit proefschrift onderzoekt de invloed van de beschikbaarheid van eolisch sediment op het transport van eolisch sediment. Het doel van dit onderzoek is het verbeteren van grootschalige langetermijnvoorspellingen van eolisch sedimenttransport in (gesuppleerde) kustgebieden. Bestaande eolisch sedimenttransportmodellen presteren in het algemeen matig ten opzichte van metingen in kustgebieden. De matige prestaties worden dikwijls geweten aan een beperkte sedimentbeschikbaarheid. Specifieke eigenschappen van het strandoppervlak, zoals de bodemvochtigheid of de aanwezigheid van niet-erodeerbare elementen als schelpen, beïnvloeden de sedimentbeschikbaarheid. Beperkte sedimentbeschikbaarheid kan er uiteindelijk toe leiden dat het sedimenttransport niet meer bepaald door de transportcapaciteit van de wind.

De eolisch sedimentbeschikbaarheid is een tamelijk ongrijpbaar fenomeen, omdat naast eolische ook marine en meteorologische processen de sedimentbeschikbaarheid beïnvloeden. Bovendien variëren deze processen op verschillende ruimtelijke en temporele schalen. De Zandmotor, een in 2011 aangelegde megasuppletie van 21 Mm^3 langs de Delflandse kust, is gebruikt om de temporele en ruimtelijke variaties in de beschikbaarheid en transport van eolisch sediment te kwantificeren. Instuifvolumes rond de Zandmotor zijn klein in vergelijking met de transportcapaciteit van de wind, ondanks het grote suppletievolume, de grote strijklengtes en de vrijwel permanente blootstelling aan wind. Daarom is de sedimentbeschikbaarheid waarschijnlijk van significante invloed op de instuifvolumes in dit gebied.

Een grootschalige eolisch sedimentbudgetanalyse is uitgevoerd op basis van meerjarige tweemaandelijkse topografische metingen van de Zandmotor. De analyse toont aan dat vanaf een halfjaar na de aanleg van de Zandmotor de eolisch sedimentaanvoer van het droge strand sterk is verminderd. De afname is waarschijnlijk het gevolg van het ontstaan van een schelpenlaag. In de daarop volgende jaren is tweederde van het instuifvolume afkomstig uit de laaggelegen stranden rond de Zandmotor die periodiek onderstromen en daarom grotendeels vochtig zijn.

Tijdens een zes weken durende veldcampagne is de sedimenttoevoer vanaf de laaggelegen stranden rond de Zandmotor geverifieerd. Gradiënten in eolisch sedimenttransport zijn gemeten om de bron van eolisch sediment te bepalen. De aanvoer vanuit het intergetijdengebied bleek tijdelijk te sedimenteren op het hogere en droge strand. Deze tijdelijke afzettingen werden tijdens hoogwater verder getransporteerd, wanneer de sedimentaanvoer vanaf het intergetijdenstrand stagneerde. Hierdoor ontstond een continue toevoer van sediment richting de duinen. De tijdelijke afzetting van sediment op het droge strand werd vermoedelijk bevorderd door de aanwezigheid van een berm die de lokale schuifspanning van de wind beïnvloedt. Bovendien viel de rand van de berm samen met het begin van de schelpenlaag die het neerslaan van sediment mogelijk verder bevorderd heeft.

De veldmetingen zijn de basis geweest voor de ontwikkeling van een modelaanpak die de invloed van sedimentbeschikbaarheid op eolisch sedimenttransport beschrijft. Het ontwikkelde model simuleert ruimtelijke en temporele variaties in de samenstelling van het strandoppervlak en hun gezamenlijke invloed op de beschikbaarheid en

het transport van eolisch sediment. Het model onderscheidt meerdere korrelgrootte-fracties waardoor een recurrente betrekking tussen de beschikbaarheid en het transport van eolisch sediment ontstaat als gevolg van zelfgradering van sediment.

Het model is toegepast op de Zandmotor en vergeleken met de meerjarige topografische metingen als eerste veldvalidatie. Het model reproduceert de meerjarige erosie en depositie volumes van eolisch sediment, en het relatieve belang van het intergetijdengebied als bron van eolisch sediment, goed. Seizoensafhankelijke variaties in eolisch sedimenttransport worden soms onderschat door het model. De nauwkeurigheid van het model is weerspiegeld in een R^2 waarde van 0,93 wanneer gemeten en gemodelleerde tijdseries voor het totaal door de wind getransporteerde sedimentvolume in de vier jaar na constructie van de Zandmotor worden vergeleken. De resultaten suggereren dat significante beperkingen in sedimentbeschikbaarheid, als gevolg van het bodemvochtgehalte en het vormen van een schelpenlaag, inderdaad bepalend zijn voor het eolisch sedimenttransport rond de Zandmotor. Een vergelijking met een simulatie zonder beperkingen in de sedimentbeschikbaarheid suggereert dat de beschikbaarheid van eolisch sediment rond de Zandmotor is beperkt tot ongeveer 25% van de transportcapaciteit van de wind. Bovendien zijn zowel de ruimtelijke en temporele variaties in de sedimentbeschikbaarheid, evenals de recurrente betrekking tussen de sedimentbeschikbaarheid en het sedimenttransport essentieel voor een nauwkeurige grootschalige langetermijnvoorspelling van eolisch sedimenttransport.

1

INTRODUCTION

1.1 MOTIVATION

Aeolian sediment transport is a prerequisite to growth and resilience of coastal dunes. Coastal dunes function as a natural protection against flooding from the sea. As human societies are particularly attracted to low-lying areas near the sea, the reliability and resilience of the protective coastal dune systems becomes vital for economic activities and human well-being. This societal demand for a safe and comfortable living space, that initiated the discipline of coastal engineering, developed our understanding of coastal safety tremendously in the past decades. The increased understanding of our coastal systems resulted in structural mitigation of coastal risks using rigid solutions or local nourishments (Hamm et al., 2002) and the engineering of entire coastlines worldwide (Donchyts et al., 2016).

With the increased confidence in our ability to mitigate coastal risks, additional demands and functions for coastal flood protections arose. Soft engineering solutions with limited environmental and ecological impact gained preference over rigid solutions. Recently, the exponent of soft engineering emerged as nature-based coastal flood protections (Waterman, 2010; de Vriend et al., 2015). Nature-based flood protections pursue the idea of stimulating natural processes with the aim of increasing coastal safety and is based on the assumption that the incidental or concentrated interventions necessary for the stimulation of nature are less intrusive than classic solutions to coastal safety. Moreover, nature-based solutions tend to include long-term monitoring and periodic adaptation and intervention that increases flexibility with respect to planning and execution as well as the occurrence of coastal hazards. The increased flexibility can make nature-based flood protection also cost-effective (Van Slobbe et al., 2013).

An innovative example of a nature-based solution to coastal safety is the Sand Motor (or Sand Engine, Stive et al., 2013). The Sand Motor is an artificial sandy peninsula that was constructed along the Dutch coast in 2011. The Sand Motor provides a 21 Mm^3 sediment source to the Dutch coast that is to be dispersed by natural processes, like tides and waves, over a period of about two decades. Although the construction of the Sand Motor clearly disturbs the coastal system, the disturbance is incidental and concentrated. In addition, the presence of the Sand Motor theoretically decreases the necessity of measures to mitigate coastal risks at other locations along the Dutch coast.

The Sand Motor is the provisional pinnacle of the evolution of soft engineering solutions to coastal safety in The Netherlands. Soft engineering solutions started

with the dynamic preservation act of 1990 that prescribes an extensive nourishment program initiated to protect The Netherlands from flooding from the sea (Min. V&W, 1990). Since the start of the program the distance between nourishments and dunes increased steadily. The initial dune and beach nourishments were replaced by foreshore nourishments as these are more cost-effective and less intrusive to the environmental and recreational functions of the coastal dune system. Nature-based solutions, like the Sand Motor, typically place nourishments kilometers away from the dune system that needs to be enforced.

With the increasing distance between nourishments and dunes, the effectiveness of nourishments in mitigating coastal risks becomes more difficult to assess. Ultimately the reliability of coastal dune systems is related to the sediment volume that is contained by the system. However, also the location in the coastal profile where the sediment resides is important. Sediment in the dunes provides a direct buffer against flooding in case of storm erosion, while sediment on the beach and foreshore influences coastal safety indirectly by depth-induced breaking of waves and consequently a reduction of the critical dune volume required to withstand a normative storm (Walstra, 2016). The sediment volume that resides in the dunes provides arguably a more persistent protection against flooding as the volume is typically only affected by severe storms. In contrast, the sediment volume that resides on the foreshore and beach is affected by seasonal nearshore bar cycles and mild storms, which increase the uncertainty of its contribution to coastal safety. It is therefore relevant to understand how sediment arrives in the dunes and provide a persistent contribution to coastal safety.

A key issue is to understand sediment transport pathways from nourishment to dunes. Many studies and sophisticated numerical models are available that describe hydrodynamic sediment transport. However, only a small fraction of the sediment moved in the nearshore ultimately arrives in the dunes (Aagaard et al., 2004). It is this small wind-induced sediment flux that provides us with the natural and persistent coastal flood protection that nature-based solutions aim for. In addition, this small wind-induced sediment flux gives coastal dune systems the natural resilience to storm impacts and the conditions for survival of persistent dune vegetation that strengthens the coastal dune systems, like marram grass (Borsje et al., 2011). It is also this small wind-induced sediment flux that is least understood and consistently overestimated by existing sediment transport models.

Aeolian sediment transport models describe the wind-induced sediment transport rate. In coastal environments these models tend to overestimate the aeolian sediment accumulation volumes, which is often accredited to limitations in sediment availability (Houser, 2009; Delgado-Fernandez et al., 2012; de Vries et al., 2014a). Sediment availability can be limited by particular properties of the bed surface. For example, if the beach is moist or covered with non-erodible elements, like shells (Wiggs et al., 2004; Edwards and Namikas, 2009; Namikas et al., 2010; McKenna Neuman et al., 2012). If sediment availability is limited, the aeolian sediment transport rate is governed by the sediment availability rather than the wind transport capacity, which violates the common assumption in aeolian sediment transport models.

This thesis explores the nature of aeolian sediment availability and its influence on aeolian sediment transport with the aim to improve large scale and long term aeolian sediment transport estimates in nourished coastal environments. This work is per-

formed within the framework of *ERC-Advanced Grant 291206 – Nearshore Monitoring and Modeling (NEMO)* that aims at an integrated modeling strategy for large scale and long term coastal sediment transport that extends from foreshore to backshore. Improving aeolian sediment transport estimates helps the completion of the sediment transport pathways from foreshore to backshore and from nourishment to dunes and thereby the assessment of measures that attempt to mitigate coastal risks, including nature-based coastal flood protections, on their effectiveness.

1.2 RESEARCH OBJECTIVES

This thesis pursues four main research objectives. Each chapter is dedicated to one research objective. The research objectives are elaborated in research questions that are addressed in the concluding chapter of this thesis (Chapter 7). The research objectives and questions are formulated as:

RESEARCH OBJECTIVE A Identify the main sources for aeolian sediment at the Sand Motor mega nourishment (Chapter 2).

The research questions related to this objective are:

- A1 What is the total aeolian sediment supply at the Sand Motor mega nourishment?
- A2 What are the main deposition areas of aeolian sediment at the Sand Motor mega nourishment?
- A3 What are the main source areas of aeolian sediment at the Sand Motor mega nourishment?

RESEARCH OBJECTIVE B Identify the main processes that govern aeolian sediment availability and supply at the Sand Motor mega nourishment (Chapter 3).

The research questions related to this objective are:

- B1 What processes govern the supply of aeolian sediment from the source areas?
- B2 What processes govern the deposition of aeolian sediment in the deposition areas?
- B3 What bed surface characteristics are related to aeolian sediment supply?

RESEARCH OBJECTIVE C Describe the generic influence of spatiotemporal variations in aeolian sediment availability on aeolian sediment transport in coastal environments (Chapter 4).

The research questions related to this objective are:

- C1 What are existing approaches to describe the influence of aeolian sediment availability on aeolian sediment transport, what are the similarities and differences among them and which approaches are mutually exclusive?

C2 What processes that were identified to be relevant to aeolian sediment availability are not covered with sufficient accuracy by existing approaches?

C3 What are the requirements for an approach that harmonizes existing, mutual inclusive approaches and is conceptually able to describe all processes relevant to aeolian sediment availability and transport?

RESEARCH OBJECTIVE D Validate the numerical model approach to reproduce the location and size of sources for aeolian sediment at the Sand Motor mega nourishment (Chapter 5).

The research questions related to this objective are:

D1 Can the calibrated numerical model reproduce the total aeolian sediment supply at the Sand Motor mega nourishment with any statistical significance?

D2 Can the calibrated numerical model reproduce the main source and deposition areas at the Sand Motor mega nourishment?

D3 What implemented processes are in retrospect significant to the model result?

1.3 THESIS OUTLINE

This thesis constitutes four parts:

Part I presents field data dedicated to the aeolian sediment supply and transport at the Sand Motor mega nourishment.

Chapter 2 presents a large scale aeolian sediment budget analysis that identifies the main suppliers of aeolian sediment in the Sand Motor region.

The large scale sediment budget analysis inspired the six-week field campaign presented in Chapter 3. Gradients in aeolian sediment transport were measured during the field campaign. Gradients in aeolian sediment transport reveal areas with net erosion and thereby the sources of aeolian sediment. The measurements therefore enable a detailed analysis of processes governing the spatiotemporal variations in aeolian sediment availability as identified in the aeolian sediment budget analysis.

Part II presents a numerical model for aeolian sediment availability and transport that is inspired by the field observations.

The field data show that significant spatial variations in aeolian sediment availability can exist and can affect net aeolian sediment transport rates. The variations in aeolian sediment availability coincide with changes in bed surface properties, like soil moisture content and beach armoring. In coastal environments these bed surface properties typically also vary in time. Assuming that the spatiotemporal variations in bed surface properties indeed

influence the aeolian sediment availability and transport, a numerical aeolian sediment transport model is developed.

Chapter 4 presents the model philosophy and design. The model focuses on the incorporation of spatiotemporal variability in aeolian sediment availability, which is illustrated using the process of beach armoring. Beach armoring occurs when roughness elements emerge from the bed and is a typical process that causes spatiotemporal variations in aeolian sediment availability. Both conceptual cases and wind tunnel experiments are used to illustrate the basic model behavior.

Chapter 5 describes the calibration and application of the model to the field data presented in Chapter 2 as a first field validation of the numerical model.

Part III concludes this thesis by addressing the research objectives and questions, and a discussion on the nature of aeolian sediment availability and corresponding modeling strategies.

Part IV contains appendices with specifics on the reference model, the numerical model implementation and available model settings presented in Chapter 4.

Part I

FIELD DATA

Field data is collected at the Sand Motor mega nourishment in The Netherlands. The Sand Motor showed a peculiar morphological development since its construction as it is permanently exposed to wind and yet its sub-aerial morphology is remarkably static.

2

LARGE SCALE SEDIMENT BUDGETS

This chapter is based on another publication: Hoonhout, B. M. and de Vries, S. (2017a). Aeolian sediment supply at a mega nourishment. Coastal Engineering. *Submitted.*

2.1 INTRODUCTION

Aeolian sediment supply is a prerequisite to growth and resilience of coastal dunes that function as a natural protection against flooding from the sea. Expanding human activities in coastal areas and growing uncertainties related to climate change, increase coastal risks. Mitigation of these risks resulted in the engineering of entire coastlines (Donchyts et al., 2016). Rigid solutions and local nourishments are traditional solutions to a societal demand for coastal safety (Hamm et al., 2002). With the increased confidence in our ability to mitigate coastal risks, additional demands and functions for coastal flood protections arose. Soft engineering solutions with limited environmental and ecological impact (Waterman, 2010; de Vriend et al., 2015) gained preference over rigid solutions or local nourishments. Recently, the exponent of soft engineering emerged as mega nourishments (Stive et al., 2013). Mega nourishments pursue the idea of stimulating natural sediment transport processes with the aim of increasing coastal safety. The idea is based on the assumption that the incidental or concentrated interventions necessary for the stimulation of nature are less intrusive than classic solutions to coastal safety. Moreover, mega nourishments tend to accommodate long-term monitoring and periodic adaptation and intervention that increases flexibility with respect to planning and execution as well as the occurrence of coastal hazards. The increased flexibility can make mega nourishments also cost-effective (Van Slobbe et al., 2013).

The effectiveness of a mega nourishment depends on the sediment transport pathways from nourishment to dunes. A small fraction of the sediment moved in the nearshore ultimately arrives in the dunes (Aagaard et al., 2004). It is this small aeolian sediment supply that provides us with the natural and persistent coastal safety that mega nourishments aim for. In addition, this small aeolian sediment supply gives coastal dune systems the natural resilience to storm impacts and the conditions for survival of persistent dune vegetation that strengthens the dunes, like marram grass (Borsje et al., 2011). It is also this small aeolian sediment supply that is least understood.

Mega nourishments affect aeolian sediment supply to coastal dunes in various ways. First, sand used for nourishment is typically obtained from offshore borrowing pits and differs from the original beach sand in terms of size and composition, affect-

ing the erodibility of the beach (van der Wal, 1998, 2000). Second, aeolian sediment availability (following the definition of Kocurek and Lancaster, 1999) at beach nourishments that are constructed above storm surge level can be significantly reduced by deflation lag deposits (Jackson et al., 2010). The absence of regular flooding and wave-reworking allows lag deposits to develop a beach armor layer, resulting in compartmentalization of the nourishment in armored and unarmored surfaces. McKenna Neuman et al. (2012) illustrated how deflation lag deposits increase the shear velocity threshold significantly and reduce aeolian sediment availability and subsequently supply from the higher supratidal beach. Deflation lag deposits can therefore cause intertidal and low-lying supratidal beaches to gain importance over the high and dry beach as source of aeolian sediment. Third, the placement of a nourishment is known to affect nearshore processes (Grunnet and Ruessink, 2005; Ojeda et al., 2008; De Schipper et al., 2013). Synchronization between aeolian and nearshore processes, like onshore bar migration and welding, is reported to stimulate aeolian sediment supply to coastal dunes (Houser, 2009; Anthony, 2013). The importance of low-lying beaches as source of aeolian sediment might therefore also be affected by changing bar dynamics.

Jackson and Nordstrom (2011) emphasized the necessity for the quantification of the effect of large scale beach nourishment designs on aeolian sediment supply. Quantitative predictions of aeolian sediment availability and supply in coastal environments has proven to be challenging (Sherman et al., 1998; Sherman and Li, 2012). Limitations in aeolian sediment availability are often identified as reason for the discrepancy between measured and predicted sediment transport rates (Delgado-Fernandez et al., 2012; de Vries et al., 2014a; Lynch et al., 2016).

Mega nourishments inherently cause spatiotemporal variations in aeolian sediment availability. The spatial variations are caused by compartmentalization of the beach. The temporal variations are induced by adaptation of the large coastal disturbance to the wave and wind climate, resulting in changing in beach width, slope and composition (de Schipper et al., 2016). Consequently, quantification of aeolian sediment availability and supply from mega nourishments requires differentiation in space and time.

This paper presents an aeolian sediment budget analysis of the 21 Mm^3 Sand Motor mega nourishment based on four years of bi-monthly topographic surveys. The sediment budget analysis quantifies the net aeolian sediment supply to the dunes, dune lake and lagoon accommodated by the Sand Motor. The Sand Motor constitutes distinct areas that are either influenced by marine processes, by aeolian processes or by a combination of both. Therefore, the influence of marine and aeolian processes on aeolian sediment supply can be separated and spatiotemporal variations in aeolian sediment availability can be identified with reasonable accuracy. The observed compartmentalization of the Sand Motor is discussed in relation to limitations in aeolian sediment availability, as well as the design of mega nourishments like the Sand Motor as solution to coastal safety.

2.2 FIELD SITE

The Sand Motor (or Sand Engine) is an artificial 21 Mm^3 sandy peninsula protruding into the North Sea off the Delfland coast in The Netherlands (Figure 2.1, Stive et al.,

2013). The Sand Motor is an example of a mega nourishment and is intended to nourish the Holland coast for a period of two decades, while stimulating both biodiversity and recreation.

The Sand Motor was constructed in 2011 and its bulged shoreline initially extended about 1 km seaward and stretched over approximately 2 km along the original coastline. The original coast was characterized by an alongshore uniform profile with a vegetated dune with an average height of 13 m and a linear beach with a 1:40 slope. The dune foot is located at a height of approximately 5 m+MSL.

Due to natural sediment dynamics the Sand Motor distributes about 1 Mm^3 of sand per year to the adjacent coasts (Figure 2.1). The majority of this sand volume is transported by tides and waves. However, the Sand Motor is constructed up to 5 m+MSL and locally up to 7 m+MSL, which is in either case well above the maximum surge level of 3 m+MSL (Figure 2.2c). Therefore, the majority of the Sand Motor area is uniquely shaped by wind.

The Sand Motor comprises both a dune lake and a lagoon that act as large traps for aeolian sediment (Figure 2.1). The lagoon is affected by tidal forcing, although the tidal amplitude quickly diminished over time as the entry channel elongated. The tidal range of about 2 m that is present at the Sand Motor periphery (Figure 2.2c), is nowadays damped to less than 20 cm inside the lagoon (de Vries et al., 2015). Consequently, the tidal currents at the closed end of the lagoon, where most aeolian sediment is trapped, are negligible.

Sand used for construction of the Sand Motor is obtained from an offshore borrowing pit in the North Sea. The sand is predominantly Holocene sand with a significant amount of fines. The median grain size is slightly coarser than found originally along the Delfland coast. Apart from sand fractions, the sediment contains a large amount of shells, shell fractions, some pebbles and cobbles and an occasional fraction of a mammoth bone.

The dominant wind direction at the Sand Motor is south to southwest (Figure 2.2a). However, during storm conditions the wind direction tends to be southwest to northwest. During extreme storm conditions the wind direction tends to be northwest. Northwesterly storms are typically accompanied by significant surges as the fetch is virtually unbounded to the northwest, while surges from the southwest are limited due to the presence of the narrowing of the North Sea at the Strait of Dover (Figure 2.1, inset).

2.3 METHODOLOGY

Spatiotemporal variations in aeolian sediment supply in the Sand Motor domain are identified using an aeolian sediment budget analysis. A sediment budget analysis can be performed if frequent topographic measurements are available (Davidson-Arnott and Law, 1990) and sediment exchange over the border of the measurement domain is limited. In a sediment budget analysis the morphological change in predetermined areas are converted to volumetric changes (budgets) that are compared in a sediment volume balance.

A sediment budget analysis is particularly suitable for coastal sites with a complex and dynamic topography, like the Sand Motor. The use of (dense) topographic measurements ensures that any local variations in the topography are included. Moreover,

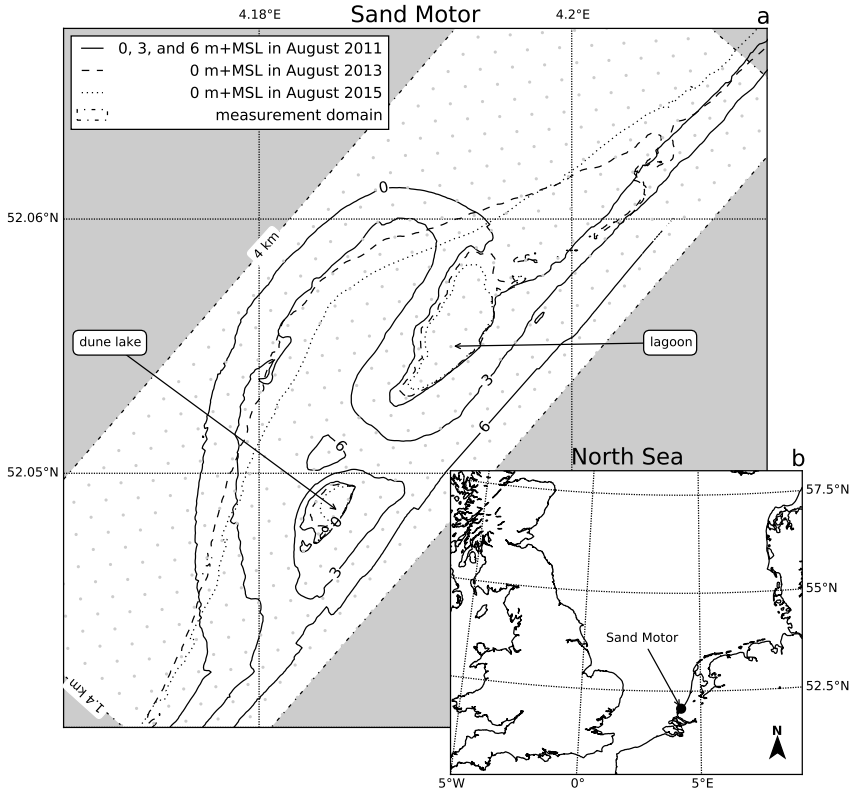

Figure 2.1: Location, orientation, appearance and evolution of the Sand Motor between construction in 2011 and 2015. The box indicates the measurement domain used in the remainder of this paper. A 100 x 100 m grid aligned with the measurement domain is plotted in gray as reference.

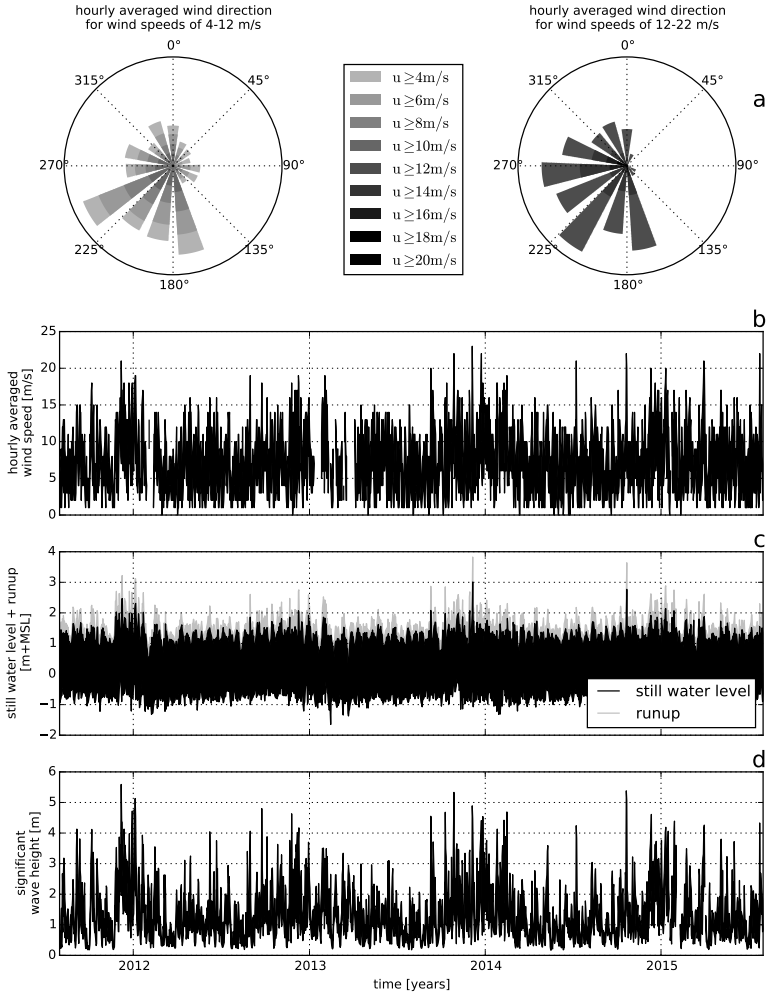

Figure 2.2: Wind and hydrodynamic time series from 2011 to 2015. Hourly averaged wind speeds and directions are obtained from the KNMI meteorological station in Hoek van Holland (upper panels). Offshore still water levels, wave heights and wave periods are obtained from the Europlatform (lower panels). Runup levels are estimated following Stockdon et al. (2006).

no assumptions on the local representativeness of the measurements are needed. The methodology is applicable to a wide range of spatial or temporal scales, allowing a multi-annual analysis of aeolian sediment supply in the Sand Motor domain.

In the Sand Motor domain it is possible to separate the marine and aeolian influence on erosion and deposition of sediment directly from a sediment budget analysis. The high construction height of the Sand Motor and the absence of regular storm surges in the first four years after construction make that distinct areas exist that are either influenced by marine or aeolian processes. The sediment budgets are determined along the borders of these marine and aeolian zones.

2.3.1 *Topographic measurements*

32 topographic measurements of the Sand Motor domain obtained over a period of four years are used to determine the overall sediment budget of the Sand Motor domain (de Schipper et al., 2016). The measurement area covers 1.4 km cross-shore and 4 km alongshore (Figure 2.1). The nearshore bathymetry is surveyed using a jetski equipped with an echo sounder and RTK-GPS receiver. The topography of the Sand Motor from the waterline up to the dune foot is surveyed using an all-terrain vehicle (ATV) that is also equipped with a RTK-GPS receiver. Inundated areas that are too shallow for the jetski, like the tidal channel and the dune lake, are surveyed using a manually pushed RTK-GPS wheel. The survey is performed along cross-shore transects that are 20 m apart. The resulting trajectories are interpolated to a regular 10 m x 10 m grid for the sediment budget analysis. Surveys that show a morphological rate of change that is more than two standard deviations from the average are considered outliers. The measurements of September 4, 2011 and June 21, 2012 are discarded as outliers.

The topography in the dune area, which is not included in the RTK-GPS surveys, is monitored by airborne lidar. Half-yearly measurements from the southern Holland coast (Delfland coast) are available since 2011, prior to the construction of the Sand Motor. The lidar measurements have a spatial resolution of 2 m or 5 m. The measurements are corrected for the presence of vegetation and artificial objects, like beach pavilions, and interpolated to the same 10 m x 10 m grid and the same moments in time as the RTK-GPS measurements.

2.3.2 *Zonation*

The Sand Motor domain is divided into seven zones for the aeolian sediment budget analysis (Table 2.1 and Figure 2.3). The zonation aims to separate areas with marine influences from areas without marine influences, and separate areas with net aeolian erosion from areas with net aeolian deposition.

The zonation is based on the 0 m+MSL, 3 m+MSL and 5 m+MSL contour lines that roughly correspond to mean sea level, the edge of the berm or maximum runup level (Figure 2.2c) and the dune foot respectively. The contours are determined such that the spatial variance in the bed level change of the zones is minimized. The minimization ensures that the optimal division between erosion and deposition areas is found. Moreover, the 3 m+MSL and 5 m+MSL contour lines have been relatively static since construction of the Sand Motor.

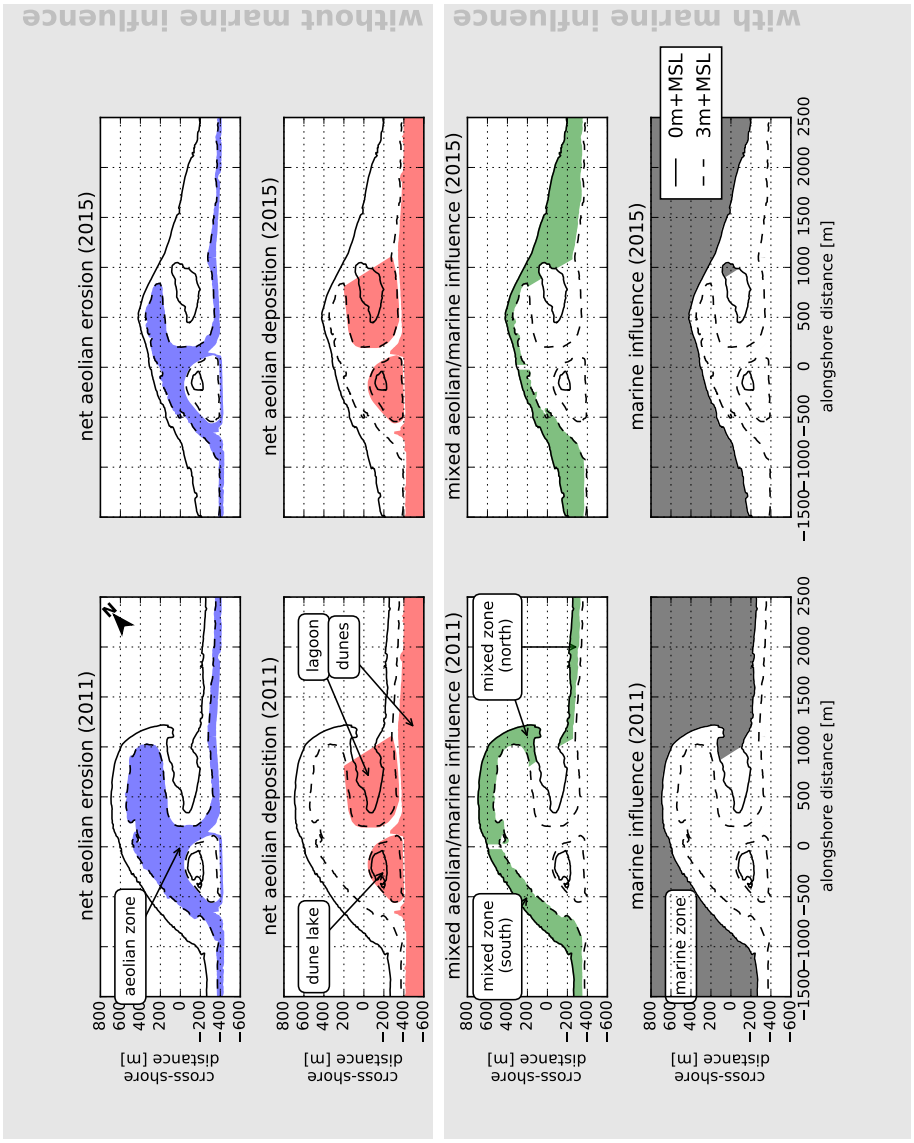

Figure 2.3: Zonation of the Sand Motor domain into zones with net aeolian erosion and no marine influence, net aeolian deposition and no marine influence, mixed aeolian/marine influence and marine influence. Left panels: 2011. Right panels: 2015.

Table 2.1: Zonation of the Sand Motor domain into seven zones with and without marine influence. See also Figure 2.3.

without marine influence	*with* marine influence
aeolian zone	mixed zone (north)
dunes	mixed zone (south)
dune lake	marine zone
lagoon	

To ensure a constant shape and size of the zones during the analysis, the convex hull of all 3 m+MSL contour lines is used as zone boundary for the lake and lagoon. Also for the dunes minimal variations over time in zone shape and size are removed by using the most seaward position of all contour lines. Consequently, only the aeolian zone and mixed zones change in shape and size over time. The volumetric change between two consecutive measurements is determined for these zones within the smaller contour:

$$\Delta V^n = \hat{A}_c \cdot \left(\overline{z_b}^n - \overline{z_b}^{n-1} \right) \quad \text{where } \hat{A}_c = \min \left(A_c^n \; ; \; A_c^{n-1} \right) \tag{2.1}$$

with ΔV^n the volume change, A_c^n the surface area of the zone and $\overline{z_b}^n$ the average bed level in the zone, all in time interval n. The (cumulative) sum over all time intervals of the volume changes in each zone is used in the analysis. By using the smaller of two contours in a comparison, a part of the larger contour is neglected:

$$A_{c,\text{neglected}}^n = \max \left(A_c^n \; ; \; A_c^{n-1} \right) - \hat{A}_c \tag{2.2}$$

The neglected area of the zone with the largest change in size, the aeolian zone, is on average 2% and never larger than 8%.

2.3.3 *Spatial variations in porosity*

The change in sediment volume is susceptible to changes in porosity. In order to relate the changes in sediment volume to the transport of sediment mass, variations in porosity need to be accounted for. Porosity values in the Sand Motor domain are obtained from core samples and used to account for the spatial variations in porosity. The core samples have a diameter of 8 cm and depth of 10 cm from the bed surface in an attempt to capture the porosity in the aeolian active layer of the bed. Each sample is dried and submerged in water to determine the porosity. For comparison, all presented sediment volumes in this paper are converted to a hypothetical porosity of 40% according to:

$$V_{40\%} = V \cdot \frac{1 - p}{1 - 40\%} \tag{2.3}$$

where V [m^3] is the measured sediment volume and p [-] the porosity.

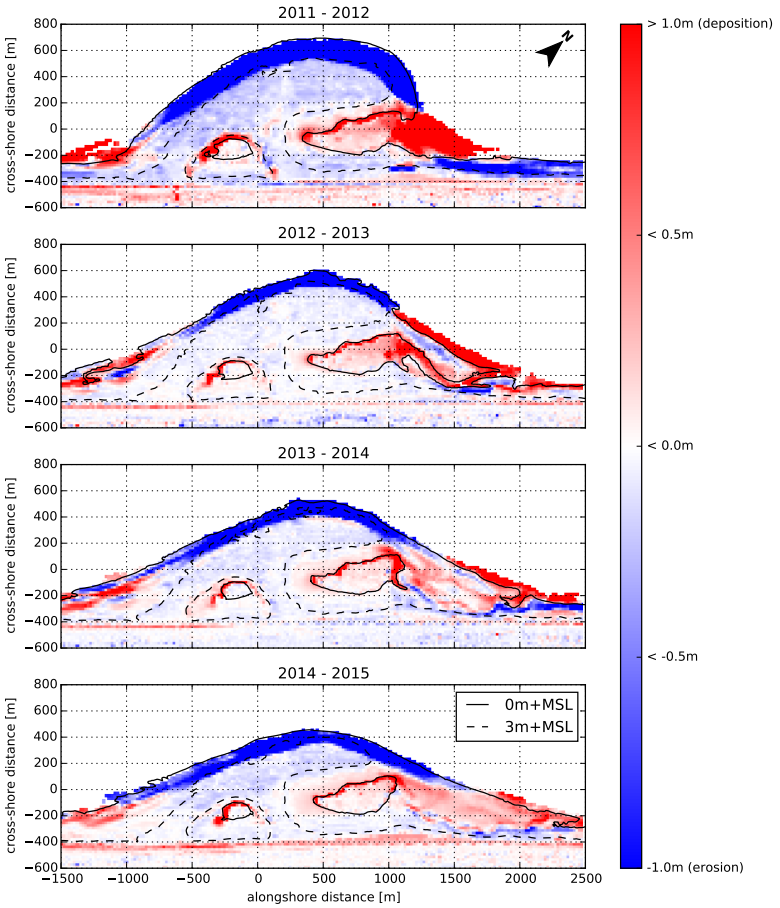

Figure 2.4: Yearly sedimentation and erosion above 0 m+MSL in the Sand Motor domain. Comparisons are made between the September surveys of each year.

Table 2.2: Measured porosity values in the Sand Motor domain. Each area is sampled at three different locations. The results per area are presented in ascending order. The last column presents the average porosity for each area that is used to convert the sediment volumes presented in this paper to a hypothetical porosity of 40%.

Area	Porosity			
	min.		max.	avg.
Aeolian zone	39.0%	39.4%	40.2%	39.5%
Mixed zone (north)	38.4%	39.8%	40.8%	39.7%
Mixed zone (south)	37.1%	38.4%	38.4%	38.0%
Dunes	36.1%	36.3%	37.1%	36.5%
Dune lake	34.7%	34.9%	36.3%	35.3%
Lagoon	46.3%	47.3%	49.0%	47.6%

2.4 RESULTS

The overall sediment budget of the Sand Motor domain is determined given morphological change in the net aeolian erosion and net aeolian deposition zones for the period between September 1, 2011 and September 1, 2015 (Figure 2.4).

2.4.1 *Morphological change and porosity*

The net morphological change within the 3 m+MSL contour can be accredited entirely to aeolian sediment transport as this area is not significantly affected by marine processes since the construction of the Sand Motor. Also the net contribution of alongshore sediment fluxes are assumed to be relatively small given that the beach width ($<$ 100 m) is small compared to the alongshore span of the measurement domain (4 km). Within the 3 m+MSL contour sediment is deposited in the dunes and eroded from the aeolian zone.

The morphological change in the dune lake and the closed end of the lagoon is assumed to be driven predominantly by wind. Hydrodynamic forcing and consequently marine deposits in these zones diminished quickly over time, while significant amounts of fine aeolian deposits are found along the southwestern to northwestern shores.

The aeolian contribution to the morphological change in the mixed zones cannot be determined directly due to the presence of both marine and aeolian forces. However, by balancing the changes in sediment volume in the net aeolian deposition zones with the changes in sediment volume in the net aeolian erosion zones the aeolian sediment supply from the mixed zones is estimated.

18 porosity measurements from six zones (Table 2.2) are used to convert all measured sediment volumes to a hypothetical porosity of 40%.

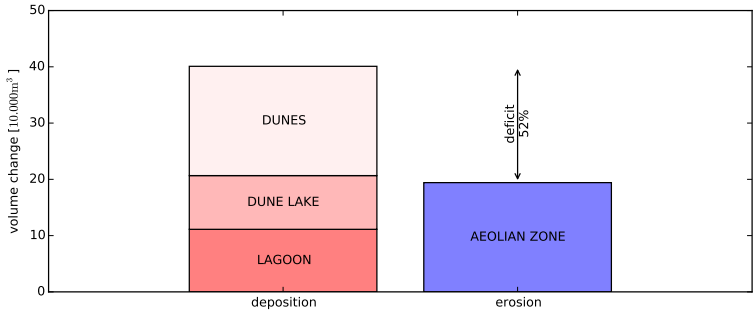

Figure 2.5: Aeolian sediment budgets in the Sand Motor domain in the period between September 1, 2011 and September 1, 2015.

2.4.2 *Aeolian sediment budgets*

The aeolian zone consistently provides less sediment than is deposited in the dunes, dune lake and lagoon (Figure 2.5). Over the four years since construction of the Sand Motor the volume deficit accumulates to $21 \cdot 10^4$ m^3, which is 52% of the total sediment accumulation of $40 \cdot 10^4$ m^3. The total wind transport capacity (or cumulative theoretical sediment transport volume) in this period is roughly estimated as $110 \cdot 10^4$ m^3 (Appendix A). As the actual sediment transport rates appear to be only about 35% of the wind transport capacity, the Sand Motor can be classified as an availability-limited system.

Late January 2012, the surveys show a net volume deficit of zero, while subsequent surveys show a more or less linear growth of the volume deficit (Figure 2.6). Fitting a linear trend reveals an average growth rate of $5.2 \cdot 10^4$ m^3/yr, which is 67% of the total sediment accumulation rate of $7.7 \cdot 10^4$ m^3/yr ($R^2 = 0.96$). The increase in growth rate of the volume deficit is likely caused by a significant decrease of the sediment contribution from the aeolian zone. The erosion from the aeolian zone in the first half year after construction of the Sand Motor exceeds the total erosion in the four years thereafter, while sediment continued to be accumulated in the dunes, dune lake and lagoon. The surface area of the aeolian zone decreased continuously (Figure 2.7).

The diminishing of the aeolian sediment supply from the aeolian zone is also reflected in the average bed level within the 3 m+MSL contour of September 22, 2015 (Figure 2.8). The bed level within this contour has been almost constant since the volume deficit started to grow steadily from late January 2012. Only a few periods of significant erosion can be distinguished that can be related to storm events. Most notably, the event of December 5, 2013 with wind speeds up to 34 m/s. That day $1.5 \cdot 10^4$ m^3 of sediment was eroded from within the 3 m+MSL contour of September 22, 2015, which is 52% of the total erosion that year. Although this event is among the few events during which the runup levels exceeded the 3 m+MSL level (Figure 2.2), the erosion can still be accredited to wind as the 3 m+MSL contour of September 22, 2015 was located about 100 m landward of the 3 m+MSL contour at the time of the

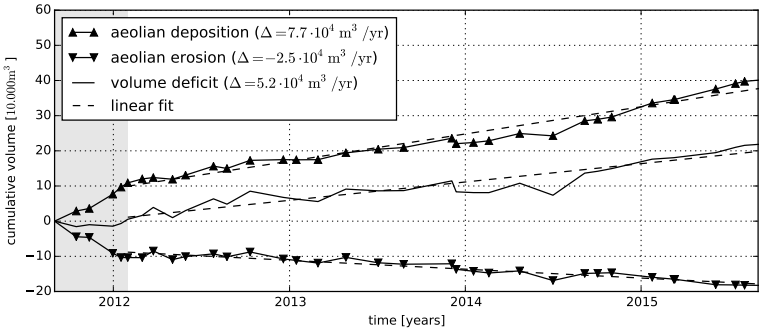

Figure 2.6: Cumulative change in sediment volume of all net aeolian erosion and net aeolian deposition zones and the volume deficit. For the linear fit the period prior to February 2012 is discarded (shaded).

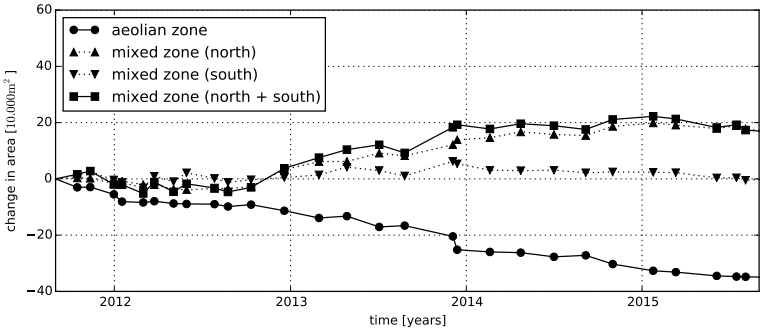

Figure 2.7: Change in size of aeolian zone and mixed zones since construction of the Sand Motor in 2011.

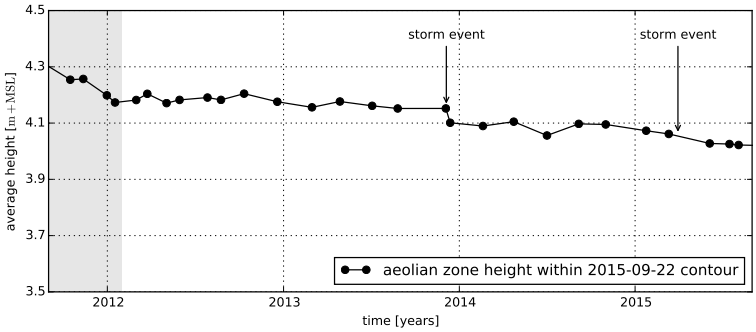

Figure 2.8: Average height of the aeolian zone in the most recent contour.

storm event. Therefore the bed level in the more recent contour was not affected by the surge, which is confirmed by observations from a local permanent camera station.

In general, the use of the 3 m+MSL contour as divide between the areas with and without marine influence appears to be valid for almost the entire four years after construction of the Sand Motor. Only four events have been registered in which runup levels exceeded the 3 m+MSL level (Figure 2.2). Observations from a local permanent camera station indicate that only during the event of December 5, 2013 the surface of the aeolian zone was significantly affected by tides and waves. Pre- and post-storm topographic surveys that are available for this event indicate that the marine erosion from the flooded areas above the 3 m+MSL level was less than $1 \cdot 10^4$ m^3.

2.4.3 *Alongshore variation*

The sediment deposits in the dunes show an alongshore variation. A depression in dune growth is observed in the lee of the dune lake and lagoon (Figure 2.9). South of the dune lake and in between the dune lake and lagoon a passage for aeolian sediment transport is present, which seems to result in a locally elevated dune growth. The average dune growth of 14 $m^3/m/yr$ in the Sand Motor domain is low compared to the dune growth rate along the adjacent southern (15 $m^3/m/yr$) and northern (19 $m^3/m/yr$) beach stretches. However, aeolian deposits in the dune lake and lagoon are of the same order of magnitude resulting in a total average sediment deposition of 27 $m^3/m/yr$ in the Sand Motor domain, which is on average 56% higher than along the adjacent coasts.

2.5 DISCUSSION

The volume deficit between the net aeolian erosion and net aeolian deposition zones can be accredited to the mixed zones that are affected by both marine and aeolian processes. The mixed zones in the Sand Motor domain are consequently estimated to provide 67% of the aeolian sediment in the Sand Motor domain. The aeolian sediment supply from the mixed zones is therefore significant, but still small compared to the

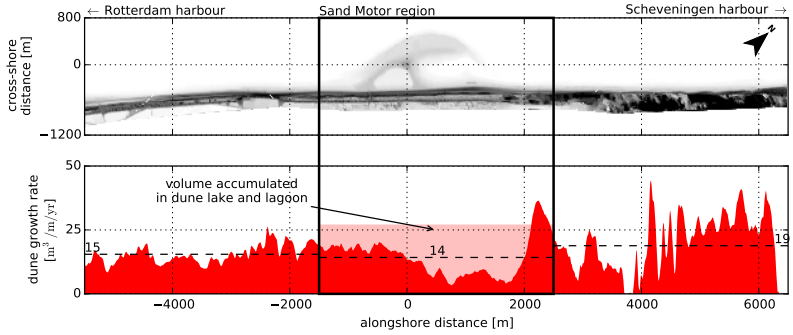

Figure 2.9: Comparison sediment accumulation rates in dunes (>3 m+MSL) for Sand Motor domain and adjacent coasts. Airborne lidar measurements from January 2012 until January 2015 are used. Horizontal dashed lines indicate local averages. The box indicates the Sand Motor domain depicted in previous figures.

98% reported by Jackson et al. (2010). The importance of the mixed zone cannot be explained by the size of the surface area as the mixed zones are initially smaller than the other main sediment source: the aeolian zone (Figure 2.7). Only from 2013 onward the surface area of the mixed zones exceed the area of the aeolian zone. However, the increase in surface area of the mixed zones is concentrated in the north where a low-lying spit develops (Figure 2.4). Given the dominant south to southwesterly wind direction and their position with respect to the lagoon that separates the spit from the dunes, it is unlikely that these intertidal beaches, provide a significant amount of sediment to dunes, dune lake and lagoon. Therefore, despite the periodic flooding and a size that is 40% – 60% smaller than the aeolian zone, the mixed zone (south) appears to provide the majority of the aeolian sediment in the Sand Motor domain.

2.5.1 *Sources of inaccuracies*

By accrediting the volume deficit to the mixed zones it is assumed that no sediment is exchanged over the boundaries of the Sand Motor domain and the sediment volume balance is thus closed. This assumption is not strictly valid, but the external sediment exchange with the Sand Motor domain is limited compared to the total sediment accumulation of $40 \cdot 10^4$ m^3.

The predominantly southwesterly wind direction might blow sediment over the lateral borders that is not taken into account. However, the net alongshore sediment supply to the Sand Motor domain is estimated to be two orders smaller than the net onshore sediment supply, or less than 1% of the total sediment accumulation (Figure 2.10), because:

1. The onshore and alongshore sediment flux *per meter width* are estimated to be of the same order of magnitude (Appendix A), but the lateral beach cross-section ($<$ 100 m) through which the alongshore flux enters the Sand Motor domain

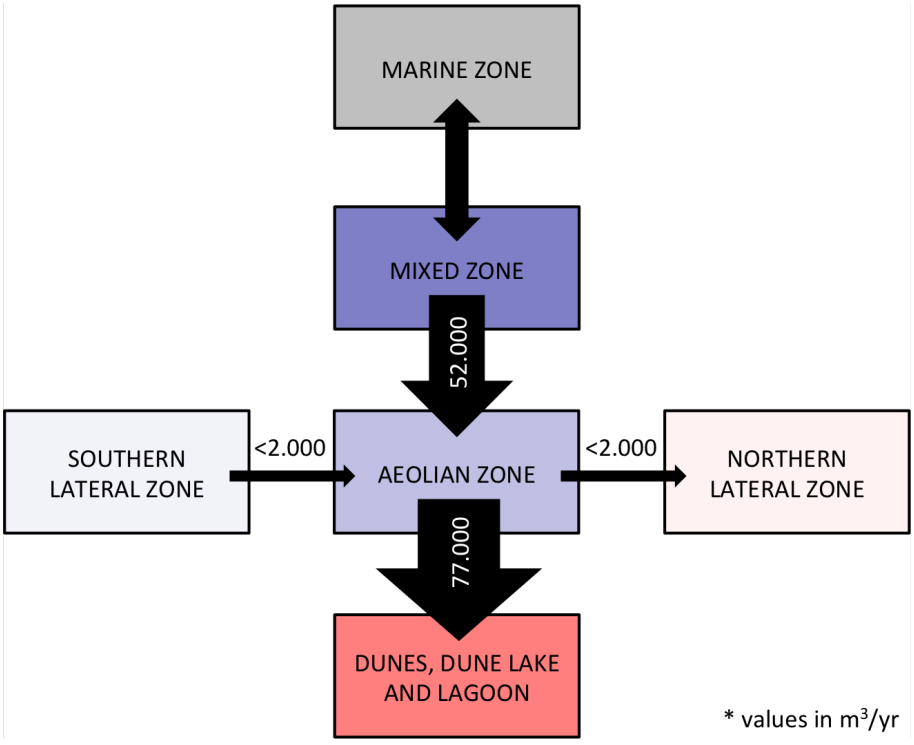

Figure 2.10: Aeolian sediment budget analysis of the Sand Motor

at the southern border is an order of magnitude smaller than the alongshore span of the Sand Motor domain (4 km) through which the onshore flux enters the domain. Therefore, the absolute alongshore contribution to the total sediment volume balance is likely an order of magnitude smaller than the onshore contribution.

2. The contribution of the net alongshore sediment flux that enters the Sand Motor domain at the southern border is at least partially compensated by a net alongshore sediment flux of the same order of magnitude that leaves the domain at the northern border. Therefore, the contribution to the total sediment volume balance of the southern and northern alongshore sediment fluxes combined (alongshore sediment transport gradient) is likely two orders of magnitude smaller than the contribution of the onshore sediment flux.

In reality the contribution of the alongshore sediment fluxes is likely to be even smaller as the sediment fluxes can locally be more onshore directed due to local wind steering. In addition, the estimates of the order of magnitude of the sediment fluxes are likely to be overestimated as possible limitations in sediment availability are ignored.

The influence of marine deposits in the lagoon is estimated to be less than 4% of the total sediment accumulation. 85% of the deposited sediment in the lagoon has the form of a southwesterly infill protruding above water and consisting of loosely packed, fine sediment and is therefore likely from aeolian origin (Figure 2.4 and Table 2.2). 15% of the deposited sediment in the lagoon, or 4% of the total sediment accumulation, is spread over a wider area and is possibly from marine origin.

The influence of marine erosion of the aeolian zone during the limited number of storm surges is estimated to be less than $1 \cdot 10^4$ m^3 (Section 2.4.2), or 2.5% of the total sediment accumulation. Similarly, the influence of the changing size of the aeolian zone is estimated to be 2% of the total erosion in this area (Section 2.3.2), or less than 1% of the total sediment accumulation.

In summary, the error that is introduced by assuming a closed sediment volume balance is estimated to be less than 9% of the total sediment accumulation. The volume deficit of 67% of the total sediment accumulation that is accredited to aeolian erosion from the mixed zones therefore needs to be nuanced and is estimated to be more than 58%.

2.5.2 *Beach armoring*

The relative importance of the mixed zones for aeolian sediment supply can likely be explained by a visually observed beach armor layer that developed in the aeolian zone since construction of the Sand Motor. A beach armor layer can reduce the availability of aeolian sediment significantly (McKenna Neuman et al., 2012). Because the Sand Motor was constructed several meters above common storm surge level, the aeolian zone has never been influenced by waves or tides. Consequently, no process is present that regularly resets the armor layer, except for the occasional high-energy wind event. Moreover, salt crusts that form due to salt spray have a similar effect on the sediment availability as an armor layer. Small concentrations of salt ($\leqslant 7$ mg/g) can already reduce the sediment availability by a factor two (Nickling and Ecclestone, 1981).

In contrast, no beach armor layer or salt crusts develop in the mixed zones as periodic flooding and related wave-reworking regularly deposit marine sediments, mix the top layer of the bed, and wash shells and shell fragments away. In addition, onshore bar migration and welding periodically provide additional unarmored sediment that can be entrained by the wind during low water (Houser, 2009; Anthony, 2013). However, aeolian sediment availability in the mixed zones is also limited due to the relatively high soil moisture contents in these areas. Also soil moisture content is known to increase the shear velocity threshold (Wiggs et al., 2004; Edwards and Namikas, 2009; Namikas et al., 2010) and limit the local aeolian sediment availability. Given that the mixed zones appear to be a more important supplier of aeolian sediment than the aeolian zone, limitations in sediment availability due to beach armoring seems to outweigh limitations due to high moisture contents.

During a storm event even shell fragments and shells can be mobilized. Consequently, the beach armor layer itself might be transported and its reducing effect on the sediment availability is (partially) neutralized. Storm events are regularly accompanied with surges that prevent wind erosion of the mixed zones. Entrainment of sediment therefore starts at a relatively high point along the fetch and much of the sediment transport capacity can be used for erosion of the aeolian zone, which contributes to the removal of the beach armor layer. If the surge is high enough it can also remove the beach armor layer by wave action or bury it by deposition of marine sediments. The removal or burial of the beach armor layer can elevate sediment availability from the aeolian zone also after the the storm passed. Only after development of a new beach armor layer the sediment availability and transport rates approach the pre-storm situation.

2.5.3 *Mega nourishments as coastal protection*

The Sand Motor mega nourishment shows a morphological development that is significantly different from natural beaches or the original Delfland coast. Aeolian sediment supply at the Sand Motor shows larger spatial variations compared to natural beaches, while dune growth rates lag behind compared to the adjacent coastal stretches. It can be questioned if such exotic behavior is desired for a coastal protection that aims to stimulate natural processes, or that, for example, it would be beneficial not to construct future mega nourishments above local storm surge level and prevent compartmentalization of the beach.

In this context, it is interesting to consider what would happen if the Sand Motor was constructed up to local storm surge level (3 m+MSL). The vast aeolian zone would not exist as the entire Sand Motor would be flooded at least once a year. Compartmentalization would be minimized and aeolian sediment availability be maximized as the formation of deflation lag deposits is counteracted by wave-reworking. The dune lake and lagoon would be filled in up to three times faster due to transport-limited aeolian sediment supply. Soon, all aeolian sediment transport pathways would end in the dunes, resulting in an up to six times larger dune growth than currently observed. Marine sediment transport would enhance these relatively rapid changes as more sediment is redistributed within the Sand Motor domain to the lagoon, dune lake and offshore by overwash.

A lower construction height of the Sand Motor would therefore result in a more rapid and more localized redistribution of sediment. Both rapid and localized redistribution are at odds with the purpose of the Sand Motor to nourish the entire Holland coast over a period of two decades. The static behavior of the supratidal areas of Sand Motor might therefore prove to be a crucial design criterion of a mega nourishment.

2.6 CONCLUSIONS

A sediment budget analysis is used to identify spatial variations in aeolian sediment deposition and supply, and dune growth in the Sand Motor domain. From the analysis the following conclusions can be drawn regarding aeolian sediment transport and supply in the Sand Motor domain:

1. The (southern) low-lying beaches that are affected by both aeolian and marine processes (mixed zone) currently supply more than 58% of all aeolian sediment deposits in the Sand Motor domain, despite that this area is periodically flooded and 40% – 60% smaller than the upper dry beach areas (aeolian zone) that are only affected by aeolian processes and supply less than 42% of the aeolian deposits;

2. The aeolian sediment supply from the aeolian zone diminished in the first half year after construction of the Sand Motor, likely due to the development of a beach armor layer;

3. The aeolian sediment supply from the aeolian zone tends to increase temporarily during and after a storm event, likely due to (partial) removal of the beach armor layer;

4. The dune growth in the Sand Motor domain is low compared to the adjacent coasts, likely due to blocking of aeolian sediment transport pathways by the dune lake and lagoon.

From the analysis the following conclusions can be drawn regarding mega nourishments in general:

1. The construction height should be a design criterion of any mega nourishment as it governs compartmentalization of the beach due to beach armoring;

2. Compartmentalization of the beach can influence the lifetime and region of influence of a mega nourishment as it affects the balance between local aeolian deposition and regional marine spreading of sediment.

3. The consequences of compartmentalization is not yet fully understood as the contribution of the upper dry beach (aeolian zone) to local aeolian sediment supply can range from 42% as observed at the Sand Motor to less than 2% as reported by Jackson et al. (2010).

3

SMALL SCALE SEDIMENT TRANSPORT

This chapter is based on another publication: Hoonhout, B. M. and de Vries, S. (2017b). Field measurements on spatial variations in aeolian sediment availability at the Sand Motor mega nourishment. Aeolian Research, *24:93–104. doi:10.1016/j.aeolia.2016.12.003.*

3.1 INTRODUCTION

The Sand Motor (or Sand Engine) is an innovative solution to counteract the anticipated coastal recession due to sea level rise (Stive et al., 2013). The Sand Motor is a 21 Mm^3 mega nourishment along the Dutch coast that is constructed well above storm surge level and therefore largely shaped by wind. While the Sand Motor accommodates fetches up to 1.0 km and is permanently exposed to wind, the dry surface area is remarkably stable (Hoonhout and de Vries, 2017a). An armor layer consisting of shells, pebbles and cobbles prevent erosion by wind and thus limit the sediment availability (following the definition of Kocurek and Lancaster, 1999). Consequently, the aeolian sediment transport rates at the Sand Motor are limited to approximately 35% of the wind transport capacity (Hoonhout and de Vries, 2017a) making the Sand Motor an availability-limited coastal system.

In an availability-limited coastal system, not the wind transport capacity, but the sediment availability governs the sediment supply towards the dunes (Houser and Ellis, 2013). Sediment availability can be limited by various bed surface properties, like shells, salt crusts, moisture and vegetation. Studies on the influence of bed surface properties on aeolian sediment availability and transport started as wind tunnel experiments (e.g. Belly, 1964; Howard, 1977; Dyer, 1986; Gillette and Stockton, 1989). These studies typically determine an adapted threshold velocity that relates the theoretical wind transport capacity to a measured sediment transport capacity (Bagnold, 1937a). In the field, the influence of different bed surface properties on sediment availability cannot easily be distinguished and the sediment availability is often presented spatially aggregated (Jackson and Nordstrom, 1998; Arens et al., 2001; Wiggs et al., 2004). The concept of critical fetch is a widely used approach for spatial aggregation of sediment supply (e.g. Jackson and Cooper, 1999; Davidson-Arnott et al., 2005, 2008; Bauer et al., 2009). The critical fetch is the distance over which the saltation cascade develops and aeolian sediment transport becomes saturated (Bauer and Davidson-Arnott, 2002). Since the saltation cascade develops slower when sediment is scarce, the critical fetch is inversely proportional to the sediment supply (Delgado-Fernandez, 2010).

Expressing the sediment supply in terms of critical fetch assumes that saturated transport is reached if the available fetch is sufficient. Hoonhout and de Vries (2017a)

showed that sediment supply can be severely limited even with fetches as large as at the Sand Motor. Consequently, critical fetches may become very large or even undefined and the definition and interpretation of the critical fetch impractical (Lynch et al., 2016; de Vries et al., 2014a). Moreover, significant spatial variations in sediment supply were found in the Sand Motor region that challenges the spatial aggregation of sediment availability. Alternatively, aeolian sediment transport is expressed in terms of local sediment availability without the need for spatial aggregation (de Vries et al., 2014b; Hoonhout and de Vries, 2016b). Such approach would require detailed measurements on spatiotemporal variations in aeolian sediment availability.

This paper presents detailed measurements of aeolian sediment transport rates from the Sand Motor during a six week field campaign in the fall of 2014. Spatial differences in sediment transport rates reveal the main erosion and deposition areas of aeolian sediment. Temporal variations in aeolian sediment transport are still expected to be correlated with the wind speed, but spatial variations are expected to be correlated with local variations in sediment availability. Understanding local sediment availability ultimately helps improving gross aeolian sediment transport estimates in availability-limited coastal systems.

3.2 FIELD SITE

The Sand Motor mega nourishment was constructed in 2011 along the Delfland coast in The Netherlands (Figure 3.1, Stive et al., 2013). The Delfland coast was originally characterized by an alongshore uniform profile with an average dune height of 13 m, a dune foot at about 5 m+MSL and a beach slope of about 1:40.

The Sand Motor is constructed as a 21 Mm^3 hook-shaped peninsula that initially protruded about 1 km into the sea and stretched over approximately 2 km alongshore. The original crest height of the Sand Motor was on average about 5 m+MSL and locally 7 m+MSL; both are well above common surge level. Consequently, a significant part of the Sand Motor is uniquely shaped by aeolian processes that redistribute significant amounts of sediments within the Sand Motor region (Hoonhout and de Vries, 2017a).

Sand used for construction of the Sand Motor is medium sand with a median diameter of about 350 μm. The sand is obtained from an offshore borrowing pit in the North Sea and contains many shells and some pebbles, cobbles and other non-erodible material.

The predominant wind direction is south to southwest. Storms have a tendency to be oriented either southwest or northwest. Also the sediment transport potential (Ψ), defined as:

$$\Psi \propto \int u^3 \, dt \tag{3.1}$$

in which u is the wind speed, is predominantly southwesterly or northwesterly oriented. The northwesterly storms are generally accompanied with significant surges as the North Sea is virtually unbounded in northwesterly direction (Figure 3.1b).

The contour of the Sand Motor changed significantly in the four years after construction. Tidal forces diffuse about 1 Mm^3 per year along the coast (de Schipper

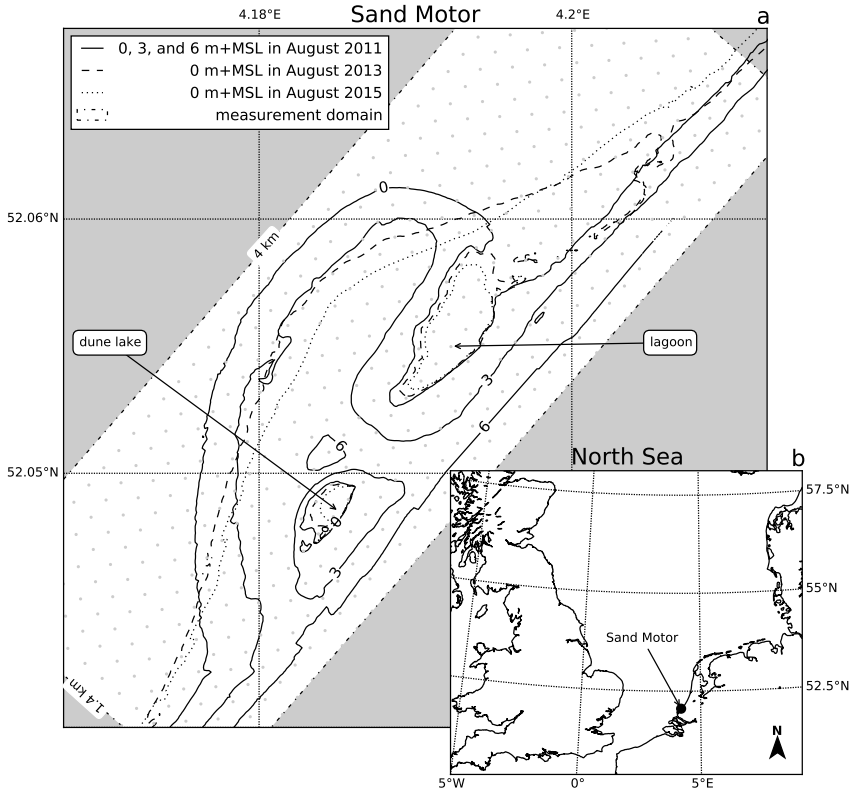

Figure 3.1: Location, orientation, appearance and evolution of the Sand Motor between construction 2011 and 2015. The box indicates the measurement domain used in the remainder of this paper. A 100 x 100 m grid aligned with the measurement domain is plotted in gray as reference.

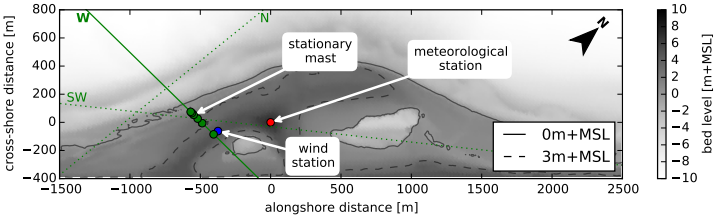

Figure 3.2: Overview of measurement transects N, W, and SW and locations during the MegaPEX field campaign.

et al., 2016). Four years after construction, the peninsula protrudes about 800 m into the sea and stretches over 4 km alongshore (Figure 3.1).

The Sand Motor provides a unique opportunity to perform measurements on spatial variations in aeolian sediment availability and transport. It accommodates vast and armored beaches next to dynamic intertidal beaches of varying width, while limitations in fetch are negligible.

3.3 METHODOLOGY

Sediment transport measurements were performed to investigate the role of the southern intertidal beaches as supplier of aeolian sediment in the Sand Motor region (Hoonhout and de Vries, 2017a). The change in sediment transport in downwind direction (spatial gradient) was measured along cross-shore transects running from the water line until the dry beach at approximately 5 m+MSL. Spatial gradients in saltation transport are positive in areas with net erosion and negative in areas with net deposition of sediment. The measurements were performed during the six week field campaign MegaPEX (Mega Perturbation EXperiment) from September 17, 2014 until October 23, 2014.

3.3.1 *Equipment*

The measurement set-up consists of 8 masts with battery power and data loggers. Each mast was equipped with at least three Wenglor fork laser sensors (P/N: YH08PCT8) for saltation measurements at 3, 10 and 25 cm above the bed (Figure 3.3). An additional three laser sensors were added to the most landward mast at 40, 55 and 70 cm above the bed to estimate the amount of particles bypassing the lower three sensors. Other masts could be equipped with three additional laser sensors as well. All except the lowest sensor were placed horizontally with the arms directed towards the wind as to minimize the disturbance of the wind field. The lowest sensor was placed vertically with the arms directed upwards, and partially buried as to further

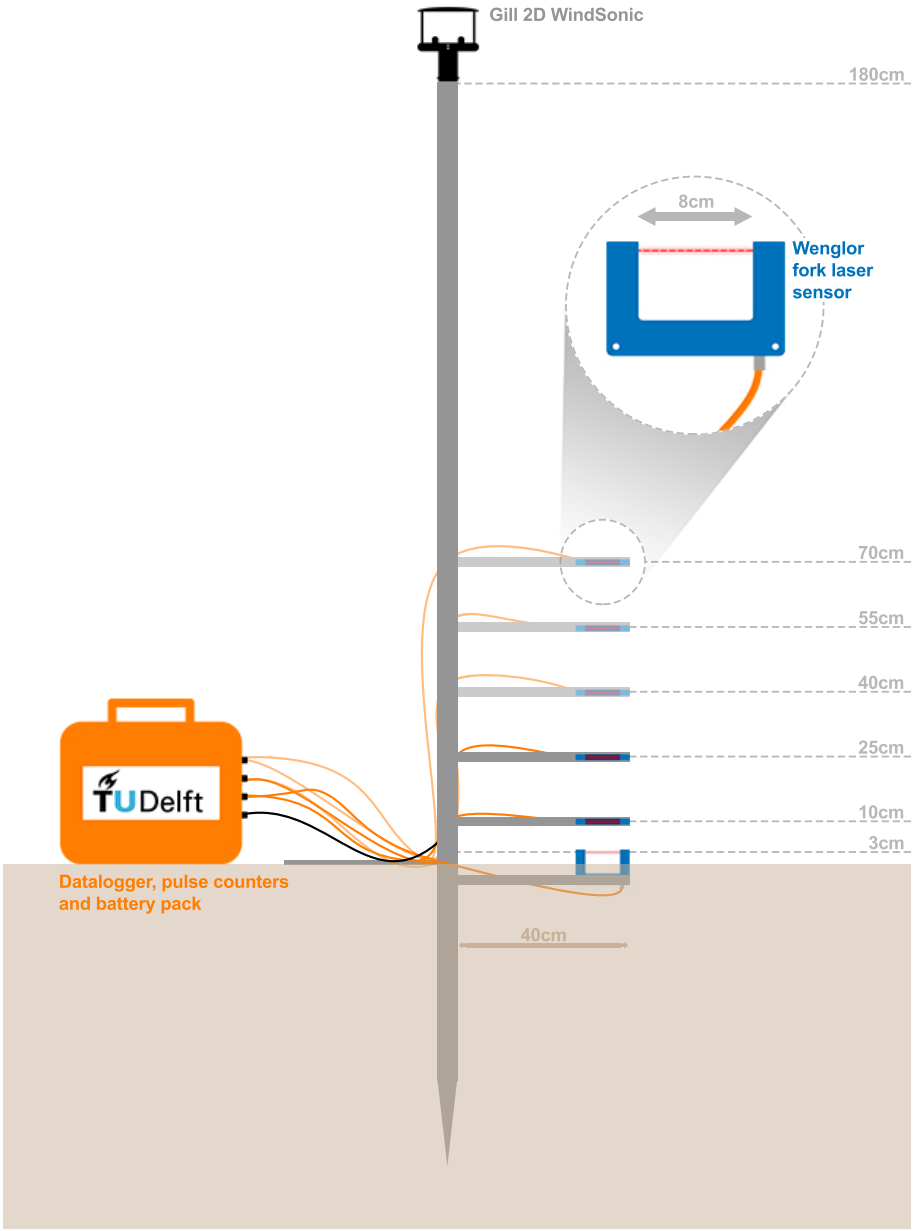

Figure 3.3: Mast with 6 Wenglor fork laser sensors and a Gill 2D WindSonic ultrasonic wind speed and direction sensor viewed in direction of the wind. The top 3 laser sensors are optional.

minimize the disturbance of the wind field. The Wenglor fork laser sensors register passing particles of 50 µm and larger with a frequency of 10 kHz using a laser beam of 0.6 mm. As the particle count is linearly related to the sediment flux (Hugenholtz and Barchyn, 2011), both are used indiscriminately in this study. The particle count is accumulated by a HOBO pulse counter (P/N: S-UCC-M001). A HOBO Energy data logger (P/N: H22-001) logged all sensors, including the pulse counters, at 1 Hz. In addition, three masts were equipped with a Gill 2D WindSonic ultrasonic wind speed and direction sensor (P/N: 1405-PK-040) at a height of 180 cm above the bed.

The masts can be rotated, but are not self-rotating to the wind as the masts were relocated depending on the wind direction. One stationary mast was present during almost the entire field campaign (Figure 3.2).

A separate Eijkelkamp wind station with three cup anemometers (P/N: 16.98.31) at heights 50, 100 and 180 cm and a wind vane (P/N: 16.98.34) at height 180 cm was present at a stationary location at the high beach for the entire duration of the field campaign. A Campbell Scientific meteorological station was present at the heart of the Sand Motor providing measurements on precipitation, humidity, solar radiation and wind speed and direction (Figure 3.2).

Qualitative small scale measurements on bed level change were performed by pressing erosion pins (nails) in the beach with falling tide. The erosion pins were placed along a cross-shore transect and about 10 cm apart with their heads flush to the bed. The erosion around the pins was measured manually with a ruler at the onset of flood.

Daily topographic surveys are performed along cross-shore transects using a Leica Viva GS10 RTG-GPS receiver. Offshore water levels and wave heights are obtained from gauges at the permanent offshore Europlatform.

3.3.2 *Deployments*

The measurement masts were deployed continuously during the field campaign, but have been relocated according to the governing wind direction. An overview of the measurement locations is given in Figure 3.2.

A single measurement transect consists of at least four masts: two in the intertidal beach area in order to capture the entrainment rate from the assumed sediment source region, one above the high water mark to capture the sediment flux from the intertidal beach area onto the dry upper beach and one higher up the beach to capture any additional sediment supply from the dry beach itself.

Table 3.1 lists the partitioning of the field campaign in 10 deployments with constant location and orientation of the measurement equipment. Most deployments were located along the westerly transect at the southern flank of the Sand Motor (Figure 3.2). Deployments DN02a and DN06a were aligned along alternative transects concurrent with deployments DN02b and DN06b respectively. During deployment DN11 all masts were clustered at high grounds as to provide a safe buffer from the expected surge during the storm event of October 23. Consequently, no transport gradients were measured during deployment DN11.

Table 3.1: Deployments of measurement masts during the MegaPEX field campaign. Maximum measured wind speeds are in parentheses.

	wind speed [m/s]	wind direction [°]	laser direction [°]	transect	duration [h]	sensors [-]	well oriented* [%]
DN02a	3 (10)	358	262	W	22	3	0
DN02b	3 (10)	359	360	N	22	3	100
DN04	5 (13)	343	360	W	42	3	92
DN05	3 (15)	196	270	W	312	3	40
DN06a	5 (17)	166	225	SW	170	3	55
DN06b	5 (17)	180	225	W	170	3	77
DN08	5 (16)	199	225	W	160	6	89
DN09	9 (21)	240	270	W	32	6	87
DN10	15 (22)	301	315	W	9	6	100
DN11	10 (24)	322	315	-	25	6	44

* The last column indicates the percentage of time in which the laser sensors were well oriented with respect to the wind. Raw data from all deployments is publishes as Hoonhout et al. (2016b). DN01 is omitted from this list as it involved a test run of the equipment only. DN02a is listed only for convenience when interpreting the published dataset. DN02b and DN06b were originally named DN03 and DN07 respectively and can be found by these names only in the published dataset.

3.3.3 *Data analysis*

Particle count time series obtained from individual Wenglor laser sensors are summed up

1. per mast, to obtain *per-mast* particle count time series for each measurement mast, and

2. over all masts, to obtain *overall* particle count time series over all measurement masts.

The per-mast particle counts are totaled rather than averaged, and therefore not corrected for the number of Wenglor laser sensors per mast. All masts deployed simultaneously in a single transect were equipped with an equal number of sensors. Only the most landward mast in the westerly transect was permanently equipped with six sensors. However, the upper three sensors of the latter mast registered negligible particle counts. Averaging would result in approximately halving the per-mast particle counts. The halving of the particle count does not reflect any physical behavior and is therefore averted. Particle count time series are interchangeably referred to as particle count rates as the measurement interval was 1 Hz.

The overall particle count time series are used for comparison with the governing wind speed. For comparison with the wind direction per-mast particle count time series are discretized in bins according to the governing wind direction and subsequently summed over time. Also for comparison with water and bed levels, the per-mast particle count time series are discretized in bins and summed over time. Discretization is then done according to the global water level and local bed level at the measurement location.

Horizontal gradients in particle counts are computed from the per-mast particle count time series and the distance between the measurement masts. Vertical distributions in particle counts are computed from the per-sensor particle count time series for each measurement mast.

Particle counts are converted into sediment fluxes following Barchyn et al. (2014a):

$$q_{wenglor} = n_{wenglor} \left(\frac{6 \cdot \gamma}{\rho \pi D^3} \cdot l_{fork} \cdot (l_{laser} + D) \right)^{-1} \tag{3.2}$$

with $\rho = 2650$ kg/m^3, $l_{fork} = 8 \cdot 10^{-2}$ m, $l_{laser} = 6 \cdot 10^{-4}$ m, $D = 335$ $^-$m and $\gamma = 1$.

Variations in wind direction of more than 45^o resulted in adjustment of the orientation of the Wenglor fork laser sensors. Particle counts with a discrepancy between wind direction and laser orientation ($\Delta\theta_u$) of more than 60^o are considered not well oriented and are discarded from the presented analysis. Other particle counts (n_{pc}) are corrected for orientation inaccuracies ($\hat{n}_{pc}$) using the basic geometric correction:

$$\hat{n}_{pc} = \frac{n_{pc}}{\cos(\Delta\theta_u)} \tag{3.3}$$

Periods without significant particle counts are not discarded from the analysis, except for the determination of the average wind direction as the wind direction tends to show random behavior for low wind conditions. The last column in Table 3.1 states the percentage of time in the laser sensors were well oriented with respect to the wind direction.

3.4 RESULTS

The conditions during the field campaign were characterized by calm and sunny weather and negligible precipitation, which is unusual for the time of the year. The average wind speed over the entire experiment was 6 m/s (Figure 3.4a). The maximum wind speed was registered at 24 m/s at the end of the campaign on October 23 during the only measured storm event (DN10). The average overall particle count rate over the entire experiment was 120 s^{-1} or < 0.1 kg/m^2/s averaged over all deployed sensors (Figure 3.4b). The maximum overall particle count rate was registered on October 7 at 5800 s^{-1} or 4 kg/m^2/s (DN06b). Therefore, the maximum registered overall particle count rate did not coincide with the maximum wind speed.

The experiment covered two spring-neap cycles with a tidal range varying between 1.5 and 2.0 m (Figure 3.4c). The maximum still water level of 2.8 m+MSL was measured during storm deployment DN11 on October 22. This surge flooded the southern flank of the Sand Motor up to 5 m+MSL.

3.4.1 *Relation between sediment transport and wind speed and water level*

Periods with low wind conditions seem to coincide with periods with a negligible overall particle count, whereas periods with fair wind conditions seem to coincide with periods with a significant overall particle count (Figure 3.4a,b). Also the occurrence of peaks in overall particle count show a correspondence with peaks in wind speed. However, the highest peaks in wind speed do not necessarily coincide with the

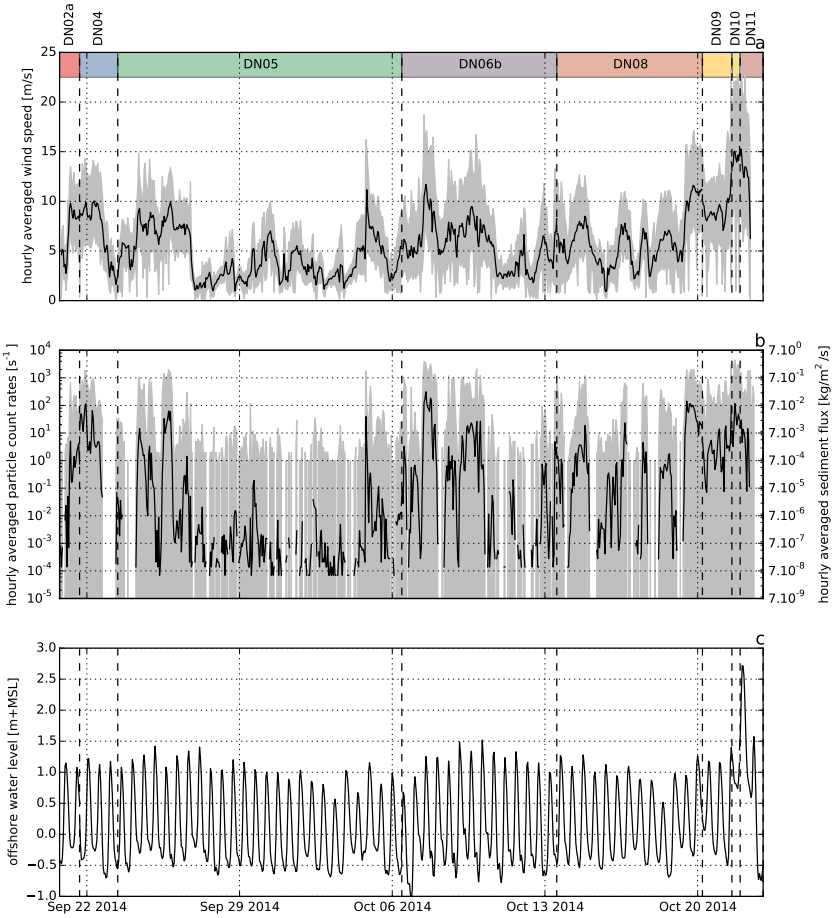

Figure 3.4: a) Wind time series, b) overall particle count rates during the deployments along the westerly transect, and c) offshore tidal elevation. Grey lines indicate the raw data, black lines the hourly averaged data. Colored bars refer to the deployments listed in Table 3.1. Deployments DN02b and DN06a are not included as these are located along different transects.

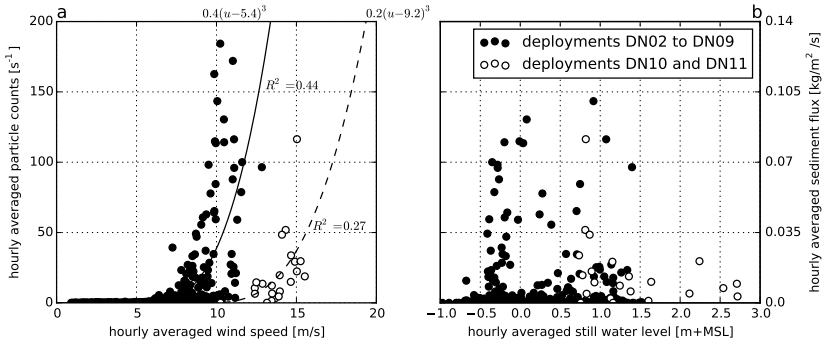

Figure 3.5: a) Relations between overall particle count and wind speed or b) water level. Closed circles and continuous lines refer to non-storm deployments DN02 to DN09. Open circles and dashed lines refer to storm deployments DN10 and DN11. All deployments are listed in Table 3.1.

highest peaks in overall particle count, resulting in an overall poor correlation between wind speed and overall particle count (Figure 3.5a). The poor correlation is reflected in a Spearman rank correlation coefficient (Spearman, 1904) of zero, indicating that the data cannot be described by a monotonic function of any kind.

In the remainder of this paper it is shown that the storm deployments DN10 and DN11 provide signals with respect to wind direction, sediment availability and fetch that are consistently different from the non-storm deployments DN02 to DN09. In anticipation to these findings, correlations between wind speed and overall particle count are computed for the storm and non-storm deployments separately, resulting in a weak positive relation between wind speed and overall particle count. Fitting a third-power curve through these separate datasets results in R^2-values of 0.43 and 0.27 respectively. The low R^2-values indicate that much of the variance in the overall particle count is not explained by wind speed.

No relation between the still water level and the overall particle count is found (Figure 3.5b). There is no evidence that the spring-neap modulation of the high water level of about 0.5 m influenced the overall particle count significantly.

3.4.2 *Wind direction and sediment source areas*

The vast majority of per-mast particle counts registered at the stationary mast, that was located at the high water line during almost the entire field campaign (Figure 3.2), was registered from a limited number of wind directions. These directions do not coincide with the prevailing wind direction or the wind direction with the largest transport potential (Figure 3.6a).

Figure 3.6a shows that the prevailing wind direction was south, but that the largest transport potential (Equation 3.1) came from the southwesterly and northwesterly directions. The per-mast particle count does not align with the prevailing wind direc-

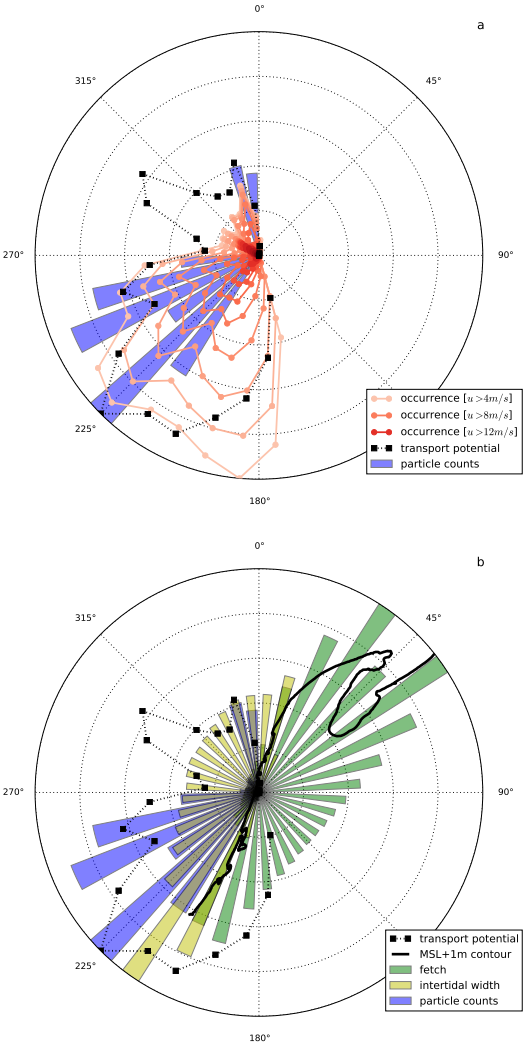

Figure 3.6: a) Per-mast particle count, wind speed and direction obtained from stationary mast (Figure 3.2) and b) available fetch and intertidal fetches.

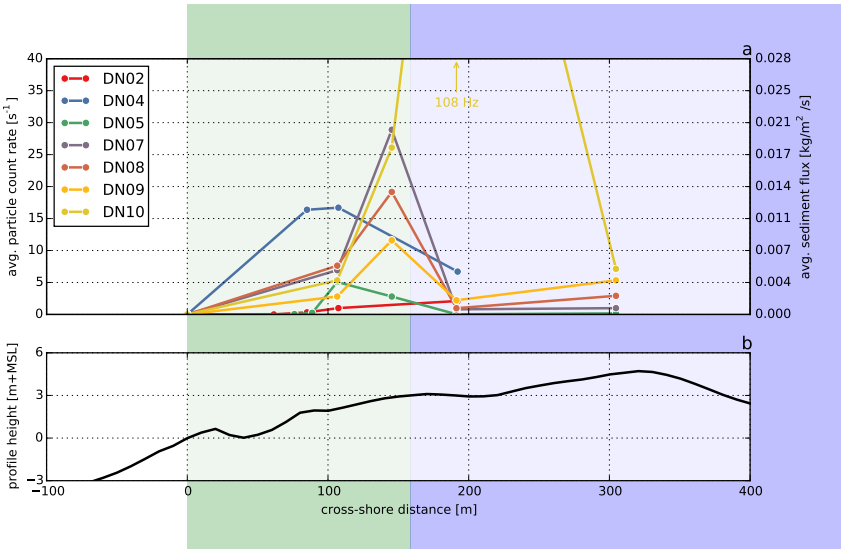

Figure 3.7: a) Average per-mast particle count rates during the deployments along the westerly transect and b) beach profile at the beginning of the field campaign. Line colors refer to the partitioning of the time series in Figure 3.4.

tion or the directions with the largest transport potential as both the southerly and northwesterly wind directions did not induce a significant particle count.

Figure 3.6b shows that most particles are registered from the wind directions with the shortest fetches. However, these wind directions provide among the largest intertidal beach widths along the Dutch coast. The exception is the northwesterly wind direction, that does accommodate a fair intertidal beach width, but did not register a per-mast particle count close to what could be expected from the transport potential. The northwesterly wind directions were solely present during the storm deployment DN10.

3.4.3 *Spatial gradients in sediment transport*

Significant variations in per-mast particle count along the measurement transects is found. Figure 3.7 shows that the largest increase in per-mast particle count in downwind direction (positive gradients) is consistently located in the intertidal beach area. Positive gradients in sediment transport indicate a net erosion of the beach surface and thus entrainment of sediment.

A significant decrease in per-mast particle count in downwind direction (negative gradients) is consistently found at the transition between intertidal and dry beach. Negative gradients in sediment transport indicate net deposition of sediment. Only during storm deployment DN10 the negative gradients at the transition were absent

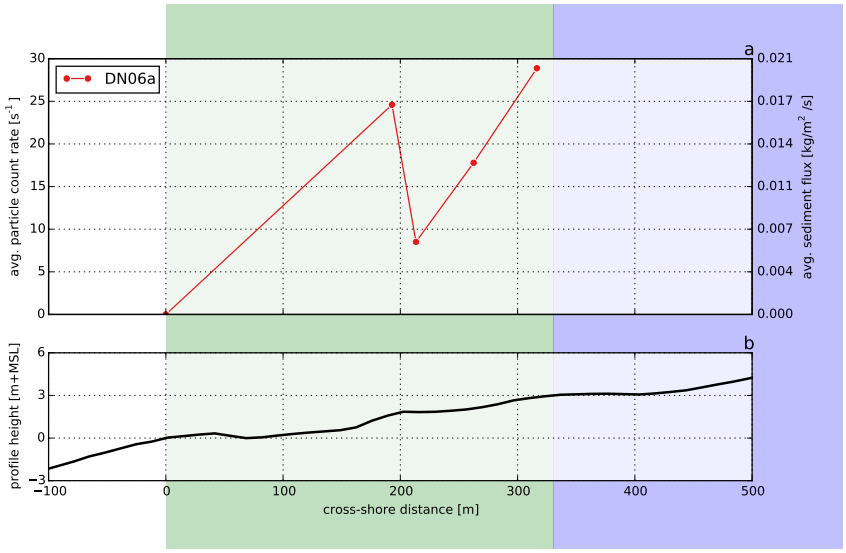

Figure 3.8: a) Average per-mast particle count rates during deployment DN06a along the southwesterly transect and b) beach profile at the beginning of deployment DN06.

and large positive gradients in both the intertidal and dry beach area were found (Figure 3.7).

The negative gradients coincide with the transition from the berm slope to the berm flat. Local deposition of aeolian sediment at the edge of a berm appears to be consistent behavior as it is also observed within the intertidal beach area. Four masts were deployed along a southwesterly transect within the intertidal beach area (DN06a, Figure 3.8) concurrent with deployment DN06b. These measurements show a significant decrease in per-mast particle count over a minor berm-like feature (x = 200 m) in the intertidal beach area. Downwind of this feature the per-mast particle count increased again with a rate comparable to what was found upwind of the berm-like feature. In addition, small scale measurements on bed level change confirm that erosion by wind is concentrated on the berm slope (Figure 3.9), while the berm flat tends to accrete. The maximum erosion of 1.2 cm in a single tidal cycle was measured with wind speeds above 10 m/s and little precipitation.

Measured negative gradients might also be caused by sediment locally bypassing the measurement equipment. To ensure that the number of bypassing particles is limited, the most landward mast in each transect was permanently equipped with six laser sensors up to 70 cm above the bed. The number of particles counted in the upper laser sensor was consistently low ($\leqslant 1\%$), suggesting that only a small number of particles bypassed the equipment at this point.

At the location downwind of the negative gradients more sediment might have bypassed than at the most landward measurement location. During deployment DN08 all four masts were equipped with six laser sensors in order to capture the vertical distribution of the particle count across the beach (Figure 3.10). It appears that the cen-

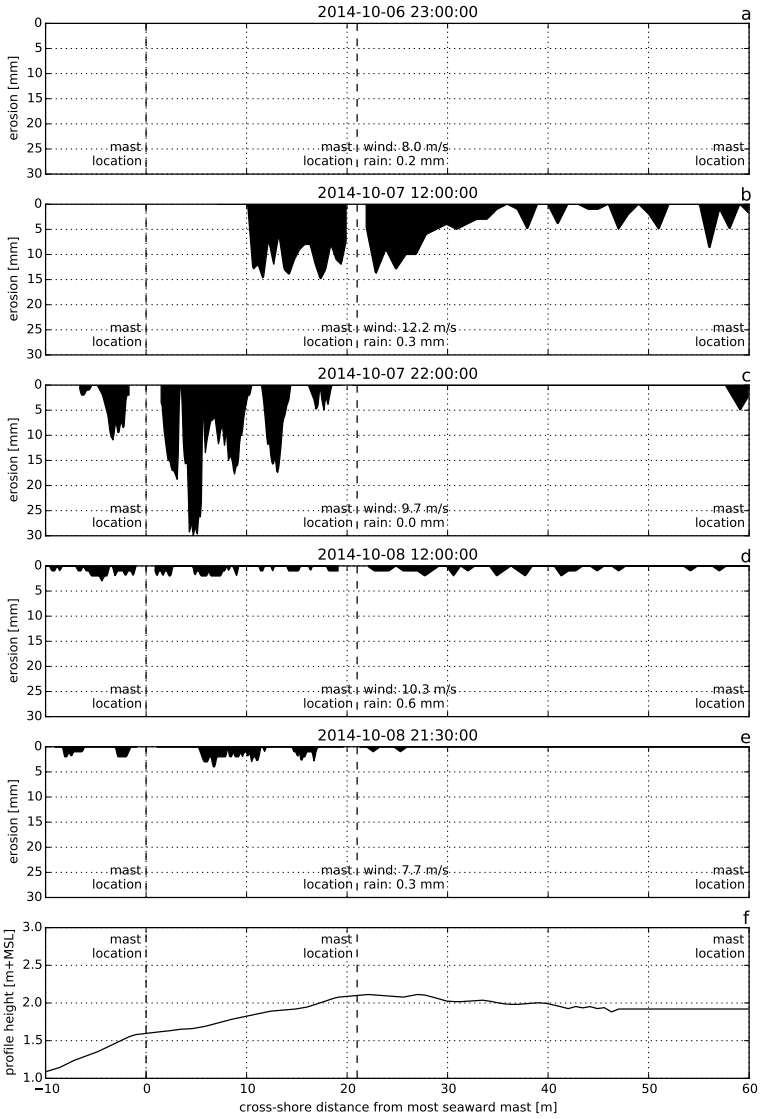

Figure 3.9: Erosion measured using erosion pins during five tidal cycles during deployment DN06a along the southwesterly transect.

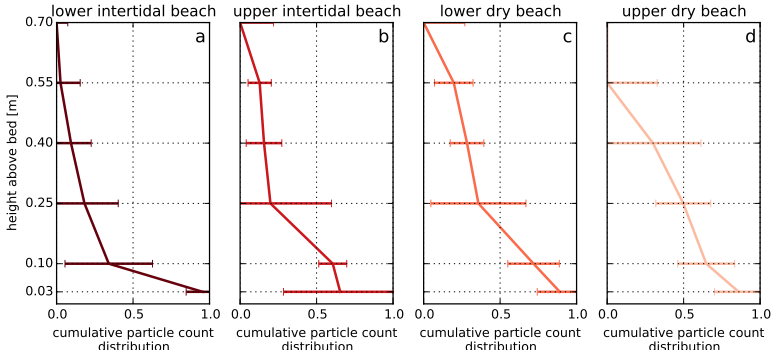

Figure 3.10: Cumulative particle count distribution over the vertical during deployment DN08. The line indicates the percentage of particles that bypasses a certain height above the bed. The horizontal bars visualize the variability in time of the particle count per laser sensor.

ter of gravity of the particle count moves upward in downwind direction.Downwind of the negative transport gradient the percentage of particles counted by the upper laser sensor is 20% compared to $\leqslant$ 10% at the other locations, suggesting that most particles bypassed at this location. The difference between the fraction of bypassing particles is too small to explain the large negative gradients, but are likely to cause the measured negative gradients to be overestimated.

3.4.4 *Fetch vs. sediment availability*

In Figure 3.11 the overall particle count obtained during the field campaign is binned according to the prevailing wind speed and the bed level at the measurement location. The average still water level is an indication of available fetch. The peak in overall particle count is at 3 m+MSL irrespective of the wind speed and available fetch. Therefore the overall particle count seems to be limited by location rather than wind speed or available fetch. The specific location at which the particle count peaks corresponds to the high water line and the onset of the shell pavement that largely covers the dry beach.

3.5 DISCUSSION

The positive gradients in per-mast particle count in the intertidal beach area and minor positive gradients in the dry beach area suggest that the intertidal beach is a primary source of aeolian sediment in the Sand Motor region. This observation is in accordance with the large scale sediment budgets of the Sand Motor region (Hoonhout and de Vries, 2017a). Armoring of the dry beach surface, due to formation of lag deposits, might lead to a significant reduction in local aeolian sediment availability. Similarly, sediment availability might also be limited in the intertidal beach area due to periodic flooding and consequently high soil moisture contents. From the differences in per-

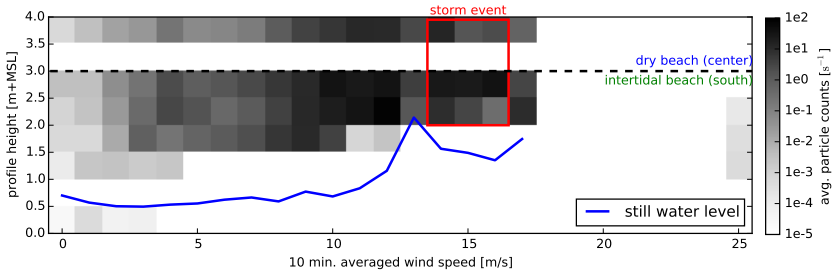

Figure 3.11: Average overall particle count rates depending on governing wind speed and bed level at measurement location, and average still water level depending on governing wind speed.

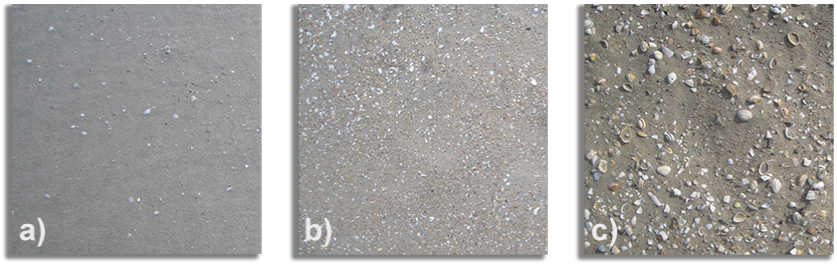

Figure 3.12: Visual impression of armor layer at three locations in the Sand Motor region: a) intertidal beach, no armoring b) lower dry beach, minor armoring with shell fragments c) upper dry beach, severe armoring with many shells and coarse sand. Covered surface is approximately 40 x 40 cm in all cases.

mast particle count gradients between the intertidal and dry beach it can be assumed that the reduction of sediment availability due to armoring outweighs the influence of soil moisture. Local differences in bed surface properties would therefore induce relative differences in sediment availability that govern aeolian sediment transport in the Sand Motor region.

The negative gradients in per-mast particle count at the transition between intertidal and dry beach indicate that sediment eroded from the intertidal beach is deposited locally on the dry beach. Morphological feedback with the wind might cause the sediment transport capacity to peak at the berm edge due to the presence of a locally accelerated wind (i.e. jet flow; Hesp and Smyth, 2016), resulting in deposition at the berm flat. In addition, the berm edge coincides with the visually observed onset of a shell pavement (Figure 3.12). The shell pavement emerged from the nourished sediment in the first half year after construction of the Sand Motor (Hoonhout and

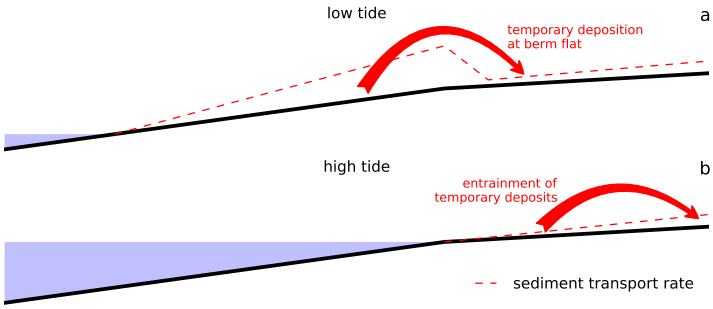

Figure 3.13: Conceptual illustration of how temporal deposits facilitate a continuous sediment supply from the intertidal beach to the dunes.

de Vries, 2017a) due to winnowing of sand from the bed. Roughness elements, like shells and cobbles, might trap impacting grains, and hamper saltation, or cause fully elastic collisions, and enhance saltation. The shell pavement at the measurement locations is relatively open and therefore both processes are likely to be relevant. The consistent negative gradients in particle count at the onset of the shell pavement suggest that trapping of sediment is dominant over the enhancement of saltation due to fully elastic collisions.

The local deposition of sediment at the berm flat is temporary as no accumulation of sand is observed on top of the shell pavement during the MegaPEX field campaign. This suggests that sediment supply from marine sources and deposition in dunes, dune lake and lagoon is a phased process. In a phased system the local sediment deposits at the berm flat might act as temporary sediment source during high water (Figure 3.13). Consequently, measured aeolian sediment transport rates would be continuous and independent of the instantaneous water level. The phasing of erosion and deposition can therefore explain the weak correlations between measured overall particle count and the instantaneous water level, which seemed to contrast the conclusion that the intertidal beach is a primary source of aeolian sediment.

The phasing of erosion and deposition increases the duration of transport from the intertidal beach to the dunes. The environmental conditions therefore needs to be favorable for aeolian sediment transport over a longer period for the sediment to reach the dunes. This requirement for dune growth closely relates to the need for synchronization between sediment availability and wind transport capacity emphasized by Houser (2009); Anthony (2013).

During a high wind event the relative importance of limitations in sediment availability might change. Strong winds can mobilize even the largest sediment fractions and shell fragments. Consequently, the beach armor layer itself might be transported and its reducing effect on sediment availability might be (partially) neutralized. Also the trapping of sediment due to an increase in bed roughness might be less effective and the influence of the berm on the wind flow reduced. In addition, high wind events are regularly accompanied with surges that prevent erosion of the intertidal beach by wind. Instead, the wind energy can be used for erosion of the dry beach,

which contributes to the removal of the beach armor layer. The surge itself might also remove the beach armor layer by wave action or bury it by deposition of marine sediments. The removal or burial of the beach armor layer might elevate sediment availability from the dry beach also after the the storm passed. Only after development of a new beach armor layer the sediment availability and transport rates then equal the pre-storm situation.

The significant spatial variations in sediment transport gradients reflect significant variations in aeolian sediment availability. The formation of beach armor layers is known to limit aeolian sediment availability (McKenna Neuman et al., 2012) and cause spatial variations in aeolian sediment supply (Jackson et al., 2010). In case of the Sand Motor the formation of the beach armor layer is particularly accommodated by:

1. the high number of shells and other roughness elements that is generally contained by nourishment sand (van der Wal, 1998, 2000), and

2. the high construction height of the Sand Motor.

As the majority of the Sand Motor's subaerial surface has never been influenced by hydrodynamics, the beach surface in these areas is never reworked. Consequently, the majority of the Sand Motor's subaerial surface does not directly contribute to dune growth or beach-dune interactions (Houser and Ellis, 2013). The vast beach surface seems to stimulate dune growth only indirectly by sheltering the dunes from storm erosion.

Large scale nourishments are typically presented as natural solution to improve coastal safety. The natural dynamics of beach-dune systems depend on the periodic reworking of the beach surface as it prevents the formation of lag deposits. Large scale nourishments with a construction height above regular storm level can disrupt these natural dynamics as the formation of lag deposits is accommodated. The resulting compartmentalization of the beach can result in a phased process that decelerates dune growth and make dune growth more dependent on incidental storm events. Besides, also marine erosion would likely be limited, contributing to the lifetime of the nourishment. In contrast, limiting the construction height of large scale nourishments would reduce the lifetime of a nourishment, but result in a larger source area of aeolian sediment and the stimulation of dune growth and natural beach-dune interactions.

3.6 CONCLUSIONS

The Sand Motor (or Sand Engine) is a 21 Mm^3 mega nourishment along the Dutch coast that is constructed well above storm surge level (Stive et al., 2013) and therefore largely shaped by wind. During the six week MEGAPEX field campaign in the fall of 2014, spatial gradients in aeolian sediment transport were measured. The gradients identified the intertidal beach as the primary source of aeolian sediment. In addition, local temporal deposition of sediment at the berm flat occurred. The deposition is likely caused by a combination of morphological feedback with the wind and an increase in bed roughness due to the presence of a shell pavement. The local deposition of sediment causes the transport of sediment from intertidal beach to dunes, dune lake and lagoon to be phased.

From the measurements the following conclusions can be drawn:

1. In the Sand Motor region, the (southern) intertidal beach area is a more important source of aeolian sediment than the dry beach area.

2. The relative importance of the intertidal beach as supplier of aeolian sediment could be explained by the development of a beach armor layer in the dry beach area that outweighs the influence of high soil moisture contents in the intertidal beach area.

3. Aeolian sediment originating from the intertidal beach seems to settle on the berm flat and to be gradually transported further resulting in an continuous sediment flux from the intertidal beach area and into the dunes, even if the intertidal beach is flooded.

4. During high wind events, aeolian sediment availability in the intertidal beach area tends to be reduced by high water levels, while the sediment availability in the dry beach area tends to be increased due to mobilization of the beach armor layer;

5. The construction height of a mega nourishment is important to its lifetime as it is governs compartmentalization of the beach due to beach armoring.

Part II

NUMERICAL MODELING

Inspired by the field observations a numerical model is developed and applied to hindcast the sub-aerial morphological evolution of the Sand Motor for the 4 years after construction.

4

NUMERICAL MODEL

This chapter is based on another publication: Hoonhout, B. M. and de Vries, S. (2016b). A process-based model for aeolian sediment transport and spatiotemporal varying sediment availability. Journal of Geophysical Research: Earth Surface. *doi:10.1002/2015JF003692. 2015JF003692.*

The numerical implementation of the model presented in this chapter and experimental features not discussed are elaborated in Appendix B.

4.1 INTRODUCTION

Aeolian sediment transport is influenced by a variety of bed surface properties that are commonly found in coastal environments, like: moisture, shells, strandlines, salt crusts, bed slopes, vegetation, non-erodible elements and antropogenic disturbances. The bed surface properties influence aeolian sediment transport by changing the sediment transport capacity and/or the sediment availability (Kocurek and Lancaster, 1999). In current aeolian sediment transport models the effects on the sediment transport capacity and sediment availability are generally incorporated through a single parameter: the velocity threshold. This approach appears to be a critical limitation in existing aeolian sediment transport models for simulation of real-world cases with spatiotemporal variations in bed surface properties.

The velocity threshold was introduced by Bagnold (1935), and incorporated in his initial aeolian sediment transport model (Bagnold, 1937b) according to:

$$\underbrace{q_{sat}}_{\substack{\text{sediment}\\ \text{transport}\\ \text{capacity}}} = \alpha \underbrace{C\frac{\rho_a}{g}\sqrt{\frac{d_n}{D_n}}}_{\substack{\text{properties}\\ \text{of sediment}\\ \text{in transport}}} (u_z - u_{th})^3 \tag{4.1}$$

in which q_{sat} [kg/m/s] is the equilibrium or saturated sediment transport rate and represents the sediment transport capacity. u_z [m/s] is the wind velocity at height z [m] and u_{th} the velocity threshold [m/s]. The properties of the sediment in transport are represented by a series of parameters: C [–] is a parameter to account for the grain size distribution width, ρ_a [kg/m^3] is the density of the air, g [m/s^2] is the gravitational constant, d_n [m] is the nominal grain size and D_n [m] is a reference grain size. α is a constant to account for the conversion of the measured wind velocity to the near-bed shear velocity following Prandtl-Von Kármán's Law of the Wall: $\left(\frac{\kappa}{\ln z/z'}\right)^3$

in which z' [m] is the height at which the idealized velocity profile reaches zero and κ [-] is the Von Kármán constant. Many studies following the work of Bagnold (1937b) effectively proposed different parameterizations for sediment properties (e.g. Owen, 1964; Hsu, 1971; Sørensen, 2004) or changed the weight of the velocity threshold (e.g. Kawamura, 1951; Lettau and Lettau, 1978). However, the characteristic structure and application of these models stayed essentially the same.

Sherman et al. (1998) and Sherman and Li (2012) summarized the performance of eight aeolian sediment transport models compared to field measurements on a sandy beach. All the models systematically overpredict the measured aeolian sediment transport rates, which is in agreement with other coastal field studies (e.g. Jackson and Cooper, 1999; Lynch et al., 2008; Davidson-Arnott and Bauer, 2009; Aagaard, 2014). Besides, the original model of Bagnold (1937b) appeared to outperform the models of later date. In an attempt to explain the poor performance of aeolian sediment transport models in coastal environments, many authors emphasized the importance of bed surface properties. Typical bed surface properties that are found along the coast and assumed to explain at least partially the poor performance of aeolian sediment transport models are high moisture contents (e.g. Wiggs et al., 2004; Davidson-Arnott et al., 2008; Darke and McKenna Neuman, 2008; McKenna Neuman and Sanderson, 2008; Udo et al., 2008; Bauer et al., 2009; Edwards and Namikas, 2009; Namikas et al., 2010; Scheidt et al., 2010), salt crusts (e.g. Nickling and Ecclestone, 1981), bed slopes (e.g. Iversen and Rasmussen, 2006), vegetation (e.g. Arens, 1996; Lancaster and Baas, 1998; Okin, 2008; Li et al., 2013; Dupont et al., 2014), shell pavements (e.g. van der Wal, 1998; McKenna Neuman et al., 2012) and sorted and armored beach surfaces (e.g. Gillette and Stockton, 1989; Gillies et al., 2006; Tan et al., 2013; Cheng et al., 2015). The influence of these bed surface properties on aeolian sediment transport has been investigated and often resulted in modified values for the velocity threshold (e.g. Howard, 1977; Dyer, 1986; Belly, 1964; Johnson, 1965; Hotta et al., 1984; Nickling and Ecclestone, 1981; Arens, 1996; King et al., 2005).

A critical limitation of the use of the velocity threshold alone to cope with the influence of bed surface properties is that it changes inherently in time and space (Stout, 2004) and that it accounts for two fundamentally different phenomena:

1. The change in the sediment transport capacity which represents the ease of sediment transport *over* a given bed; and

2. The change in sediment availability, which represents the ease of sediment entrainment *from* a given bed.

Although in uniform and constant situations, like often used in wind tunnel experiments, the difference might be negligible, in real-world field conditions it is not. The difference is most apparent when observing transport over a bed with spatial variations in bed surface properties. For example due to tidal motions in the intertidal beach area, emergence of roughness elements in the dry beach area and vegetation in the dune area. In addition, temporal variations in bed surface properties, for example due to tidal spring/neap cycles, rain showers, storm surges, seasonal variations in vegetation and progressive armoring of the beach, increase the need for simulation rather than parameterization of bed surface properties and sediment availability (as discussed in section 4.2).

This paper presents a new model approach for aeolian sediment transport. The model simulates rather than parameterizes bed surface properties and sediment availability. The model explicitly defines sediment availability following de Vries et al. (2014b) and introduces multi-fraction aeolian sediment transport in order to simulate processes that limit the availability of sediment, like beach armoring, and processes that enhance the availability of sediment, like hydraulic mixing. Consequently, the model can cope with arbitrary spatiotemporal configurations of bed surface properties. Although validation of the model is ongoing, the performance of the model is illustrated using four prototype cases, the simulation of two wind tunnel experiments from literature (Nickling and McKenna Neuman, 1995; Dong et al., 2004b) and a sensitivity analysis of newly introduced parameters.

In literature the *velocity threshold* is used interchangeably to describe the (change in) sediment transport capacity and sediment availability. In this paper the term *velocity threshold* is strictly used to describe the (change in) sediment transport capacity (Equation 4.1). The term *sediment availability* is used in accordance with the terminology proposed by Kocurek and Lancaster (1999), which is often referred to as *sediment supply* in literature.

4.2 MODEL CHALLENGES: BED SURFACE PROPERTIES

The importance of spatiotemporal variations in bed surface properties for aeolian sediment transport is most apparent when observing transport over a bed consisting of both erodible and non-erodible fractions. Many studies have investigated the influence of varying grain sizes on aeolian sediment transport. In most cases it involved studies on the influence of non-erodible or roughness elements using either field experiments (e.g. Davidson-Arnott et al., 1997; Gillies et al., 2006; Tan et al., 2013) or wind tunnel experiments (e.g. Gillette and Stockton, 1989; Nickling and McKenna Neuman, 1995; McKenna Neuman and Nickling, 1995; Dong et al., 2004b; McKenna Neuman et al., 2012) and occasionally numerical modeling (e.g. Turpin et al., 2010). The studies typically use granular material with a clear bi-modal distribution. A flat sandy surface is then partially covered by a significantly larger grain size fraction ranging from shells and gravel to pebbles and cobbles. Typically the coverage of non-erodible elements is expressed using the roughness density λ as described by Raupach et al. (1993). Raupach et al. (1993) uses the roughness density to determine the relative increase in the shear velocity threshold according to:

$$R_t = \frac{u_{*th,S}}{u_{*th,R}} = \frac{1}{\sqrt{(1 - m\sigma\lambda)(1 + m\beta\lambda)}} \tag{4.2}$$

in which $u_{*th,S}$ is the shear velocity threshold with a bare surface, $u_{*th,R}$ is the shear velocity threshold with a surface including non-erodible elements and m, σ and β are calibration coefficients that account for the size and shape of the non-erodible elements.

4.2.1 *Temporal Variations in Bed Surface Properties*

The concept of the roughness density is useful to describe the instantaneous influence of roughness elements in the bed on aeolian sediment transport. However, it does not account for the fact that roughness elements tend to emerge from the bed over time due to winnowing of fines. Following Gillette and Stockton (1989), Nickling and McKenna Neuman (1995) and McKenna Neuman and Nickling (1995) showed that the winnowing of fines and the emergence of roughness elements result in a time-dependent aeolian sediment transport rate. The time-dependency is caused by a recurrence relation between sediment transport and sediment availability. Consequently, neither the roughness density nor the sediment availability can be determined a-priori. We argue that process-based simulation of bed surface properties rather than parameterization is needed to solve the instantaneous sediment availability.

McKenna Neuman et al. (2012) shows that even small shell fragments cause a sandy surface to be armored over time. But even in the absence of non-erodible roughness elements, spatiotemporal variations in bed surface properties may develop as the transport capacity is inversely related to the grain size (Bagnold, 1937b) resulting in sediment sorting: a coarsening of the bed surface and downwind deposition of fines (Bagnold, 1937b; van der Wal, 2000; Arens et al., 2002).

4.2.2 *Spatial Variations in Bed Surface Properties*

Spatial variations in bed surface properties occur naturally in coastal environments. For example, strandlines locally cover the erodible bed and reduce the sediment availability. However, strandlines not necessarily reduce the sediment transport capacity to the same extent and may even increase the transport capacity due to fully elastic collisions with the sediment in transport. The distinction between sediment availability and sediment transport capacity in relation to bed surface properties is not offered by existing models.

Dong et al. (2004b) describes a similar situation in a wind tunnel. In their experiment a patch of gravel (10 - 40 mm) is positioned downwind of a patch of sandy material. Dong et al. (2004b) show how the gravel patch reduces the aeolian sediment transport rate downwind of the domain compared to the situation without the gravel. However, in all conditions sediment passes the patch, while sediment availability from the patch is zero. There seems to be a tendency of an increase in sediment transport rate with increasing patch size when the patch size is relatively small. This is attributed to the change in transport characteristics due to fully elastic collisions between the sand grains and the gravel. Consequently, the saltation height and rebound angle increase and in turn influence the sediment transport capacity. Only for large patch sizes the trapping of sand grains in the gravel pores becomes a dominant process resulting in a decrease in the sediment transport rate downwind of the gravel patch.

Dong et al. (2004b) acknowledged the limitations of the use of the shear velocity threshold to describe the results of his wind tunnel experiments. Therefore they introduced a factor in the aeolian sediment transport formulation of Dymin (1954) that depends on the length of the gravel patch squared. Although an important observation, the method is hardly generalizable to more realistic situations where moist

intertidal beaches are located adjacent to strandlines and armored beaches that subsequently border a vegetated dune. Therefore, to cope with spatially varying bed surface properties an aeolian sediment transport model is needed that provides a generic distinction between the effect of bed surface properties on the sediment transport capacity and sediment availability.

4.3 MODEL CONCEPTS: SEDIMENT AVAILABILITY, SATURATED TRANSPORT AND ENTRAINMENT

The sediment transport capacity and sediment availability together determine the sediment entrainment. Sediment availability differs from entrainment in that the availability defines the *potential* erosion of the bed, while the entrainment defines the *actual* erosion of the bed. If aeolian sediment transport is transport-limited, the sediment availability is larger than entrainment and not all available sediment will be transported. Consequently, entrainment is governed by the sediment transport capacity. If aeolian sediment transport is availability-limited, entrainment is equal to the sediment availability. Whether aeolian sediment transport is transport- or availability-limited depends on the balance between the sediment transport capacity and the sediment availability that are both influenced by bed surface properties. In the literature various concepts to incorporate the influence of bed surface properties in aeolian sediment transport models can be found:

1. the concept of the shear velocity threshold (e.g. Howard, 1977; Dyer, 1986; Belly, 1964; Johnson, 1965; Hotta et al., 1984; Nickling and Ecclestone, 1981; Arens, 1996);

2. the concept of critical fetch (e.g. Bauer and Davidson-Arnott, 2002; Delgado-Fernandez, 2010);

3. the concept of explicit availability (or supply; de Vries et al., 2014b).

From these concepts the shear velocity threshold is typically applied in conjunction with a formulation for the aeolian sediment transport capacity (e.g. Equation 4.1). The sediment transport capacity described by these formulations is the equilibrium or saturated sediment transport rate. The saturated sediment transport rate is the maximum transport rate reached in case of a fetch (F) beyond the critical fetch (F_c, Bauer and Davidson-Arnott, 2002). In case of abundant sediment availability and fetches beyond the critical fetch the saturated sediment transport rate seems to be an appropriate indicator for the actual sediment flux downwind of the observed domain. However, in coastal environments fetches can be limited due to limited beach widths (e.g. Jackson and Cooper, 1999; Bauer et al., 2009; Davidson-Arnott et al., 2005; Delgado-Fernandez, 2010; Dong et al., 2004a) and sediment availability is limited due to beach armoring as well as other bed surface properties. Consequently, in reality the saturated sediment transport rate is not necessarily an appropriate indicator for the sediment flux downwind of the observed domain.

The concept of critical fetch therefore introduces a measure to distinguish between saturated ($F \geqslant F_c$) and unsaturated sediment transport situations ($F < F_c$). In this approach the aeolian sediment transport rate, (critical) fetch distance, entrainment and sediment availability are related following:

$$q = \int_0^{\hat{F}} \phi(u_*, u_{*th}, m_a)\, dx \quad \text{with } \hat{F} = \min(F, F_c) \tag{4.3}$$

where q [kg/s/m] is the instantaneous sediment transport rate per unit width, F [m] is the fetch distance and F_c [m] the critical fetch distance, ϕ is the entrainment function that depends on the shear velocity u_* [m/s], the shear velocity threshold u_{*th} [m/s] and the available sediment mass m_a [kg/m^2]. x [m] is the downwind distance from a zero-transport boundary. This integral is solved for by assuming a pre-defined entrainment rate. Equation 4.3 then simplifies to:

$$q = \Phi(u_*, u_{*th}, m_a, \hat{F}) \tag{4.4}$$

where Φ is the analytically integrated solution to Equation 4.3. Delgado-Fernandez and Davidson-Arnott (2011) use the critical fetch concept to incorporate the effect of spatiotemporal variations in soil moisture. However, due to the recurrence relation in time between the aeolian sediment transport rate q and the sediment availability m_a, neither the sediment availability nor the entrainment can be determined a-priori and the integral in Equation 4.3 cannot easily be solved analytically.

Equation 4.3 can be simplified by observing the difference between availability-limited and transport-limited situations. In availability-limited situations the entrainment function simplifies to $\frac{\partial m_a}{\partial t}$, while in transport-limited situations the sediment availability is abundant. Equation 4.3 can therefore be rewritten as:

$$q = \begin{cases} \int_0^{\hat{F}} \frac{\partial m_a}{\partial t}\, dx & \text{if availability-limited} \\ \\ \int_0^{\hat{F}} \phi(u_*, u_{*th})\, dx & \text{if transport-limited} \end{cases} \tag{4.5}$$

The wind velocity can influence sediment availability indirectly through beach armoring. Given constant wind velocity, the development of a beach armor layer can turn a transport-limited situation into an availability-limited situation, which subsequently influences the instantaneous aeolian sediment transport rate. In an availability-limited situation, entrainment does not depend on the wind velocity since the wind velocity is sufficiently high to mobilize all available sediment.

The distinction between availability-limited and transport-limited situations in Equation 4.5 naturally reveals the fundamental difference between sediment availability and the sediment transport capacity and shows why these two phenomena cannot be represented by a single parameter like the shear velocity threshold. Moreover, Equation 4.5 provides an opportunity to model availability-limited and transport-limited situations separately as proposed by de Vries et al. (2014b), who uses a 1D advection formulation in combination with the concept of a spatiotemporal varying sediment availability m_a (or supply S_e according to the terminology of de Vries et al. (2014b)) to regulate the entrainment, transport and deposition of sediment by wind.

The disadvantage of the use of an explicit term for the sediment availability is that little is known about the quantitative relation between availability and the different availability-limiting bed surface properties. Moreover, also in the approach of de Vries et al. (2014b) sediment availability is not quantified by the model, but is input to the model. Due to the recurrence relation between the sediment transport rate and

sediment availability the governing input parameter to this model is unknown and the resulting instantaneous sediment transport rate cannot be computed. Therefore we propose to extend the approach of de Vries et al. (2014b) with numerical simulation of spatiotemporal varying bed surface properties and sediment availability.

4.4 MODEL DESCRIPTION

The model approach of de Vries et al. (2014b) is extended to compute the spatiotemporal varying sediment availability through simulation of the process of beach armoring. For this purpose the bed is discretized in horizontal grid cells and in vertical bed layers (2DV). Moreover, the grain size distribution is discretized into fractions. This allows the grain size distribition to vary both horizontally and vertically. A bed composition module is used to compute the sediment availability for each sediment fraction individually. This model approach is a generalization of existing model concepts, like the shear velocity threshold and critical fetch, and therefore compatible with these existing concepts.

4.4.1 *Advection Scheme*

A 1D advection scheme is adopted in correspondence with de Vries et al. (2014b) in which c [kg/m^2] is the instantaneous sediment mass per unit area in transport:

$$\frac{\partial c}{\partial t} + u_z \frac{\partial c}{\partial x} = E - D \tag{4.6}$$

t [s] denotes time and x [m] denotes the cross-shore distance from a zero-transport boundary. E and D [kg/m^2/s] represent the erosion and deposition terms and hence combined represent the net entrainment of sediment. Note that Equation 4.6 differs from Equation 9 in de Vries et al. (2014b) as they use the saltation height h [m] and the sediment concentration C_c [kg/m^3]. As h is not solved for, the presented model computes the sediment mass per unit area $c = hC_c$ rather than the sediment concentration C_c. For conciseness we still refer to c as the *sediment concentration*.

The net entrainment is determined based on a balance between the equilibrium or saturated sediment concentration c_{sat} [kg/m^2] and the instantaneous sediment transport concentration c and is maximized by the available sediment in the bed m_a [kg/m^2] according to:

$$E - D = \min\left(\frac{\partial m_a}{\partial t} \quad ; \quad \frac{c_{sat} - c}{T}\right) \tag{4.7}$$

T [s] represents an adaptation time scale that is assumed to be equal for both erosion and deposition. A time scale of 1 second is commonly used (de Vries et al., 2014b).

The saturated sediment concentration c_{sat} is computed using an empirical sediment transport formulation (e.g. Equation 4.1) where the transport rate q_{sat} is divided by the wind velocity u_z to obtain a mass per unit area (per unit width):

$$c_{sat} = \max\left(0 \quad ; \quad \alpha C \frac{\rho_a}{g} \sqrt{\frac{d_n}{D_n}} \frac{(u_z - u_{th})^3}{u_z}\right) \tag{4.8}$$

in which C [–] is an empirical constant to account for the grain size distribution width, ρ_a [kg/m^3] is the air density, g [m/s^2] is the gravitational constant, d_n [m] is the nominal grain size, D_n [m] is a reference grain size, u_z [m/s] is the wind velocity at height z [m] and α [–] is a constant to convert from measured wind velocity to shear velocity.

Note that at this stage the spatial variations in wind velocity are not solved for and hence no morphological feedback is included in the simulation. The model is initially intended to provide accurate sediment fluxes from the beach to the dunes rather than to simulate subsequent dune formation.

4.4.2 *Multi-fraction Erosion and Deposition*

The formulation for the equilibrium or saturated sediment concentration c_{sat} (Equation 4.8) is capable of dealing with variations in grain size through the variables u_{th}, d_n and C (Bagnold, 1937b). However, the transport formulation only describes the saturated sediment concentration assuming a fixed grain size distribution, but does not define how multiple fractions coexist in transport. If the saturated sediment concentration formulation would be applied to each fraction separately and summed up to a total transport, the total sediment transport would increase with the number of sediment fractions. Since this is unrealistic behavior the saturated sediment concentration c_{sat} for the different fractions should be weighted in order to obtain a realistic total sediment transport. Equation 4.7 therefore is modified to include a weighting factor $\hat{w}_k$ in which k represents the sediment fraction index:

$$E_k - D_k = \min\left(\frac{\partial m_{a,k}}{\partial t} \quad ; \quad \frac{\hat{w}_k \cdot c_{sat,k} - c_k}{T}\right) \tag{4.9}$$

It is common to use the grain size distribution in the bed as weighting factor for the saturated sediment concentration (e.g. Delft3D-FLOW Manual, 2014, section 11.6.4). Using the grain size distribution at the bed surface as a weighting factor assumes, in case of erosion, that all sediment at the bed surface is equally exposed to the wind.

Using the grain size distribution at the bed surface as weighting factor in case of deposition would lead to the behavior where deposition becomes dependent on the bed composition. Alternatively, in case of deposition, the saturated sediment concentration can be weighted based on the grain size distribution in the air. Due to the nature of saltation, in which continuous interaction with the bed forms the saltation cascade, both the grain size distribution in the bed and in the air are likely to contribute to the interaction between sediment fractions. The ratio between both contributions in the model is determined by a bed interaction parameter ζ.

The weighting of erosion and deposition of individual fractions is computed according to:

$$\hat{w}_k = \frac{w_k}{\sum_{k=1}^{n_k} w_k} \tag{4.10a}$$

$$\text{where} \quad w_k = (1-\zeta)\cdot w_k^{air} + (1-\hat{S}_k)\cdot w_k^{bed} \tag{4.10b}$$

in which k represents the sediment fraction index, n_k the total number of sediment fractions, w_k is the unnormalized weighting factor for fraction k, $\hat{w}_k$ is its normalized

counterpart, w_k^{air} and w_k^{bed} are the weighting factors based on the grain size distribution in the air and bed respectively and $\hat{S}_k$ is the effective sediment saturation of the air. The weighting factors based on the grain size distribution in the air and the bed are computed using mass ratios:

$$w_k^{air} = \frac{c_k}{c_{sat,k}} \quad ; \quad w_k^{bed} = \frac{m_{a,k}}{\sum_{k=1}^{n_k} m_{a,k}} \tag{4.11}$$

The sum of the ratio w_k^{air} over the fractions denotes the degree of saturation of the air column for fraction k. The degree of saturation determines if erosion of a fraction may occur. Also in saturated situations erosion of a sediment fraction can occur due to an exchange of momentum between sediment fractions, which is represented by the bed interaction parameter ζ. The effective degree of saturation is therefore also influenced by the bed interaction parameter and defined as:

$$\hat{S}_k = \min\left(1 \quad ; \quad (1-\zeta)\cdot\sum_{k=1}^{n_k} w_k^{air}\right) \tag{4.12}$$

When the effective saturation is greater than or equal to unity the air is (over)saturated and no erosion will occur. The grain size distribution in the bed is consequently less relevant and the second term in Equation 4.10b is thus minimized and zero in case $\zeta = 0$. In case the effective saturation is less than unity erosion may occur and the grain size distribution of the bed also contributes to the weighting over the sediment fractions. The weighting factors for erosion are then composed from both the grain size distribution in the air and the grain size distribution at the bed surface. Finally, the resulting weighting factors are normalized to sum to unity over all fractions ($\hat{w}_k$).

The composition of weighting factors for erosion is based on the saturation of the air column. The non-saturated fraction determines the potential erosion of the bed. Therefore the non-saturated fraction can be used to scale the grain size distribution in the bed in order to combine it with the grain size distribution in the air according to Equation 4.10b. The non-saturated fraction of the air column that can be used for scaling is therefore $1 - \hat{S}_k$.

For example, if bed interaction is disabled ($\zeta = 0$) and the air is 70% saturated, then the grain size distribution in the air contributes 70% to the weighting factors for erosion, while the grain size distribution in the bed contributes the other 30% (Figure 4.1, upper left panel). In case of (over)saturation the grain size distribution in transport contributes 100% to the weighting factors and the grain size distribution in the bed is of no influence. Transport progresses in downwind direction without interaction with the bed.

To allow for bed interaction in saturated situations in which no net erosion can occur, the bed interaction parameter ζ is used (Figure 4.1). The bed interaction parameter can take values between 0.0 and 1.0 in which the weighting factors for the equilibrium or saturated sediment concentration in an (over)saturated situation are fully determined by the grain size distribution in the bed or in the air respectively. A bed interaction value of 0.2 represents the situation in which the grain size distribution at the bed surface contributes 20% to the weighting of the saturated sediment concentration over the fractions. In the example situation where the air is 70% saturated such value for the bed interaction parameter would lead to weighting factors

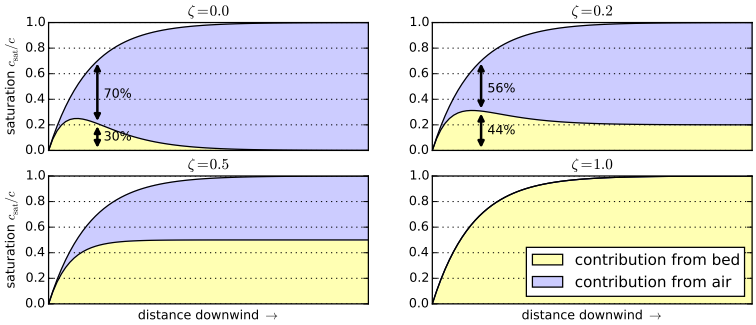

Figure 4.1: Contributions of the grain size distribution in the bed and in the air to the weighting factors $\hat{w}_k$ for the equilibrium sediment concentration in Equation 4.9 for different values of the bed interaction parameter.

that are constituted for $70\% \cdot (100\% - 20\%) = 56\%$ based on the grain size distribution in the air and for the other 44% based on the grain size distribution at the bed surface (Figure 4.1, upper right panel).

The parameterization of the exchange of momentum between sediment fractions is an aspect of saltation that is still poorly understood. Therefore calibration of the bed interaction parameter ζ is necessary. The model parameters in Equation 4.8 can be chosen in accordance with the assumptions underlying multi-fraction sediment transport. C should be set to 1.5 as each individual sediment fraction is well-sorted, d_n should be chosen equal to D_n as the grain size dependency is implemented through u_{th}. u_{th} typically varies between 1 and 6 m/s for sand.

4.4.3 *Simulation of Sediment Sorting and Beach Armoring*

Since the equilibrium or saturated sediment concentration $c_{sat,k}$ is weighted over multiple sediment fractions in the extended advection model, also the instantaneous sediment concentration c_k is computed for each sediment fraction individually. Consequently, grain size distributions may vary over the model domain and in time. These variations are thereby not limited to the horizontal, but may also vary over the vertical since fine sediment may be deposited on top of coarse sediment or, reversely, fines may be eroded from the bed surface leaving coarse sediment to reside on top of the original mixed sediment. In order to allow the model to simulate the processes of sediment sorting and beach armoring the bed is discretized in horizontal grid cells and vertical bed layers (2DV; Figure 4.2).

The discretization of the bed consists of a minimum of three vertical bed layers with a constant thickness and an unlimited number of horizontal grid cells. The top layer is the *bed surface layer* and is the only layer that interacts with the wind and hence determines the spatiotemporal varying sediment availability and the contribution of the grain size distribution in the bed to the weighting of the saturated sediment concentration. One or more *bed composition layers* are located underneath the bed surface

layer and form the upper part of the erodible bed. The bottom layer is the *base layer* and contains an infinite amount of erodible sediment according to the initial grain size distribution. The base layer cannot be eroded, but can supply sediment to the other layers.

Each layer in each grid cell describes a grain size distribution over a predefined number of sediment fractions (Figure 4.2, detail). Sediment may enter or leave a grid cell only through the bed surface layer. Since the velocity threshold depends among others on the grain size, erosion from the bed surface layer will not be uniform over all sediment fractions, but will tend to erode fines more easily than coarse sediment (Figure 4.2, detail, upper left panel). If sediment is eroded from the bed surface layer, the layer is repleted by sediment from the lower bed composition layers. The repleted sediment has a different grain size distribution than the sediment eroded from the bed surface layer. If more fines are removed from the bed surface layer in a grid cell than repleted, the median grain size increases. If erosion of fines continues the bed surface layer becomes increasingly coarse. Deposition of fines or erosion of coarse material may resume the erosion of fines from the bed.

In case of deposition the process is similar. Sediment is deposited in the bed surface layer that then passes its excess sediment to the lower bed layers (Figure 4.2, detail, upper right panel). If more fines are deposited than passed to the lower bed layers the bed surface layer becomes increasingly fine.

4.4.4 *Simulation of the Emergence of Non-erodible Roughness Elements*

Sediment sorting may lead to the emergence of non-erodible elements from the bed. Non-erodible roughness elements may shelter the erodible bed from wind erosion due to shear partitioning, resulting in a reduced sediment availability (Raupach et al., 1993). Therefore Equation 4.2 is implemented according to:

$$u_{*th,R} = u_{*th} \cdot \sqrt{\left(1 - m \cdot \sum_{k=k_0}^{n_k} w_k^{bed}\right)\left(1 + \frac{m\beta}{\sigma} \cdot \sum_{k=k_0}^{n_k} w_k^{bed}\right)} \tag{4.13}$$

in which σ is the ratio between the frontal area and the basal area of the roughness elements and β is the ratio between the drag coefficients of the roughness elements and the bed without roughness elements. m is a factor to account for the difference between the mean and maximum shear stress and is usually chosen 1.0 in wind tunnel experiments and may be lowered to 0.5 for field applications. The roughness density λ in the original equation of Raupach et al. (1993, Equation 4.2) is obtained from the mass fraction in the bed surface layer w_k^{bed} (Equation 4.11) according to:

$$\lambda = \frac{\sum_{k=k_0}^{n_k} w_k^{bed}}{\sigma} \tag{4.14}$$

in which k_0 is the index of the smallest non-erodible sediment fraction in current conditions and n_k is the total number of sediment fractions. It is assumed that the sediment fractions are ordered by increasing size. Whether a fraction is erodible depends on the sediment transport capacity.

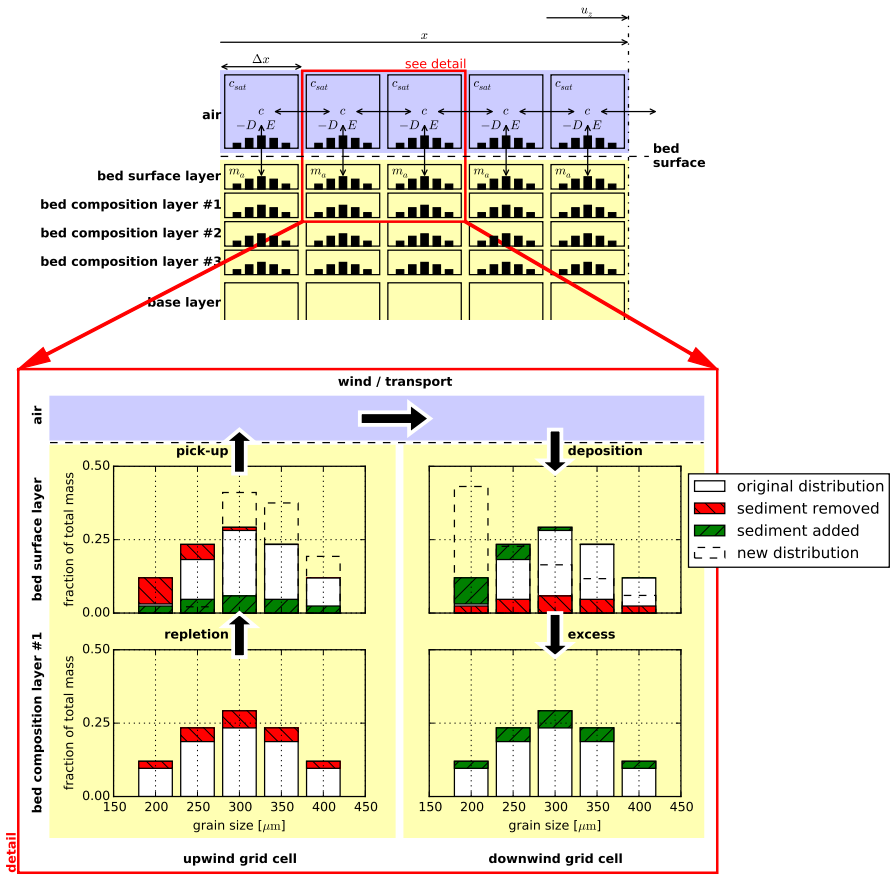

Figure 4.2: Schematic of bed composition discretisation and advection scheme. Horizontal exchange of sediment may occur solely through the air that interacts with the *bed surface layer*. The detail presents the simulation of sorting and beach armoring where the bed surface layer in the upwind grid cell becomes coarser due to non-uniform erosion over the sediment fractions, while the bed surface layer in the downwind grid cell becomes finer due to non-uniform deposition over the sediment fractions. Symbols refer to Equations 4.6 and 4.7.

4.4.5 *Simulation of the Hydraulic Mixing, Infiltration and Evaporation*

As sediment sorting due to aeolian processes can lead to armoring of a beach surface, mixing of the beach surface or erosion of course material may undo the effects of armoring. To ensure a proper balance between processes that limit and enhance sediment availability in the model both types of processes need to be sufficiently represented when simulating spatiotemporal varying bed surface properties and sediment availability.

A typical upwind boundary in coastal environments during onshore winds is the water line. For aeolian sediment transport the water line is a zero-transport boundary. In the presence of tides, the intertidal beach is flooded periodically. Hydraulic processes like wave breaking mix the bed surface layer of the intertidal beach, break the beach armoring and thereby influence the availability of sediment. Moreover, the hydraulic processes periodically wet the intertidal beach temporally increasing the shear velocity threshold. Infiltration and evaporation subsequently dry the beach.

In the model the mixing of sediment is simulated by averaging the sediment distribution over the depth of disturbance (Δz_d). The depth of disturbance is linearly related to the breaker height (e.g. King, 1951; Williams, 1971; Masselink et al., 2007). Masselink et al. (2007) proposes an empirical factor $f_{\Delta z_d}$ [-] that relates the depth of disturbance directly to the local breaker height according to:

$$\Delta z_d = f_{\Delta z_d} \cdot \min(H \quad ; \quad \gamma \cdot d) \tag{4.15}$$

in which the offshore wave height H [m] is taken as the local wave height maximized by a maximum wave height over depth ratio γ [-]. d [m] is the water depth that is provided to the model through an input time series of water levels. Typical values for $f_{\Delta z_d}$ are 0.05 to 0.4 and 0.5 for γ.

The drying of the beach is simulated by simplified functions for infiltration and evaporation. Infiltration is represented by an exponential decay function that is governed by a drying time scale T_{dry}. Evaporation is simulated using an adapted version of the Penman-Monteith equation (Shuttleworth, 1993) that is governed by meteorological time series of solar radiation, temperature and humidity.

4.5 RESULTS

The model is applied to a series of prototype cases to illustrate the processes described by the model, two wind tunnel experiments to illustrate the capabilities of the model to simulate spatiotemporal variations in bed surface properties and sediment availability and a sensitivity analysis.

4.5.1 *Prototype cases*

The four prototype cases P1 to P4 are intended to illustrate the capabilities of the presented model to simulate processes of sediment sorting (van der Wal, 2000; Arens et al., 2002) and beach armoring (van der Wal, 1998). The prototype cases are constructed using a 120 m schematized linear beach with a 1:20 slope, a wind velocity of 12 or 30 m/s, a drying time scale T_{dry} of 3 h, constant evaporation and a simula-

tion time of 30 days. The prototype cases are initialized with lognormally distributed sediment with $d_{50} = 335$ μm ($\Phi - \text{scale} = 1.6$, $\sigma_\Phi = 0.4$), which is representative for nourished poorly sorted beaches along the Dutch coast. Parameterizations for shells and shell fragments in Equation 4.13 are based on experiments described by McKenna Neuman et al. (2012) and chosen as $m = 0.5$, $\sigma = 4.2$ and $\beta = 130$. The four scenarios described by the prototype cases are:

P1 This scenario is used as reference for normalization and involves sand only and no tidal movement. The model is forced by a constant wind of 12 m/s. Sediment sorting occurs due to the presence of a wide range of sediment fractions. However, beach armoring does not occur due to the absence of shells, resulting in an almost constant sediment transport rate at the downwind end of the domain.

P2 This scenario involves 5% of shells and shell fragments ranging from 2 to 30 mm and no tidal movement. The model is forced by a constant wind of 12 m/s. The presence of shells means that beach armoring occurs that causes spatiotemporal variations in sediment availability and a decrease in sediment transport.

P3 This scenario involves 5% of shells and shell fragments and a sinusoidal tide with a 2 m tidal range and a tidal period of 12 h. The tide periodically floods a 40 m intertidal beach area. The model is forced by a constant wind of 12 m/s. The tidal movement causes mixing of the bed surface layer in the intertidal beach area reducing the effects of beach armoring.

P4 This scenario is equal to scenario P3, but the model is forced by a wind of 12 m/s that is increased twice to 30 m/s to simulate the effect of higher energy wind events that (partially) reset the composition of the bed surface layer and temporarily increase the sediment availability in the dry beach area.

Figure 4.3 presents the simulated aeolian sediment transport rates at the downwind end of the domain for cases P2 to P4 over the course of 30 days of simulation time. The results are normalized using the transport rate in case P1. The reference case P1 shows an almost constant transport rate over the entire course of the simulation. The presence of shells in case P2 results in a reduction of sediment availability. As a result, the transport rates in case P2 are lower compared to case P1. The transport rate decreases as more shells emerge from the bed and a beach armor layer develops. In case P2 there are no processes that break the armoring and the transport rates asymptotically reach zero. The beach armor layer develops in direction of the wind. Therefore, the relative contribution of the downwind part of the beach ($x \geqslant 40$) to the total sediment transport increases over time.

Case P3 includes tidal movement and hydraulic mixing. At the high water line the sediment transport is zero during high tide and maximized during low tide. Initially, transport is not saturated at the high water line and entrainment of sediment continues over the dry beach. As shells emerge from the bed, a beach armor layer develops that reduces sediment availability. The reduction of sediment availability progresses slower at the intertidal beach compared to the dry beach due to hydraulic mixing. After 8 days the sediment transport rates at the high water line start to exceed the sediment transport rates at the dune foot during low water. Sediment that is eroded from the intertidal beach during low water is partially trapped at the dry beach due to

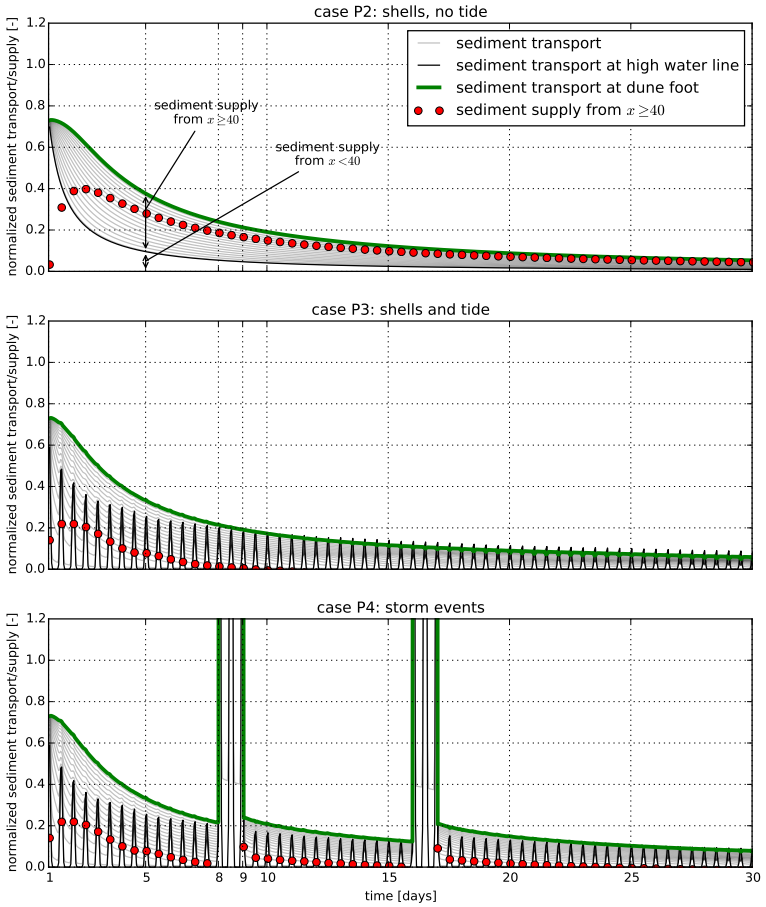

Figure 4.3: Sediment transport in time and over the model domain for three scenarios with constant wind. Each line depicts a different location along the beach, starting from x = 40 m, which coincides with the high water line in cases P3 and P4, and ends at the dune foot. Results are normalized using the transport rate in case P1 with almost constant transport (not shown). The difference between the sediment transport at dune foot (green) and the sediment transport at x = 40 m is visualized by the red dots and represents the sediment supply from the dry beach. In cases P3 and P4 the sediment transport at the high water line periodically exceeds the sediment transport at the dune foot, indicating local deposition of sediments originating from the intertidal beach.

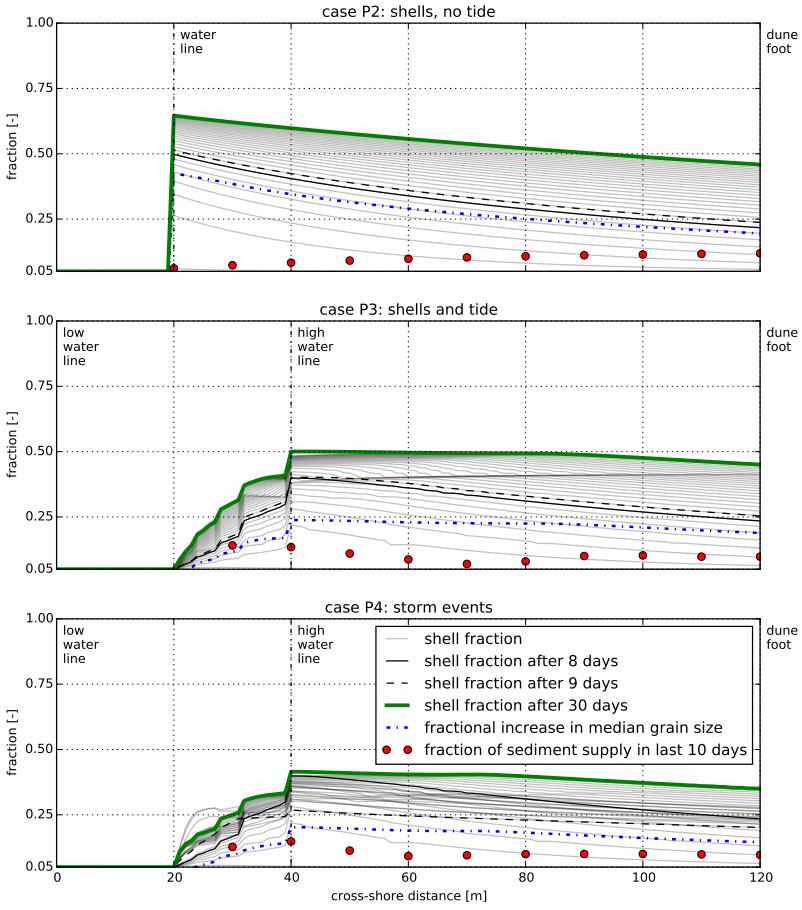

Figure 4.4: Distribution of the shell fraction over the model domain and in time. Sediment supply is inversely related to the degree of beach armoring, indicated by the shell fraction. Median grain size increases with the increase in shell fraction indicating erosion of predominantly fines. High-energy wind events in case P4 even mobilize shell fractions resulting in a decrease in beach armoring and an increase in sediment availability.

differences in roughness. During subsequent high water, when the sediment supply from the intertidal beach ceases, these deposits are again entrained and blown downwind. The net erosion from the dry beach ultimately approaches zero as armoring of the dry beach progresses. At this point all sediment deposited downwind originates directly from the intertidal beach. However, due to the spatial differences in roughness, sediment is temporally deposited at the dry beach and cause the sediment transport rates at the dune foot to be only weakly correlated with the tidal movement.

Case P4 shows a pattern similar to case P3, but after 8 and 16 days a relatively high-energy wind event passes for 24 hours. As a result, the transport rate spikes, but an elevated transport rate is also visible after the wind velocity drops. During the high-energy wind event even small shell fragments are mobilized. The beach armoring is therefore (partially) removed and more sediment is available for transportation afterwards. This leads to a prolonged peak in sediment transport and an increase of the relative contribution of the dry beach to the total sediment transport at the dune foot. After the beach armoring is re-established over time the transport rates approach the rates of case P3 again.

The differences in transport rate between the prototype cases are directly related to sediment availability, since the wind is constant in all cases but case P4. Figure 4.4 shows the fractions of shells and shell fragments in the bed surface layer for case P2 to P4. The shell fraction increases over time in all simulations. In case P2 the shell fraction peaks at the water line as the beach armor layer develops in downwind direction. Consequently, at the end of the simulation most sediment originates from the downwind end of the beach where the beach armoring is least developed. In case P3 and P4 hydraulic mixing causes the shell fraction in the intertidal beach to remain low resulting in a different distribution of shells compared to case P2 and hence a difference in sediment availability. Consequently, at the end of the simulation most sediment originates from the intertidal beach. In reality, the contribution of the intertidal beach to the total sediment transport is likely to be higher as more marine processes counteract the local development of a beach armor layer than currently simulated, like marine deposits and buoyancy of shells. In case P4 the drop in shell fraction from day 8 to day 9 is related to the first high-energy wind event. At the end of the simulation, the fraction of sediment that originates from the intertidal beach is relatively low compared to case P3. In all cases also the median grain size in the bed surface layer increases, indicating that predominantly fine sediment is eroded from the bed. The unbalanced sediment transport over the fractions cause sediment sorting in downwind direction.

The contribution to the instantaneous sediment transport of the specific processes described by the model can be distinguished in the prototype cases P1 to P4 because a constant wind velocity is imposed. If a more realistic variable wind velocity time series is used, the contributions of the specific processes are obscured by the wind-related variance. To show that the simulation of spatiotemporal bed surface properties and sediment are also important in variable wind conditions, prototype cases P1 to P3 are repeated using an synthetic variable wind time series (P1b to P3b). The time series is generated using a Markov Chain Monte Carlo (MCMC) simulation following a Weibull distribution with a mean wind velocity of 12 m/s.

Figure 4.5 shows the sediment transport rate in case P3b normalized by the sediment transport rate in case P1b depending on the hourly averaged wind velocity. To

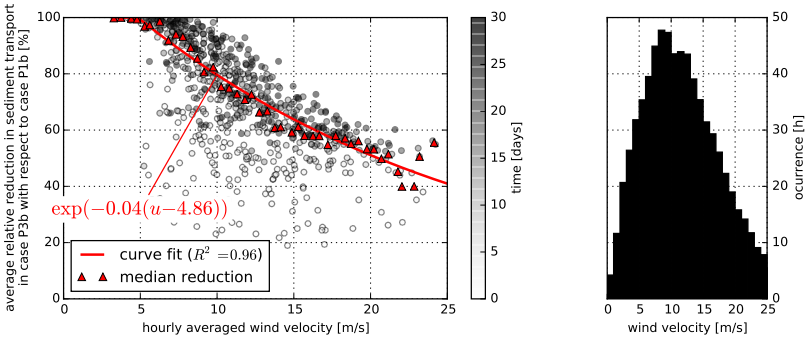

Figure 4.5: Average reduction in sediment transport in prototype case P3b compared to case P1b depending on the hourly averaged wind velocity (left panel). The results are obtained using an synthetic variable wind time series following a Weibull distribution with a mean wind velocity of 12 m/s (right panel). The sediment transport reduction (scatter) is binned according to the wind velocity using 0.5 m/s bins. The median reduction per bin (triangles) is used to fit an exponential curve (line). The reduction tends to increase during the simulation (scatter colors).

remove the influence of the wind variability, the normalized sediment transport time series obtained from the simulations are binned according to the hourly averaged wind velocity in 0.5 m/s bins. The median transport rate in each bin is subsequently determined to obtain a relation between instantaneous normalized sediment transport and wind velocity. The reduction is close to 100% up to wind velocities of 5 m/s and subsequently decreases according to an exponential function. The median reduction for 12 m/s wind velocity is 74%, which is less than the maximum reduction of 95.0% with a constant 12 m/s wind velocity in case P3. The reduction tends to increase during the simulation as beach armoring progresses.

4.5.2 *Wind tunnel experiments*

To illustrate the applicability of the model approach, two unrelated wind tunnel experiments obtained from literature are simulated that involve either temporal (Nickling and McKenna Neuman, 1995) or spatial (Dong et al., 2004b) variations in bed surface properties as discussed in section 4.2.

Nickling and McKenna Neuman (1995) describe an experiment in a wind tunnel with a 4.5 m working section in which a grid of 18 mm marbles was buried in sandy material with $d_{50} = 270$ µm. During the experiment with constant wind of 8 m/s, measured at 25 cm above the bed, the sand is winnowed from in between the marbles resulting in the emergence of the marbles over time. The emergence of the marbles cause the bed to become armored. The effect of armoring of a marble extends beyond the marble dimensions due to shadowing effects in the lee of the marble described by Equation 4.13. All parameter values, including z', are obtained from Nickling and

McKenna Neuman (1995) and hence no further calibration of parameters is performed for this simulation.

Figure 4.6 shows the modeled normalized sediment transport rate in comparison with the measurements described in Nickling and McKenna Neuman (1995). Where the measurements start with a relatively constant transport and even a slight increase in transport, the model predicts an immediate decrease in transport. The marbles are modeled as a large sediment fraction for which its presence in a bed composition layer is described by a mass fraction rather than a location. Therefore, it is possible to define the marble density, but not the exact marble locations. Consequently, from the start of the simulation marbles start to emerge from the bed resulting in an immediate decrease in sediment transport. In contrast, in the wind tunnel the marbles are covered with a thin layer of sand that was removed first before the marbles start to emerge. The initial emergence of the marbles coincided with a slight increase in sediment transport. Nickling and McKenna Neuman (1995) attributes this rise to a pronounced change in boundary conditions and turbulence. Since these small scale variations in the wind shear are not represented in the model the rise in transport is not visible in the model results. However, the decrease in sediment transport due to the emergence of the marbles for the three different grid spacings described in Nickling and McKenna Neuman (1995), is qualitatively represented by the model.

Dong et al. (2004b) describe an experiment in a wind tunnel with a 21 m working section in which a patch of gravel with diameter 10 – 40 mm was positioned downwind of a sandy bed with $d_{50} = 180$ μm. The length of the gravel patch was varied between the experiments from 0.5 – 12 m and the wind velocity from 8 – 22 m/s, measured at 60 cm above the bed. The free-flow wind velocities are converted to shear velocities assuming $z' = 6$ mm. The gravel patch traps saltating grains. In the model the entrapment of grains is simulated as an exchange of momentum between the sandy fractions and the immobile gravel fraction. This exchange is governed by the bed interaction parameter, which is calibrated for this simulation and found to be 0.05.

Figure 4.7 shows the modeled sediment transport rate in comparison with the measurements described in Dong et al. (2004b). The increase in sediment transport with increasing wind velocity is well represented by the model given the uniform RMSE among the different wind velocities. The decrease in sediment transport rate with increasing gravel patch length is represented by the model with a relative RMSE of less than 10% for all except the lowest and highest wind velocities. Significant surpassing of sediment over the sediment trap during the measurements with 22 m/s wind velocity is reported by Dong et al. (2004b), which explains the consistent overprediction of the sediment fluxes by the model. The discrepancy between the model and the measurements for the 8 and 10 m/s wind velocities is less consistent and is expected to be a result of a low signal-to-noise ratio related to the small sediment fluxes. Also for short gravel patch lengths the model deviates from the measurements. The relatively high variability over the 0.5 to 2 m gravel patch lengths is attributed to a change in transport characteristics (Dong et al., 2004b) due to fully elastic collisions between the sand grains and the gravel. A bed interaction parameter that is not constant is needed to capture this behavior in the model.

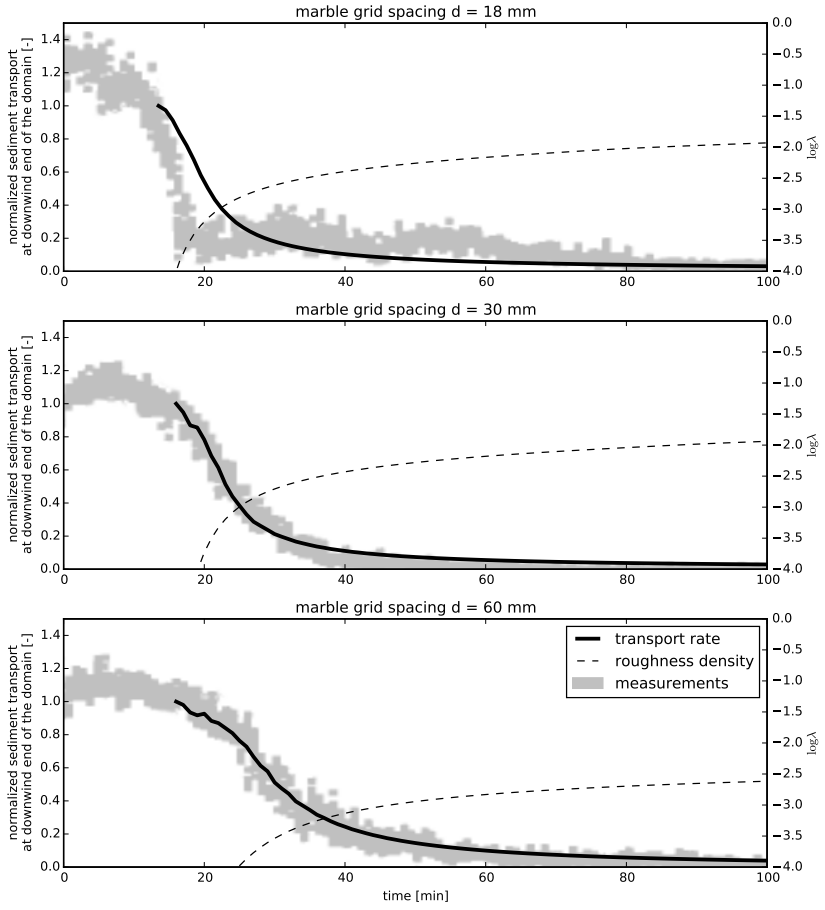

Figure 4.6: Comparison between modeled and measured normalized sediment transport rates from wind tunnel experiments described in Nickling and McKenna Neuman (1995). The dashed line depicts the emergence of marbles in terms of increasing roughness density. The visualization of the measurement results is copied from Figure 4 in the original publication without digitization.

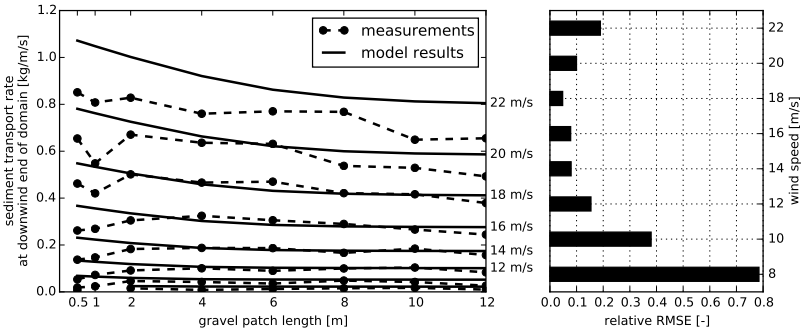

Figure 4.7: Comparison between model results and measurements from wind tunnel experiments described in Dong et al. (2004b) (left panel) and RMS errors relative to the mean measured transport rate (right panel). The measured transport rates with a wind velocity of 22 m/s are underestimated due to surpassing of sediment over the sediment trap (Dong et al., 2004b).

4.5.3 *Sensitivity*

The sensitivity of the model to four newly introduced parameters and the wind velocity is determined to obtain insight in the importance of these parameters to the model results. The newly introduced parameters are the bed interaction parameter, depth of disturbance factor, the drying time scale and the grain size distribution standard deviation. Case P3 as presented in section 4.5.1 is used as starting point for the sensitivity analysis. Figure 4.8 shows the change in normalized total sediment transport given variations of each of the four model parameters and the wind velocity.

The bed interaction parameter, the depth of disturbance factor and the drying time scale affect the source area of aeolian sediment (Figure 4.8a, b and c). In absence of bed interaction all sediment entrained in the intertidal beach area is being transported to the downwind end of the domain unhindered. In contrast, in the presence of bed interaction sediment from the intertidal beach area may be trapped in the beach armor layer that is being developed in the dry beach area during the simulation. Consequently, the total sediment transport reduces with increasing bed interaction. The bed interaction parameter parameterizes the exchange between sediment fractions, which is an aspect of saltation that is still poorly understood. In particular situations with a large spatial variability in bed surface properties the bed interaction parameter is expected to show a more significant sensitivity (e.g. Dong et al., 2004b). Therefore calibration of the bed interaction parameter is necessary in such situations.

The depth of disturbance factor shows no significant sensitivity as aeolian sediment supply from the intertidal beach is concentrated close to the water line where wave heights are negligible. Lower parts of the intertidal beach are continuously too moist for sediment to be entrained. The sensitivity to the depth of disturbance factor increases with decreasing drying time scale, but typically only for values smaller than 0.5 m. The sensitivity to the drying time scale shows that for time scales larger than several hours the intertidal beach is continuously too moist for sediment to be en-

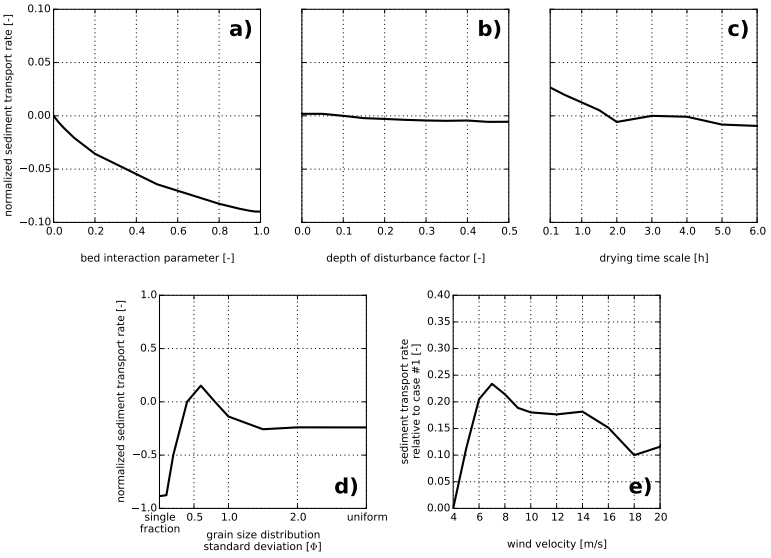

Figure 4.8: Sensitivity of the total normalized sediment transport with respect to case P3 for four newly introduced parameters and the wind velocity. The sensitivity of the wind velocity is expressed with respect to the transport rate in case P1.

trained. For small drying time scales the intertidal beach supplies aeolian sediment that contains relatively many fines, resulting in a slight increase in total sediment transport.

From the sensitivity of the grain size distribution width, represented by the grain size distribution standard deviation and strictly speaking not a model parameter, it can be concluded that the introduction of multiple sediment fractions has a significant impact on the sediment transport rate (Figure 4.8d). However, for poorly sorted sediments the sensitivity of the model to the distribution width is limited. Beyond a standard deviation of $\sigma_\Phi = 1.5$ the development of the sediment rate is similar to the transport rate with a uniform distribution.

The rate of armoring depends on the presence of non-erodible sediment fractions. Whether a sediment fraction is erodible depends on the wind transport capacity. Therefore the rate of armoring and consequently the instantaneous sediment availability depends on the wind velocity. Figure 4.8e depicts the sediment transport rate in case P3 with respect to the almost constant transport rate in case P1 for different wind velocities. For low wind velocities all shell fractions can contribute to the establishment of a beach armor layer, but the beach armor layer develops slowly as the winnowing of fines is dependent on the entrainment rate. For high wind velocities even shell fragments may be mobilized, but the beach armor layer consisting of larger shells is developed quickly. Consequently, the reduction of sediment transport is present over all wind velocities and 83% on average.

4.6 DISCUSSION

Process-based simulation of bed surface properties and sediment supply provides an alternative for complex spatiotemporal parameterizations. Nevertheless, process-based simulation itself requires parameterization, calibration and validation. These parameterizations are generally less complex as they describe static properties rather than spatiotemporal varying processes.

4.6.1 *Parameterization*

Compared to existing models for availability-limited aeolian sediment transport the need for complex parameterization has been reduced in the presented model. The adoption of the advection model of de Vries et al. (2014b) makes parameterization of spatiotemporal variations in the shear velocity threshold, like attempted by Nickling and McKenna Neuman (1995), Dong et al. (2004b) and others, unnecessary. In addition, process-based simulation of bed surface properties makes parameterization of the inherently time-varying sediment availability m_a unnecessary. Existing parameterizations for the shear velocity threshold under influence of moisture, vegetation, sediment sorting and other bed surface properties are still valid for the instantaneous shear velocity threshold.

Despite the efforts to minimize complex parameterizations that are difficult to generalize, the model also introduces new parameterizations that are specifically related to the process-based simulation of sediment availability, i.e. the bed interaction parameter, depth of disturbance and soil drying time scale. The depth of disturbance and soil drying time scale could easily be replaced by process-based simulation as

there is thorough knowledge on near-shore morphodynamics and beach hydrology. Moreover, the presented model framework allows for spatiotemporal variations of parameters that are known not to be constant (e.g. z'). However, these considerations are outside the scope of this paper and will be part of future research.

4.6.2 *Calibration*

The calibration of the parameters involved in process-based simulation of sediment availability is a relatively new field of research. In this paper a pragmatic approach to calibration of these parameters is adopted, but there are various opportunities for improvement. For example, the depth of disturbance is used to approximate the mixing of the intertidal beach surface by waves. Masselink et al. (2007) shows how the depth of disturbance can be determined based on a linear relation with the local wave height. The mixing of the intertidal beach surface is particularly important as it breaks beach armoring. The depth of disturbance does not provide any information about how the bed is disturbed, just over which depth. Moreover, aspects like marine deposits and shell buoyancy also affect the sediment availability in the intertidal beach area. Gallagher et al. (2011) presented detailed measurements of spatiotemporal variations in the bed surface grain size at Truc Vert, France. The intertidal beach appears to be consistently finer than the upper beach. The measurements are obtained using macrophotography (Buscombe et al., 2010) ensuring that the measurements solely involve the beach surface. These type of measurements may provide a much more detailed calibration of the hydraulic mixing simulated in the model, although it might be questioned if such detailed hydraulic calibration is still within the scope of an aeolian sediment transport model. Alternatively, the calibration of the hydraulic mixing could be left to dedicated near-shore models (e.g. XBeach; Roelvink et al., 2009; Reniers et al., 2013) and online model coupling could be used to incorporate detailed near-shore hydro- and morphodynamics in the proposed aeolian modeling framework.

Similarly, an exponential decay function with a constant drying time scale is currently used to approximate the influence of the hydrological process of infiltration. The exponential decay is a simplified approach that was adopted after it appeared to be a reasonable approximation of numerical model results obtained with the HYDRUS model (Šimůnek et al., 1998) that simulates the soil moisture contents in the unsaturated zone following van Genuchten (1978). Detailed measurements for calibration of the instantaneous soil moisture can be obtained relatively easy using either in-situ or remote infra-red or microwave measurements (e.g. Edwards et al., 2013; Hoonhout et al., 2014a). Again, it might be questioned if the amount of detail involved in using these kind of data for estimates of the bed surface moisture is still within the scope of an aeolian sediment transport model.

In contrast to the depth of disturbance and the drying rate, the bed interaction parameter has little relation with existing literature. In essence, the bed interaction parameter describes the exchange of momentum between grain size fractions along the fetch distance. Specifically it describes whether impacting grains eject other grains from the bed or that they are rebounded due to fully elastic collisions with large, non-erodible elements. A low value for the bed interaction parameter would indicate a large number of rebounding grains, while a high value would indicate a low num-

ber of rebounding grains. Typically, the number of rebounded grains increases with an increasing number of non-erodible, large elements in the bed. Consequently, the bed interaction parameter is not uniform over the fractions. Moreover, due to beach armoring the bed interaction is neither constant over time nor in space. In this paper the bed interaction parameter is pragmatically assumed to be uniform and constant since no basis for differentiation of the parameter is currently available. Thorough calibration of the bed interaction parameter would require detailed, spatiotemporal measurements of grain size distributions in the bed and the saltation cascade. It would require a series of sediment traps along the fetch that are regularly emptied and sieved as to determine the change of the grain size distribution in the saltation cascade in space and over time. Concurrently the grain size distribution at the bed surface over the entire fetch needs to be monitored without disturbing the bed significantly. In a laboratory environment the change in grain size distribution could be monitored using sediment that is colored per fraction. Visual observation of the change in coloring then provides insight in the change in grain size distribution. However, the experiment should be performed at such scale that the trapping of sediment by upwind traps does not significantly influence the saltation cascade downwind over the period that the armor layer develops.

4.6.3 *Validation*

Validation of the proposed model is ongoing. Initially, validation will be focused on gross sediment transport rates in availability-limited systems. Few holistic measurements are available that monitor both the spatiotemporal variations in the sediment transport rate and the availability-limiting factors like moisture content and beach armoring concurrently (e.g. Delgado-Fernandez et al., 2012; Hoonhout et al., 2013). Sites with detailed and frequent topographic measurements and hydrodynamic boundary conditions available can be found worldwide. These sites would be a good starting point for assessing the performance of the model compared to existing models. Using simplified, but generic descriptions of the hydraulic mixing and drying rate the model should already provide time series of aeolian sediment transport that adhere much better to the true nature of aeolian sediment transport events than existing models. Delgado-Fernandez and Davidson-Arnott (2011) and de Vries et al. (2014a) already indicated that the true nature of these events is not solely related to wind velocity and direction, but also to surges, seasons, spring/neap cycles, rain showers and other events that influence sediment availability. The variations in aeolian sediment transport due to these event-driven changes in sediment availability are not well captured by models that rely solely on the wind transport capacity. The model has added value if it improves the prediction of transport rates under such circumstances.

4.7 CONCLUSIONS

The AeoLiS model presented in this paper is the first aeolian sediment transport model that simulates spatiotemporal variations in bed surface properties and sediment availability. Simulation of sediment availability is necessary as sediment availability cannot be determined a-priori due to its recurrence relation with sediment transport. The presented model approach is a generalization of existing modeling

concepts for aeolian sediment transport that include the influence of bed surface properties and limitations in sediment availability, like the shear velocity threshold and critical fetch, and is compatible with these concepts. The model uses an advection scheme following de Vries et al. (2014b) and a bed composition module that discretizes the bed in horizontal grid cells and vertical bed layers to account for spatial variations in bed surface properties. Temporal variations in sediment availability are not parameterized, but simulated using the bed composition module. The simulation of sediment availability reduces the need for complex spatiotemporal parameterizations and consequently calibration. In this paper the influence of sediment sorting and beach armoring and the reversed process of hydraulic mixing on aeolian sediment transport are illustrated using four prototype cases. The model can reproduce patterns in aeolian sediment availability and transport as observed in wind tunnel experiments that involve spatiotemporal variations in bed surface properties (Nickling and McKenna Neuman, 1995; Dong et al., 2004b). Further, the model provides a generic framework to incorporate additional spatiotemporal varying processes that either influence sediment availability or the wind transport capacity with a minimum of parameterization. The framework allows relatively straightforward implementation of the effects of infiltration, evaporation, vegetation, buildings, and morphological feedback with the wind.

From this paper the following conclusions can be drawn:

1. A model for aeolian sediment transport was presented that simulates the processes of sediment sorting and beach armoring, the reversed process of hydraulic mixing, interaction between sediment fractions in the air with sediment fractions in the bed and thereby the influence of spatiotemporal variations in sediment availability;

2. The model can be seen as a generalization of existing approaches to incorporate limitations in sediment availability and the wind transport capacity in aeolian transport estimates and is compatible with approaches based on either shear velocity thresholds or critical fetch;

3. The process of beach armoring can be a governing factor in aeolian sediment transport modeling and may reduce the estimated transport rates significantly and up to 95.0% in the presented prototype cases;

4. The model can reproduce typical patterns in aeolian sediment transport with spatiotemporal variations in sediment availability obtained from measurements from the unrelated wind tunnel experiments described in Nickling and McKenna Neuman (1995) and Dong et al. (2004b), with a minimum parameterization and calibration.

5

SAND MOTOR HINDCAST

5.1 INTRODUCTION

In availability-limited coastal systems, the aeolian sediment transport rate is governed by the sediment availability rather than the wind transport capacity. Aeolian sediment transport models typically incorporate the sediment availability through the shear velocity threshold. However, the determination of appropriate threshold values in practice appears to be challenging as the shear velocity threshold tends to vary both spatially and temporally (Barchyn et al., 2014b). For example, soil moisture in the intertidal beach area fluctuates with the tidal phase and causes a local modulation of the shear velocity threshold. Moreover, a recurrence relation between sediment availability, and thus the shear velocity threshold, and sediment transport exists that complicates the a-priori determination of an appropriate threshold value. Consequently, aeolian sediment transport models tend to perform poorly in availability-limited systems.

Sherman et al. (1998) and Sherman and Li (2012) summarized the performance of eight aeolian sediment transport models compared to field measurements on a sandy beach. Although it is unknown whether this coastal system was availability-limited, all models systematically overpredicted the measured aeolian sediment transport rates. This finding is in correspondence with an abundance of coastal field studies in which aeolian sediment transport rates are overestimated by numerical models (e.g. Jackson and Cooper, 1999; Lynch et al., 2008; Davidson-Arnott and Bauer, 2009; Aagaard, 2014).

In an attempt to explain the poor performance of aeolian sediment transport models in coastal environments, many authors emphasized the importance of sediment availability and bed surface properties. Typical bed surface properties that are found along the coast and known to affect sediment availability are high moisture contents (e.g. Wiggs et al., 2004; Davidson-Arnott et al., 2008; Darke and McKenna Neuman, 2008; McKenna Neuman and Sanderson, 2008; Udo et al., 2008; Bauer et al., 2009; Edwards and Namikas, 2009; Namikas et al., 2010; Scheidt et al., 2010), salt crusts (e.g. Nickling and Ecclestone, 1981), vegetation (e.g. Arens, 1996; Lancaster and Baas, 1998; Okin, 2008; Li et al., 2013; Dupont et al., 2014), shell pavements (e.g. van der Wal, 1998; McKenna Neuman et al., 2012) and sorted and armored beach surfaces (e.g. Gillette and Stockton, 1989; Gillies et al., 2006; Tan et al., 2013; Cheng et al., 2015). The influence of these bed surface properties on aeolian sediment availability and transport has been investigated and typically resulted in relations between bed surface properties

and the shear velocity threshold (e.g. Howard, 1977; Dyer, 1986; Belly, 1964; Johnson, 1965; Hotta et al., 1984; Nickling and Ecclestone, 1981; Arens, 1996; King et al., 2005).

Modeling rather than parameterization of spatiotemporal variations in aeolian sediment availability can improve coastal aeolian sediment transport estimates. As tides only affect the intertidal beach area, lag deposits and salt crusts typically emerge from the dry beach area, and vegetation is often restricted to the dune area, sediment availability varies spatially. In addition, temporal variations in sediment availability are induced by tidal spring/neap cycles, rain showers, storm surges, seasonal variations in vegetation and progressive armoring of the beach. Due to self-grading of the sediment, progressive beach armoring creates a recurrence relation between sediment availability and transport that challenges the a-priori determination of the spatiotemporal variations in sediment availability. Process-based modeling of the instantaneous shear velocity threshold field can address these challenges and improve coastal aeolian sediment transport estimates.

This paper presents the first application of a two-dimensional (2DH) aeolian sediment availability and transport model (Hoonhout and de Vries, 2016b) to hindcast the development of the sub-aerial topography of an availability-limited coastal system. The model is unique in that it describes both spatial and temporal variations in aeolian sediment availability induced by the combined influence of sediment sorting, beach armoring and soil moisture content. The influence of spatiotemporal variations in aeolian sediment availability and the model performance are illustrated by a comparison between model results and a large scale sediment budgets analysis that identifies and quantifies the main sources and sinks for aeolian sediment in the coastal system (Hoonhout and de Vries, 2017a).

5.2 FIELD SITE

The Sand Motor (or Sand Engine) is an artificial 21 Mm^3 sandy peninsula protruding into the North Sea off the Delfland coast in The Netherlands (Figure 5.1, Stive et al., 2013). The Sand Motor was constructed in 2011 and its bulged shoreline initially extended about 1 km seaward and stretched over approximately 2 km along the original coastline. The original coast was characterized by an alongshore uniform profile with a vegetated dune with an average height of 13 m and a linear beach with a 1:40 slope. The dune foot is located at a height of approximately 5 m+MSL.

Due to natural sediment dynamics the Sand Motor distributes about 1 Mm^3 of sand per year to the adjacent coasts (Figure 5.1). The majority of this sand volume is transported by tides and waves. However, the Sand Motor is constructed up to 5 m+MSL and locally up to 7 m+MSL, which is in either case well above the maximum surge level of 3 m+MSL (Figure 5.2c). Therefore, the majority of the Sand Motor area is uniquely shaped by wind.

The Sand Motor comprises both a dune lake and a lagoon that act as large traps for aeolian sediment (Figure 5.1). The lagoon is affected by tidal forcing, although the tidal amplitude quickly diminished over time as the entry channel elongated. The tidal range of about 2 m that is present at the Sand Motor periphery (Figure 5.2c), is nowadays damped to less than 20 cm inside the lagoon (de Vries et al., 2015). Consequently, the tidal currents at the closed end of the lagoon, where most aeolian sediment is trapped, are negligible.

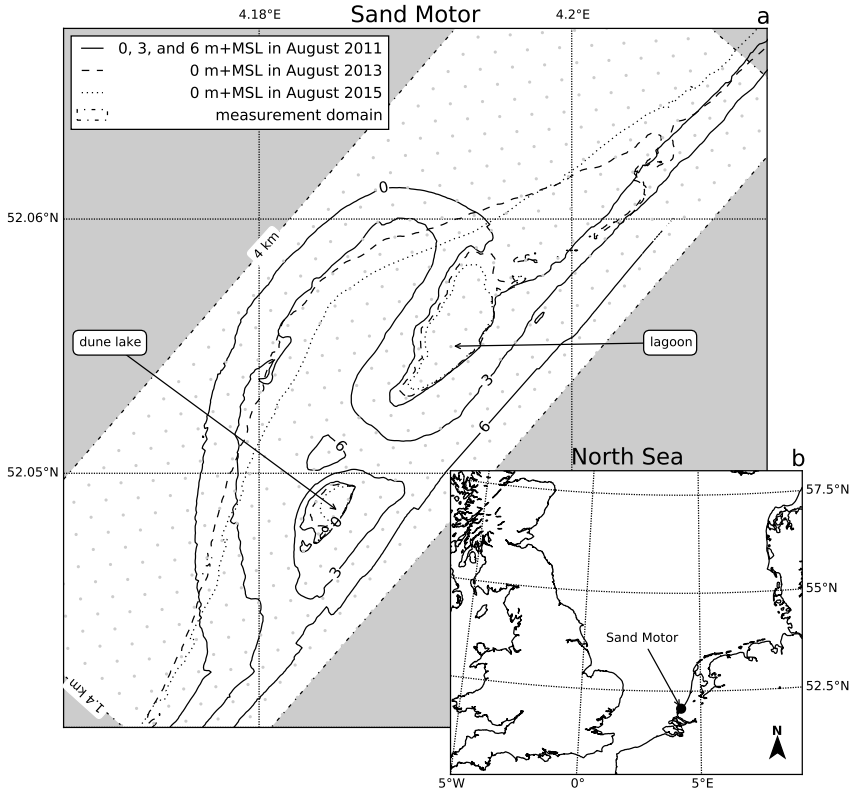

Figure 5.1: Location, orientation, appearance and evolution of the Sand Motor between construction in 2011 and 2015. The box indicates the measurement domain used in the remainder of this paper. A 100 x 100 m grid aligned with the measurement domain is plotted in gray as reference.

The dominant wind direction at the Sand Motor is south to southwest (Figure 5.2a). However, during storm conditions the wind direction tends to be southwest to northwest. During extreme storm conditions the wind direction tends to be northwest. Northwesterly storms are typically accompanied by significant surges as the fetch is virtually unbounded to the northwest, while surges from the southwest are limited due to the presence of the narrowing of the North Sea at the Strait of Dover (Figure 5.1, inset).

5.3 MODEL APPROACH

A two-dimensional (2DH) model of the Sand Motor that includes limitations in sediment availability is constructed and calibrated based on four years of field measurements on wind, tides, waves and topography. The calibrated model is used to investigate the influence of spatiotemporal variations in aeolian sediment availability on sediment accumulation in the Sand Motor domain.

To test that the Sand Motor mega nourishment is indeed an availability-limited coastal system, the measured long-term sediment accumulation volumes (Hoonhout and de Vries, 2017a) are first compared to a reference model that assumes no limitations in sediment availability exist.

5.3.1 *Reference model*

A selection of equilibrium sediment transport formulations is used as reference model. An equilibrium sediment transport formulation describes the wind transport capacity in given conditions. In conjunction with a shear velocity threshold based on only a constant uniform median grain size, an estimate of the potential aeolian sediment accumulation in absence of availability-limitations can be obtained. The potential aeolian sediment accumulation or cumulative wind transport capacity Q [m^3] in the Sand Motor domain is estimated based on hourly averaged time series of the wind speed u_z [m/s] and direction θ_u [°] obtained from the KNMI meteorological station in Hoek van Holland following:

$$Q = \sum q \cdot \frac{\Delta t \cdot \Delta y}{(1-p) \cdot \rho_p} \cdot f_{\theta_u} \tag{5.1}$$

where the temporal resolution Δt = 1 h, the alongshore span of the domain Δy = 4 km, the porosity p = 0.4, the particle density ρ_p = 2650 kg/m^3, the sediment transport rate q is given by the equilibrium sediment transport formulation (Table 5.1) and f_{θ_u} is a factor to account for the wind direction. The wind direction can be accounted for by only including the onshore wind component with respect to the original coastline orientation. However, given the typical Sand Motor geometry (Figure 5.1), sediment is likely to be trapped in the dune lake and lagoon even with alongshore wind. Therefore it can be assumed that the onshore wind component will provide a lower limit of the cumulative wind transport capacity. Similarly, an upper limit can be obtained by assuming that all onshore wind directions contribute equally to the cumulative wind transport capacity. For the upper limit the factor f_{θ_u} is defined as:

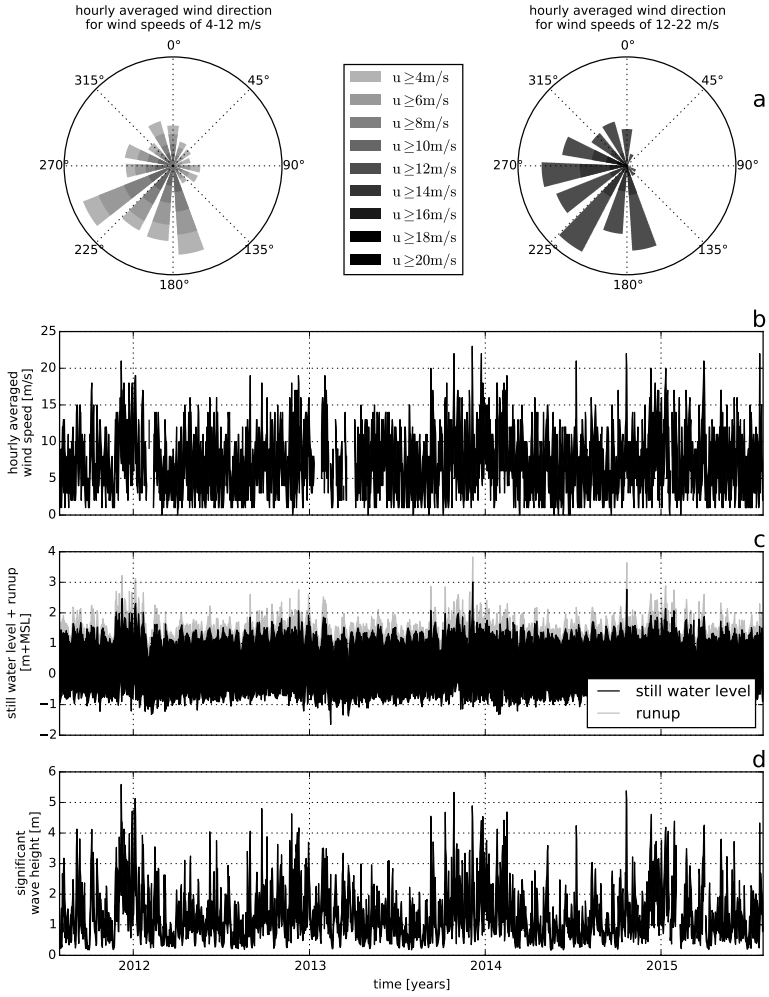

Figure 5.2: Wind and hydrodynamic time series from 2011 to 2015. Hourly averaged wind speeds and directions are obtained from the KNMI meteorological station in Hoek van Holland (upper panels). Offshore still water levels, wave heights and wave periods are obtained from the Europlatform (lower panels). Runup levels are estimated following Stockdon et al. (2006).

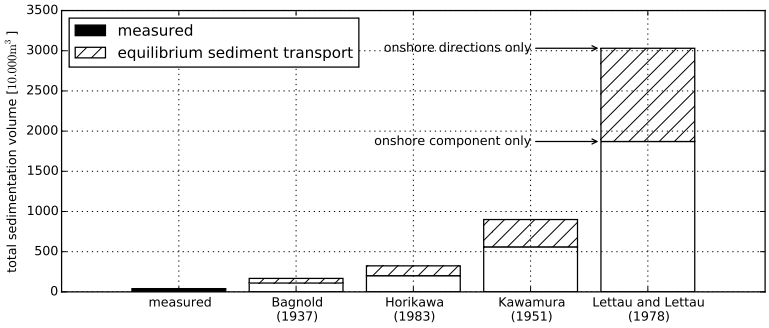

Figure 5.3: Comparison of the cumulative wind transport capacity according to a selection of equilibrium sediment transport formulations and measured total sedimentation in the Sand Motor domain. The equilibrium sediment transport is based on an hourly averaged wind speed and direction time series from September 1, 2011 until September 1, 2015. Offshore wind directions are discarded. For the upper boundary of each estimate all wind directions are weighted equally. For the lower boundary of each estimate the wind directions are weighted according to the magnitude of the onshore component.

$$f_{\theta_u} = \begin{cases} 1 & \text{if} \quad \cos(312^\circ - \theta_u) \geqslant 0 \\ 0 & \text{if} \quad \cos(312^\circ - \theta_u) < 0 \end{cases} \tag{5.2}$$

while for the lower limit the factor f_{θ_u} is defined as:

$$f_{\theta_u} = \max(0 \quad ; \quad \cos(312^\circ - \theta_u)) \tag{5.3}$$

where 312° accounts for orientation of the original coastline. Figure 5.3 presents an overview of the cumulative wind transport capacity in the Sand Motor domain over the period between September 1, 2011 and September 1, 2015 according to a selection of equilibrium sediment transport formulations and in comparison with the measured accumulation volumes. The estimates of the wind transport capacity show a large variation between formulations that are mainly due to the incorporation of the shear velocity threshold. However, all formulations overestimate the measured sediment accumulation in the Sand Motor domain with at least a factor $3-4$. The large variation and consistent overestimation is in accordance with the review of aeolian sediment transport models presented by Sherman and Li (2012). The consistent overestimation of the measured sedimentation volumes in the Sand Motor domain suggest that the Sand Motor is indeed an availability-limited coastal system.

5.3.2 *Schematization*

A two-dimensional (2DH) aeolian sediment availability and transport model for the Sand Motor mega nourishment is constructed for the four years between September

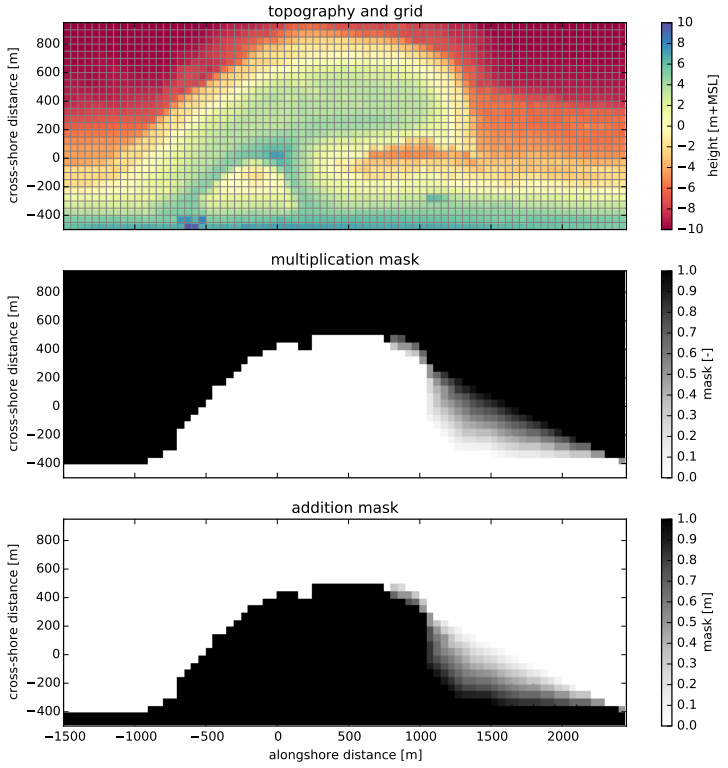

Figure 5.4: Model grid and topography based on the topographic survey of August 3, 2011 (upper panel) and hydrodynamic mask used to limit tidal and wave motions in the dune lake and lagoon (middle and lower panels). Water levels and wave heights are uniformly imposed to the model and multiplied by the multiplication mask and subsequently increased with the addition mask.

Table 5.1: Equilibrium sediment transport formulations, coefficient values* and the ratio between measurements and model results.

Reference	Equation	C	Ratio
Bagnold (1937b)	$q = C\frac{\rho_a}{g}\sqrt{\frac{d_n}{D_n}}\,(u_* - u_{*th})^3$	1.8	3 – 4
Horikawa et al. (1983)	$q = C\frac{\rho_a}{g}\,(u_* + u_{*th})^2\,(u_* - u_{*th})$	1.0	5 – 8
Kawamura (1951)		2.78	14 – 22
Lettau and Lettau (1978)	$q = C\frac{\rho_a}{g}\sqrt{\frac{d_n}{D_n}}\,(u_* - u_{*th})\,u_*^2$	6.7	46 – 75

* Other values are the shear velocity $u_* = \alpha \cdot u_z$ m/s, the shear velocity threshold $u_{*th} = \alpha \cdot 3.87$ m/s, the conversion factor from free-flow wind velocity to shear velocity $\alpha = 0.058$, the air density ρ_a = 1.25 kg/m^3, the particle density ρ_p = 2650.0 kg/m^3, the gravitational constant g = 9.81 m/s^2, the nominal grain size d_n = 335 μm, a reference grain size D_n = 250 μm and the height above the bed of the wind measurement z = 10 m.

1, 2011 and September 1, 2015, which is shortly after the nourishment was placed. The model's topography and grid are based on the measured topographies of August 3, 2011 and later. The topographies are rotated 48 ° and interpolated to a 50 x 50 m grid spanning 1.5 km cross-shore and 4 km alongshore with respect to the original coastline, not including the dunes (Figure 5.4, upper panel).

Four years of hourly wind speed and direction data measured at 10 m above the bed is obtained from the KNMI meteorological station at Hoek van Holland (Figure 5.2a,b). Hourly offshore water levels and wave heights are obtained from the Europlatform for the same period (Figure 5.2c,d).

An average lognormal grain size distribution with a median diameter $d_{50} = 335$ μm is used as measured at the Sand Motor field site. The sand fractions cover a range from 0.1 to 2 mm. The amount of shells and other roughness elements in the originally nourished sand is estimated to be 5%. The estimate is based on three sediment samples obtained from the field site 0.5 m below the bed surface. Additional fractions ranging from 2 to 32 mm are added according to a lognormal distribution to account for the presence of roughness elements in the bed. The grain size distribution is used to populate the initial bed that consists of 10 bed composition layers with a thickness of 1 cm each.

The hindcast aims at the large scale and long term sedimentation volumes as presented by Hoonhout and de Vries (2017a). Therefore an efficient, but diffusive, implicit Euler Backward scheme with a timestep of 1 h is used that does not resolve high frequency variations in wind or sediment transport. Consequently, the model produces smooth solutions that describe hourly steady states based on the instantaneous average wind speed and sediment availability.

Bagnold (1937b) is selected as equilibrium sediment transport formulation as it is derived separately for different grain sizes and therefore suitable for multi-fraction aeolian sediment transport. Alternative formulations (Table 5.1) are derived for wider grain size distributions that do not necessarily result in a monotonic relation between the grain size and the sediment transport rate (e.g. Kawamura, 1951; Horikawa et al., 1983). Such non-monotonic relation is unrealistic in a multi-fraction context as it would result in a preference to transport both fine sediment and large elements that are considered non-erodible. Moreover, the formulation of Bagnold (1937b) overesti-

mates the measured aeolian sediment transport rates in the Sand Motor domain less compared to alternative formulations (Table 5.1, rightmost column).

Water levels and wave heights are initially uniformly imposed to the model. Consequently, the tidal range, mean water level and wave heights that are present at the Sand Motor periphery are also present in the dune lake and lagoon. In reality the tidal range and wave heights in the dune lake and lagoon are much lower, while the mean water level in the dune lake and lagoon is elevated compared to mean sea level (de Vries et al., 2015). To account for these spatial differences in hydrodynamics a hydrodynamic mask is applied (Figure 5.4, middle and lower panel; Appendix B.3.4)

Subtidal changes in topography are not simulated by the model. The subtidal changes can be important to aeolian sediment transport as the location and size of aeolian sediment erosion and deposition areas might change. To account for these changes, measured topographies are imposed to the model through a Basic Model Interface (BMI, Peckham et al., 2013, Appendix B.4).

All measured topographies in the period between September 1, 2011 and September 1, 2015 are linearly interpolated in time as to obtain daily updates of the Sand Motor's topography. The hydrodynamic mask is updated along with the topography. The presented aeolian sediment transport rates are based on the time-integrated entrainment and deposition rates that are computed by the model rather than differences in topography.

5.3.3 *Calibration*

The model is calibrated on the shape of roughness elements that emerge from the bed and shelter the sand surface from wind erosion, the drying rate of the soil and the time needed for the sediment transport to adapt to changing wind conditions. These processes are represented in the model by parameters for which data or literature can only provide approximate values:

1. σ, as used in the formulation of Raupach et al. (1993, Equation 4.2), is the ratio between the basal and frontal area of the roughness elements that constitute the beach armor layer.

2. T_{dry} is the time scale at which the beach dries out after flooding (Equation B.26). It represents the time in which the soil moisture content halves in case the beach is not inundated and no evaporation occurs.

3. T is the adaptation time scale in the right-hand side of the advection equation (Equation 4.7). It represents the time scale to which the sediment transport adapts to variations in the wind conditions and sediment availability.

The implementation of roughness elements is characterized by three calibration parameters: m, β and σ (Equation 4.13). m is a factor to account for the difference between the mean and maximum shear stress and is usually chosen as 0.5 for field applications (Raupach et al., 1993; McKenna Neuman et al., 2012). Numerically it is irrelevant if β or σ is calibrated as they only appear as a ratio $\frac{\beta}{\sigma}$ in the model implementation. As β is the ratio between the drag coefficient of the roughness elements alone and the drag coefficient of the unarmored sandy bed, the value can be assumed

to be reasonably generic. In contrast, σ depends on the shape and protrusion of the roughness elements and therefore depends on the field site and varies in time. For example, a spherical object placed on top of the bed would be represented by $\sigma = 1$, while a spherical object protruding halfway through the bed (hemisphere) would be represented by $\sigma = 2$. Consequently, calibration of σ seems to be preferable as it is less certain. Wind tunnel experiments presented by McKenna Neuman et al. (2012) investigated the influence of a lag deposits, consisting of shells and shell fragments, on aeolian sediment transport. Values for the calibration coefficients m and β were found to be 0.5 and 130 respectively and are adopted for the Sand Motor hindcast. An optimal average value for σ is obtained by systematic variation between 2 and 20.

The drying rate of the beach (T_{dry}) depends on many factors, like grain size, soil moisture content, groundwater level, wind speed and solar radiation. The use of a single time scale as aggregate for these processes is an oversimplification of reality. Therefore a wide range of parameter values is covered in the calibration. T_{dry} is varied between 0.1 and 10 hours where the former results in virtually instant drying and the latter results in an intertidal beach that is permanently too moist for aeolian sediment transport to be initiated.

The adaptation time scale (T), that represents the swiftness of aeolian sediment transport to adapt to changing wind conditions, is in the order of seconds (Davidson-Arnott et al., 2008; de Vries et al., 2014b). As the model time step is orders of magnitude larger, the model effectively solves steady states and the value for T will not affect temporal variations in sediment transport. However, the adaptation time scale also affects the development of the saltation cascade in space. Sediment transport increases in downwind direction from a zero-flux boundary, like the water line in case of onshore wind, with a rate that is governed by the value of T. Consequently, T influences the width of the source area in case of abundant sediment availability. T is varied between 1 and 10 seconds.

The calibration is performed based on the bi-monthly erosion and deposition volumes as measured in the Sand Motor domain (Hoonhout and de Vries, 2017a). The erosion and deposition volumes are determined within seven predefined zones (Figure 5.5) that aim to separate areas with marine influences from areas without marine influences, and separate areas with net aeolian erosion from areas with net aeolian deposition. The zonation is based on the 0, 3 and 5 m+MSL contour lines that roughly correspond with the mean water level, maximum runup level or berm edge and the dune foot respectively. The average R^2 value of the time series for erosion and deposition is used as benchmark. The R^2 value represents the fraction of explained variance and is defined as:

$$R^2 = \frac{\sum_n \left[V^n_{\text{measured}} - V^n_{\text{model}}\right]^2}{\sum_n \left[V^n_{\text{measured}} - \overline{V^n_{\text{measured}}}\right]^2} \tag{5.4}$$

where V^n is the measured or modeled sediment volume in time period n. The overbar denotes time-averaging. In addition the root-mean-square error (RMSE) is presented as absolute measure for the model accuracy, which is defined as:

$$\text{RMSE} = \sqrt{\sum_n \left[V^n_{\text{measured}} - V^n_{\text{model}}\right]^2} \tag{5.5}$$

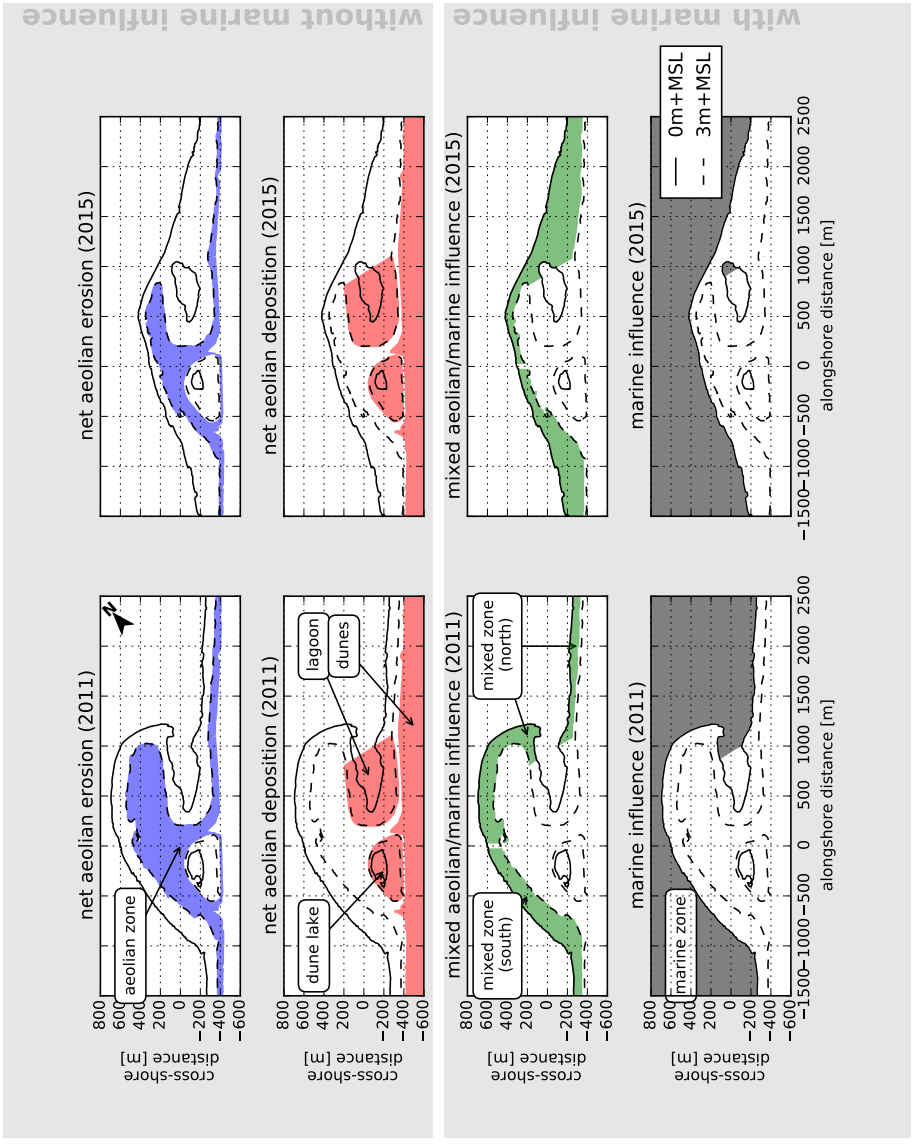

Figure 5.5: Zonation of the Sand Motor domain into zones with net aeolian erosion and no marine influence, net aeolian deposition and no marine influence, mixed aeolian/marine influence and marine influence. Zonation is based on the 0, 3 and 5 m+MSL contour lines that roughly correspond with the mean water level, maximum runup level or berm edge and the dune foot respectively. Left panels: 2011. Right panels: 2015. Source: Hoonhout and de Vries (2017a).

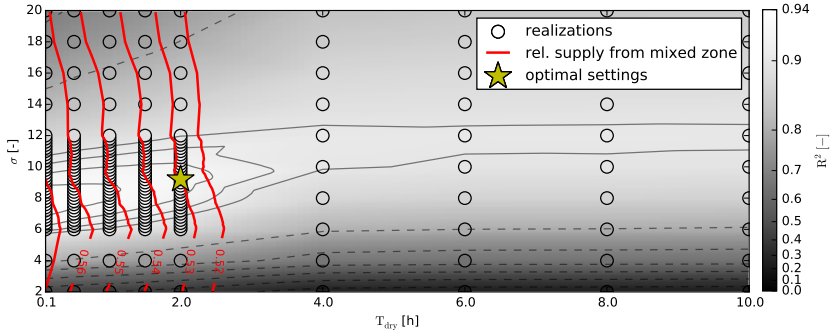

Figure 5.6: Systematic variation of calibration parameters σ and T_{dry} with T = 1 s. The circles indicate the realizations made. The colored background depicts a linear interpolation of the R^2 values with respect to the data presented in Figure 2.6. The solid isolines depict R^2 values from 0.90 to 0.93, while the dashed isolines depict R^2 values from 0.0 to 0.9. The red lines depict the relative supply from the mixed zones ranging from 52% to 57%. The yellow star indicates the optimal value model settings.

The calibration itself is performed in three steps:

1. A coarse calibration on σ and T_{dry}.
2. A calibration on T using the provisional optimal settings for σ and T_{dry}.
3. A fine calibration on σ and T_{dry} using the optimal setting for T.

5.4 RESULTS

The optimal model settings were chosen from 150 realizations (Figure 5.6). The optimal realization has an R^2 value of 0.93 and a RMSE of $3 \cdot 10^4$ m^3. The corresponding optimal parameter settings are found to be $\sigma = 9.2$, $T_{dry} = 2$ h and T = 1 s. These settings were ultimately selected from a cluster of realizations with comparable R^2 values based on the relative sediment supply from the mixed zones (Figure 5.5, third row) at the end of the simulation. An overview of all model settings for the calibrated model is given in Appendix C.

Figure 5.7 shows that erosion from the aeolian zone (Figure 5.5, first row) is most pronounced in the first year and least in the second year in both the measurements and the model results. Also the deposition of aeolian sediment in the dune lake and lagoon (Figure 5.5, second row) is observed in both the measurements and model results, although the model underestimates these deposited volumes. The deposition in the dune lake and lagoon is also more localized in the measurements than in the model results. The spatial variability in the erosion of the aeolian zone is larger in the measurements than in the model results. The large variability measured in the mixed zone is not present in the model results as hydrodynamic sediment transport is not simulated.

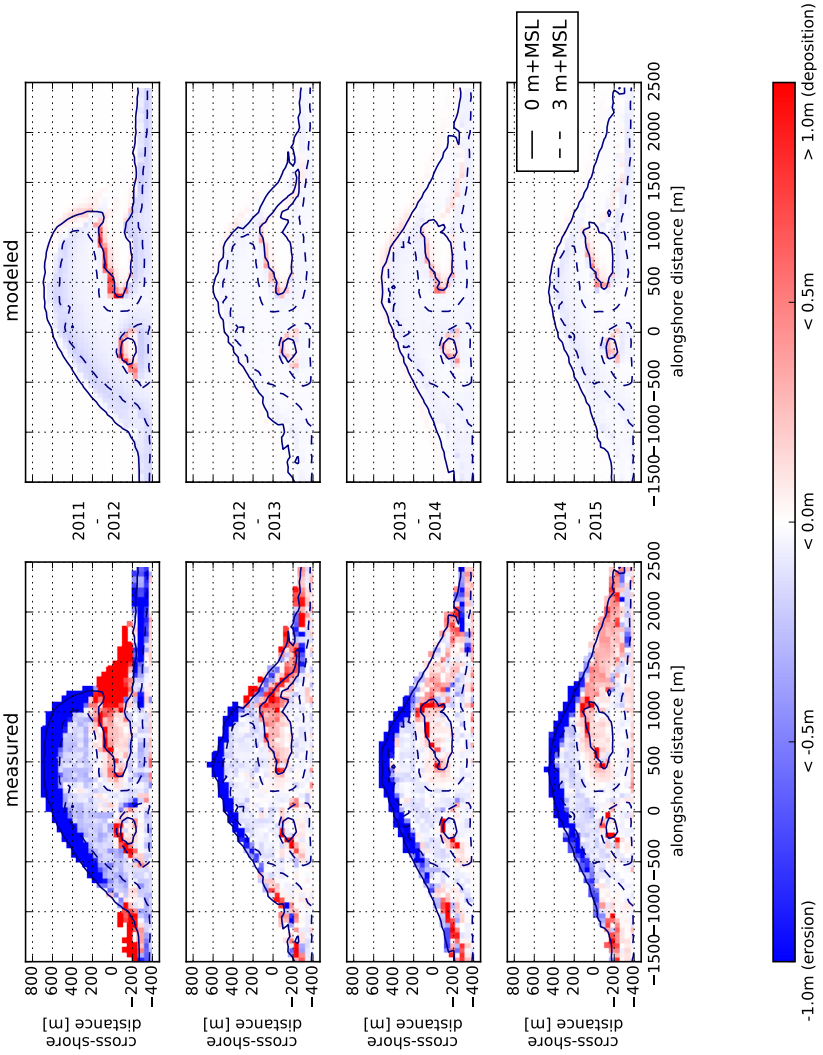

Figure 5.7: Measured and modeled yearly sedimentation and erosion above 0 m+MSL. Model results only include aeolian sediment transport as hydrodynamic sediment transport is not computed. Comparisons are made between the September surveys of each year.

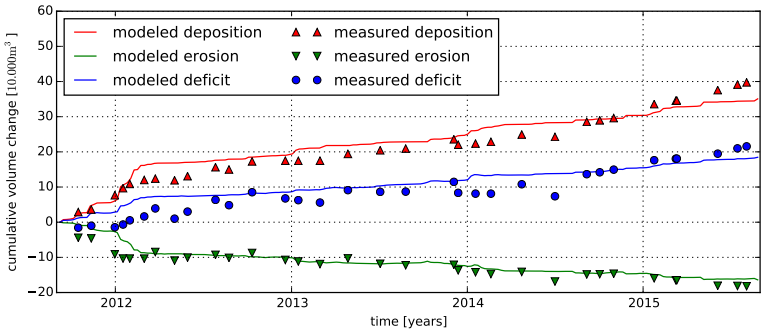

Figure 5.8: Measured and simulated net volume change of erosion and deposition volumes as presented in Figure 2.6.

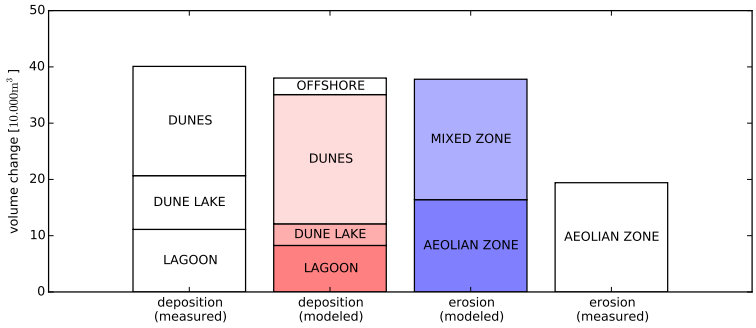

Figure 5.9: Total erosion and deposition volumes at the end of the simulation and measured total erosion and deposition volumes as presented in Figure 2.5.

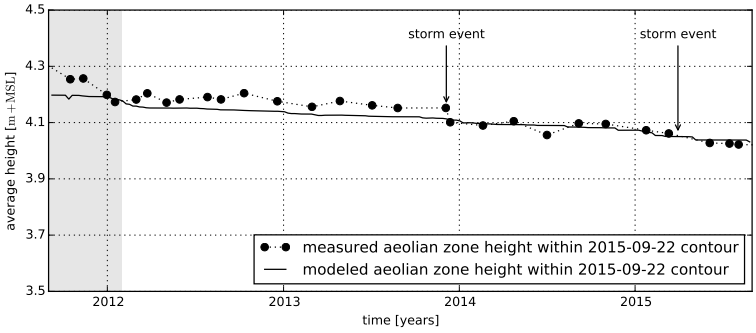

Figure 5.10: Measured and simulated average beach height in the aeolian zone as presented in Figure 2.8.

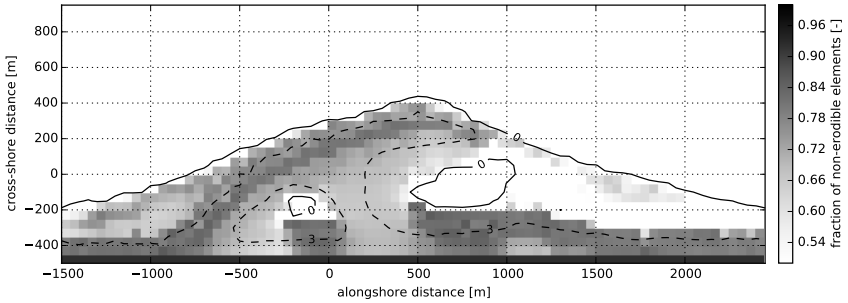

Figure 5.11: Simulated shell fraction in the aeolian zone at the end of the simulation.

The development of the total erosion and deposition volumes in the Sand Motor domain in the four year period is represented well by the model (Figure 5.8). The dune accumulation volume is overestimated at the expense of the sediment volumes deposited in the dune lake and lagoon (Figure 5.9). As the dune area is not included in the model domain, the sediment flux over the onshore boundary is assumed to settle in the dunes entirely. The total sediment accumulation at the end of the simulation is underestimated by 12% as the offshore sediment deposits are not included in the large scale sediment budget analysis that are used for comparison. The underestimation is unique for the last nine months of the simulation as the model overestimates the total sediment accumulation with 5% on average (Figure 5.8). The relative importance of the mixed zone as supplier of aeolian sediment is well captured.

The change in beach height within the most recent 3 m+MSL contour, that marks the aeolian zone, is represented by the model as the R^2 value is 0.71 and the RMSE is about 4 cm or 12% of the average bed level change (Figure 5.10). As the change in beach height is computed within the most recent 3 m+MSL contour, the discrepancy is illustrative for the differences in spatial variability in erosion between measurements and model results. The lowering of the beach in the aeolian zone in the first half year of the simulation is particularly underestimated, while the accelerated erosion in this period is well captured in the total sediment transport. This indicates that sediment is eroded from outside the most recent 3 m+MSL contour.

The coverage of non-erodible elements $\sigma\lambda$ [-] (Equation 4.14) in the aeolian zone varies between 60% and 80% at the end of the simulation (Figure 5.11). The coverage is high compared to the 10% – 20% shell coverage estimated to be present at the Sand Motor above 3 m+MSL based on gridded photographs.

Both the spatial and temporal variations in aeolian sediment availability are crucial for an accurate description of total sedimentation and erosion volumes as well as an accurate prediction of the aeolian sediment source and deposition areas. Figure 5.12 compares the total sedimentation volume according to measurements, the calibrated model and additional simulations, that are variations of the calibrated model in which spatial and/or temporal variations in the shear velocity threshold are averaged out. During these additional simulations the shear velocity threshold is not computed by the model, but space- and/or time-averaged thresholds based on the model results

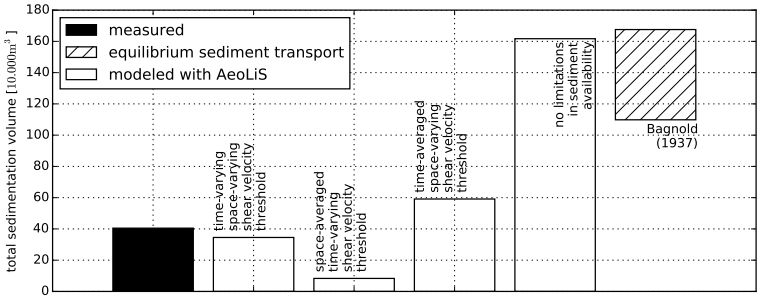

Figure 5.12: The influence of time-varying and space-varying shear velocity thresholds on the total sedimentation volume. The two leftmost bars depict the measured and modeled sedimentation volume as obtained from the calibrated model (Figure 5.9). The middle two bars depict results from two separate model simulations in which a space-averaged threshold time series or a time-averaged threshold field is imposed respectively. The threshold averages are based on the result from the calibrated model. The two rightmost columns depict a result from a separate model simulation with a constant uniform threshold based on only a constant uniform median grain size and the estimated equilibrium sediment transport following Bagnold (1937b) respectively (Table 5.1).

of the calibrated model are imposed. Negligence of the spatial variations results in a 79% underestimation of the total sedimentation volume and a relative contribution of 8% of the mixed zones. The negligence of the temporal variations results in a 46% overestimation of the total sedimentation volume and a relative contribution of 86% of the mixed zones. In addition, a simulation without limitations in sediment availability overestimates the measured total sedimentation volumes with 400%, which is comparable to the wind transport capacity following Bagnold (1937b, Figure 5.3).

5.5 DISCUSSION

The model results show that multi-annual aeolian sediment erosion and deposition volumes, and the relative importance of the mixed zones as source of aeolian sediment are reproduced with reasonable accuracy. This suggests that indeed significant limitations in sediment availability, due to soil moisture content and beach armoring, govern aeolian sediment transport in the Sand Motor domain. A comparison with a simulation without limitation in sediment availability suggests that aeolian sediment availability in the Sand Motor domain is limited to about 25% – 35% of the wind transport capacity.

The negligence of spatial variations causes the model to underestimate the measured total sedimentation volume. The sediment supply from the relatively small mixed zone is marginalized as the imposed space-averaged shear velocity threshold is relatively high. In contrast, the negligence of temporal variations causes the model to overestimate the measured total sedimentation volume. The sediment supply from the mixed zones is increased as the effect of its periodic flooding is averaged out. At the same time, the sediment supply from the aeolian zone is decreased as the influence of beach armoring affects sediment availability from the start of the simulation rather than after the development of the beach armor layer. Therefore, the total sedimentation volume is not only overestimated, but also the importance of the mixed zones as supplier of aeolian sediment.

5.5.1 *Seasonal and local variations in sedimentation and erosion*

The model can reproduce multi-annual trends in sedimentation volume, which is the aim of the hindcast, but seasonal and local variations are sometimes not represented by the model. An analysis of these variations is interesting as they influence the accuracy of specific model results.

Average wind speeds tend to be elevated in December and January (Figure 5.2), which leads to short periods of accelerated sediment accumulation in the beginning of 2012, 2013 and 2015 that are captured well by the model. Early 2014 no accelerated sediment accumulation is measured, while the model simulation shows an increase in sediment accumulation originating from the mixed zones similar to other years.

The discrepancy early 2014 might be explained by topographic changes induced by hydrodynamic forces. On December 5th, 2013 an exceptional storm hit the Dutch coast. During this storm a significant decrease in aeolian deposits in the lagoon was observed, while deposits in the dunes and dune lake increased only marginally. The assumption that the closed end of the lagoon is mainly governed by aeolian sediment transport might be violated in these exceptional conditions. At the same time, the

erosion of the aeolian zone that day equaled the total erosion of the aeolian zone that year. Consequently, the total subaerial sediment volume decreased that day with about $1 \cdot 10^4$ m^3, possibly caused by hydrodynamic forces. This suggests that the simplified hydrodynamics, despite the use of a hydrodynamic mask, are a limiting factor in describing the Sand Motor's subaerial morphodynamics during extreme storms.

In the first months of the simulation, the total sediment accumulation is well represented, but erosion of the aeolian zone is underestimated. As beach armoring is the most important availability limitation in the aeolian zone, this suggests that the armoring rate is overestimated by the model. The armoring rate is mainly influenced by initial shell fraction of 5%, which might be overestimated. Alternatively, the initially uniform distribution of shells in the bed is not an accurate representation of reality.

Measured erosion and deposition rates exceed modeled erosion and deposition rates in the final nine months of the simulation. In this period dune growth seems to accelerate, while neither the deposition in the dune lake and lagoon did accelerate nor did the wind speed increase. The apparent acceleration is therefore solely found in the half yearly lidar measurements of the dune area (Hoonhout and de Vries, 2017a) and is consequently based on a single data point. Despite the uncertainty involved in the measured acceleration, also precipitation rates, that were up to 70% lower in this period compared to the same period in other years, might explain the discrepancy at the end of the simulation (Jackson and Nordstrom, 1998). For the hindcast no precipitation time series are imposed as the effect on the aeolian sediment transport rate is not properly understood yet. Consequently, the calibration of the model might have resulted in an overestimated importance of beach armoring to compensate for the negligence of precipitation.

The distribution of the aeolian sediment deposits over the dune lake, lagoon and dunes is not represented well as deposits in the dune lake and lagoon are underestimated. Additional hydrodynamic and hydrologic processes, like wind setup and groundwater seepage, might cause the entrapment area in reality to be larger than modeled. But more importantly, the dune lake and lagoon are positioned in the lee of the Sand Motor crest with respect to the predominant southwesterly wind direction. The height difference between the Sand Motor crest and the water level in the lagoon and dune lake is several meters, which is likely to influence the local wind field significantly. The probable decrease in wind shear in the lee of the Sand Motor crest promotes deposition of aeolian sediment and likely hampers supply to the dunes. These local variations in wind shear are not included in the simulations.

5.5.2 *Beach armoring, sediment availability and the shear velocity threshold*

The influence of beach armoring is reflected in the model by both σ and the roughness density λ (Equation 4.13 and 4.14). The optimal value for σ was found to be 9.2, which is high compared to the value of 4.2 found by McKenna Neuman et al. (2012). The difference suggests that the roughness elements at the Sand Motor protrude less from the bed compared to what was found in the wind tunnel experiments. Consequently, the importance of beach armoring would be relatively low at the Sand Motor. However, the low σ value is largely compensated by the roughness density λ reflected in a shell coverage $\sigma\lambda$ that is high compared to what was found in the wind tunnel experiments (12% – 43% on average) and what is found at the Sand Motor field site

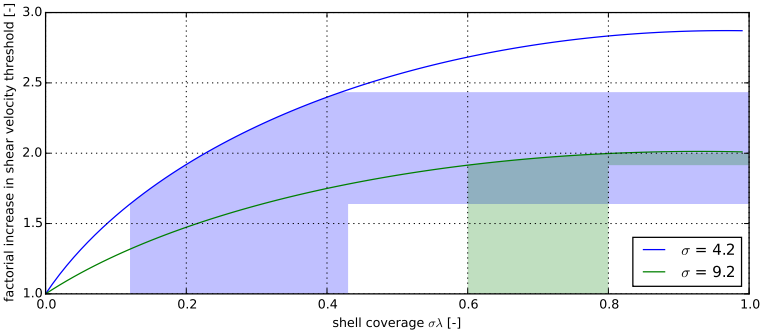

Figure 5.13: Relation between shear velocity threshold, shell coverage and σ according to Raupach et al. (1993, Equation 4.13). The shaded areas indicate the relevant parameter ranges from McKenna Neuman et al. (2012) (blue) and the model results (green).

(10% – 20%). Figure 5.13 shows that the combination of high shell coverage and σ value results in a very similar increase of the shear velocity threshold compared to the wind tunnel experiments presented by McKenna Neuman et al. (2012).

The reason that the model calibration resulted in this particular value for σ is that the model does not differentiate between the fluid and impact velocity threshold. Therefore, the roughness elements in the model affect the initiation of sediment transport equal to the continuation of sediment transport. The potential reduction in sediment availability increases with a decreasing value for σ (if $m = 0.5$, Figure 5.13) and is implemented through an increase in shear velocity threshold. The shear velocity threshold also affects aeolian sediment already in transport and originating from upwind, unarmored beach areas, like the mixed zones. Sediments from upwind areas are therefore partially deposited in the aeolian zone as soon a beach armor layer develops. For low values for σ the local deposition of sediment from upwind areas is already significant with low shell coverage. Low σ values therefore reduce the total sediment accumulation in the dunes quickly. In order for the model to provide reasonable total sediment transport rates, a higher value for σ was found in the calibration that ultimately induces a higher shell coverage. The value for σ therefore does not only represent a spatiotemporal averaged emergence of roughness elements, but also a compromise between its effect on the fluid and impact velocity threshold.

5.6 CONCLUSIONS

The Sand Motor hindcast shows that the reduction of aeolian sediment availability due to soil moisture and beach armoring can largely explain the low accumulation volumes in the Sand Motor domain. The AeoLiS model has shown to be quantitatively valuable and practically applicable. The model provides a framework for the description of complex spatiotemporal variations in aeolian sediment availability and its relation to sediment transport that has not yet been exploited in full.

From the hindcast the following conclusions can be drawn:

- The AeoLiS model is able to reproduce multi-annual aeolian sediment transport rates in the Sand Motor domain in the four years after its construction with a RMSE of $3 \cdot 10^4$ m^3 and R^2 of 0.93 when time series of measured and modeled total aeolian sediment transport volumes are compared.
- The AeoLiS model is able to reproduce large scale spatial patterns in aeolian sediment transport in the Sand Motor domain in the four years after its construction, but underestimates the deposition in the dune lake and lagoon.
- The AeoLiS model overestimates the total sedimentation volume with 5% on average, but underestimates the total sedimentation volume with 12% at the end of the simulation. The discrepancy at the end of the simulation might be caused by a particularly dry season as precipitation is not included in the simulations.
- The AeoLiS model is able to capture the seasonal variations in sediment transport in all years, except for early 2014 when significant morphological change is possibly related to hydrodynamic sediment transport that is not included in the simulations.
- The AeoLiS model overestimates the shell coverage, which compensates the high value for σ. The high σ value is a compromise between the fluid and impact threshold that are currently assumed to be equal.
- The combination of spatial and temporal variations in aeolian sediment availability, due to the combined influence of soil moisture, sediment sorting and beach armoring, and the feedback between aeolian sediment availability and transport is essential for an accurate estimate of the total sedimentation volume and the corresponding aeolian sediment source areas in the Sand Motor domain.

Part III

DISCUSSION AND CONCLUSIONS

6

DISCUSSION

This thesis explored the nature of aeolian sediment availability. Aeolian sediment availability is generally associated with the shear velocity threshold. Alternatively, sediment availability can be expressed in terms of critical fetch (Bauer and Davidson-Arnott, 2002) or explicitly following de Vries et al. (2014a). The latter two approaches deviate rather radically from the legacy of aeolian research. Both discard the abundantly available relations between bed surface properties, sediment availability and the shear velocity threshold. Instead, they describe sediment availability in new terms for which no quantification is known. In Chapter 4 it is argued that the new approaches have a right to exist as they allow for an increased complexity in situations that can be described by models. Ultimately, the approach of de Vries et al. (2014a) is adopted for this thesis and adapted to support multi-fraction sediment transport in order to simulate sediment sorting and beach armoring that introduces feedback between aeolian sediment availability and transport in aeolian sediment transport modeling.

The model approach presented in this thesis is a unification of the classic approach based on the shear velocity threshold and the approach of de Vries et al. (2014a). Whereas de Vries et al. (2014a) use a user-defined value for the sediment availability m_a (or S_e) to truncate the instantaneous sediment transport in their model, the approach presented in this thesis uses simulation to determine the local sediment availability $m_{a,k}$. The weighting factor $\hat{w}_k$ is subsequently adapted to the local sediment availability (Equation 4.9). Since the weighting factor $\hat{w}_k$ is essentially a space- and time-dependent modification to the shear velocity threshold, this new approach connects the field of availability-limited aeolian sediment transport modeling with the long history of aeolian research.

Availability-limited aeolian sediment transport modeling can be further improved by distinguishing between the fluid and impact threshold in future versions of the presented model. The presented model provides a framework in which such distinction can be made rather naturally. The bed interaction parameter essentially implements this distinction already for armored beach surfaces, but a more generic implementation is required for coastal systems with large spatial variations in sediment availability. A key issue is still that relations between bed surface properties, sediment availability and the shear velocity threshold are typically derived as bulk formulation for the fluid and impact threshold together. A proper implementation of the fluid and impact threshold in the presented model therefore depends on a substantial investment in data collection (Martin and Kok, 2016).

The presented model for availability-limited aeolian sediment transport can also be applied to availability-abundant coastal systems. However, much of the complexity in coastal aeolian sediment transport modeling is related to aeolian sediment availability. The approach might be considered too complex for more regular situations where sediment availability is abundant. A key issue is that assessing whether a coastal environment is availability-limited or not, is not trivial. In this thesis established formulations for equilibrium aeolian sediment transport are used to roughly estimate the sediment availability of coastal systems. However, if the presented model is proven to be sufficiently accurate in availability-abundant coastal systems, it might be used to formulate rules of thumb to assess coastal systems on their sediment availability more accurately. Subsequently, the model might be used to assess these coastal systems that are found to be availability-limited or facilitate the formulation of aggregated relations between aeolian sediment availability and transport that would serve a more rapid assessment.

In hindsight, the chapters in this thesis reveal a certain chronology in understanding the phenomenon of aeolian sediment availability. Deducing the significance of sediment availability from the large scale sediment budget analysis or the small scale sediment transport measurements was not trivial as sediment availability appeared to be rather intangible. This started with the slightly ambiguous use of terminology in literature where, for example, *sediment supply* is often mistaken to be equal to *sediment availability* or the *shear velocity threshold*. In addition, various aeolian, marine and meteorological processes affect aeolian sediment availability and/or the shear velocity threshold differently and on various temporal and spatial scales. Consequently, significant time was spent to narrow down the essence of sediment availability and define a distinctive terminology accordingly. The phenomenon of aeolian sediment availability was made tangible in a numerical model for aeolian sediment availability and transport that is unique in that it describes aspects essential to aeolian sediment availability and transport modeling that have previously been subject to research, but never been combined in a comprehensive model approach. The main contribution of the model is the *combined* simulation of:

1. Temporal variations in aeolian sediment availability and transport.
2. Spatial variations in aeolian sediment availability and transport.
3. Recurrence relation between aeolian sediment availability and transport through self-grading of sediment.
4. Simulation of multiple availability-limiting processes and their combined influence on aeolian sediment transport.
5. Natural differentiation between fluid and impact shear velocity threshold (not implemented).

6.1 MODEL IMPROVEMENTS

As illustrated by the Sand Motor hindcast presented in Chapter 5, the combined influence of various aspects of aeolian sediment availability is essential to obtain reliable estimates of aeolian sediment transport and dune growth for which the presented

model provides a general framework. Notwithstanding that model development just started and needs further extension, calibration and validation to make it generally applicable.

Based on the Sand Motor hindcast several opportunities for future model improvement have been identified:

- Support for local variations in wind shear due to morphological feedback.

  Neither deposition in front of the dunes nor deposition in the lee of the Sand Motor crest is currently simulated as morphological feedback with the wind is not taken into account. Given the discrepancy in the spatial distribution of aeolian sediment deposits between measurements and model result, it seems advisable to provide the model with local variations in wind shear. The model of Kroy et al. (2002) based on the derivation of the local wind field by Weng et al. (1991) might provide a description of the local variations in wind shear for which the computational effort relates well to the presented model.

- Support for the effect of wind gusts.

  The calibrated model is forced by an hourly averaged wind time series. The use of hourly averaged values for wind speed neglects the gustiness of the wind. Wind gusts might influence sediment transport significantly as the relation between wind speed and sediment transport is nonlinear. However, providing the model with high resolution wind time series would require a less diffusive numerical scheme that would likely not be computationally feasible for long-term simulations. Moreover, since saltation is not purely an advective mode of transport, the assumption of advection might be violated for very short time scales as interaction with the bed becomes dominant.

  As an alternative, the influence of gusts can be parameterized. It can be argued that some persistence is needed for gusts to influence sediment transport, resulting in a lower boundary of the temporal resolution of the wind time series. The distribution of the wind speed with respect to the hourly average can then provide a basis for a gustiness factor that increases the global wind shear.

- Support for differentiation between the fluid and impact shear velocity thresholds.

  The sediment transport capacity is currently implemented identical for the initiation and continuation of motion as no distinction between the fluid and impact threshold is made. The Sand Motor hindcast illustrates how this restriction affects the influence of roughness elements on aeolian sediment availability. Similar to the implementation of the bed interaction parameter, that distinguishes between the grain size distribution in the bed and the air, a distinction between fluid and impact threshold can be implemented.

  The right-hand side of the advection equation (Equation 4.9) can be modified according to:

$$E_k - D_k = \min\left(\frac{\partial m_{a,k}}{\partial t} \quad ; \quad \frac{\hat{w}_k}{T}\cdot\left[(1-S_k)\cdot c_{sat,k}^{fluid} + S_k \cdot c_{sat,k}^{impact} - c_k\right]\right) \quad (6.1)$$

where $c_{sat,k}^{fluid}$ [kg/m²] and $c_{sat,k}^{fluid}$ [kg/m²] are the sediment transport capacity associated with the fluid and impact threshold respectively and S_k [-] is the degree of saturation defined as:

$$S_k = \sum_{k=1}^{n_k} \frac{c_k}{c_{sat,k}^{impact}} \tag{6.2}$$

Note that the weighting factor $\hat{w}_k$ already distinguishes between sediment in the air and in the bed, depending on the saturation and the bed interaction parameter and therefore appears outside the brackets.

Although the presented model conceptually allows to differentiate between the impact and fluid threshold, empirical data to quantify the differentiation is lacking. This model improvement is therefore hypothetical at the current stage of development.

- Support for independent definition of the active bed layer.

  The top bed composition layer currently acts as active bed layer, but at the same time defines the vertical resolution of the sorting and armoring processes. As these are two fundamentally different properties of the model, it is advisable to define the active bed layer separate from the numerical resolution. A probability distribution can be defined that describes the probability of sediment to be eroded from a specific layer, which would logically decrease with the depth. The bed composition layer thickness would than uniquely determine the vertical resolution of sorting and armoring.

- Use of online coupling with other models

  The Sand Motor hindcast showed the importance of an accurate description of the hydrodynamics for accurate estimates of the development of the aeolian sedimentation and erosion volumes. Similarly, groundwater seepage might influence the aeolian sediment deposition around the lagoon and dune lake, which would require a description of the groundwater level to be implemented.

  It can be questioned if such detailed descriptions of hydrodynamic and hydrological processes are still within the scope of an aeolian sediment transport model. Alternatively, online model coupling with dedicated models for nearshore hydrodynamics and hydrology can be pursued. A Basic Model Interface (BMI) was implemented to accommodate model coupling.

6.2 MODEL VALIDATION

The Sand Motor appeared to be a valuable field site for investigating the influence of aeolian sediment availability on long-term aeolian sediment transport. The construction height, dry surface area and considerable beach armoring and compartmentalization amplify the processes governing aeolian sediment availability. These characteristics make the Sand Motor also a peculiar coastal site. The relative importance of processes governing aeolian sediment availability are likely to be different at a more ordinary coastal site. For example, beach armoring will not be as important

on narrow beaches that are frequently flooded. Preliminary model results for more ordinary coastal sites suggest that the extent of the compartmentalization of the beach is less, but spatiotemporal variations in aeolian sediment availability still influence aeolian sediment transport significantly. A comparison between field measurements from more ordinary coastal sites and model results can provide insight in the relative importance of these processes in general.

7

CONCLUSIONS

This thesis concludes with addressing the research questions formulated in the introductory chapter (Chapter 1).

RESEARCH OBJECTIVE A Identify the main sources for aeolian sediment at the Sand Motor mega nourishment (Chapter 2).

The research questions and answers related to this objective are:

A1 What is the total aeolian sediment supply at the Sand Motor mega nourishment?

The total aeolian sediment supply accumulated to 400.000 m^3 in the first four years after construction of the Sand Motor in 2011. The average accumulation rate during these four years was therefore 100.000 m^3/yr. In the first half year after construction the total accumulation was 120.000 m^3, indicating an average accumulation rate of 240.000 m^3/yr. From January 2012 the accumulation rate of aeolian sediment reduced with two-third to about 80.000 m^3/yr.

A2 What are the main deposition areas of aeolian sediment at the Sand Motor mega nourishment?

Aeolian sediment in the Sand Motor region is deposited in the dunes (50%), dune lake (25%) and lagoon (25%). The deposits in the dunes increased with respect to the dune lake and lagoon over the course of four years since construction of the Sand Motor. In addition, aeolian sediment is likely to be deposited offshore as well. The associated sediment volume is unknown, but estimated by the numerical model as 10% of the measured deposition volume.

A3 What are the main source areas of aeolian sediment at the Sand Motor mega nourishment?

Aeolian sediment in the Sand Motor region originates from the dry beach area (aeolian zone, 33%) and the intertidal and low-lying supratidal beach areas (mixed zones, 67%). The relative importance of the mixed zones is notable as it is periodically flooded and the majority of the northern mixed zone is oriented unfavorable with respect to the wind.

RESEARCH OBJECTIVE B Identify the main processes that govern aeolian sediment availability and supply at the Sand Motor mega nourishment (Chapter 3).

The research questions and answers related to this objective are:

B1 What processes govern the supply of aeolian sediment from the source areas?

Aeolian sediment supply at the Sand Motor is governed by the development of a beach armor layer. The reduction of aeolian sediment supply from the dry beach area due to the formation of a beach armor layer increases the contribution of the intertidal beach areas to the total aeolian sediment supply. Aeolian sediment supply from the intertidal and low-lying supratidal beach areas (mixed zone) is governed by the periodic flooding of the intertidal beach. The timescales involved in the flooding and drying of the intertidal beach seems to be short, resulting in a swift response of the sediment supply to the instantaneous waterline position. Local deposits on the berm flat seem to act as temporary sediment source during high water or high soil moisture contents resulting in a continuous supply from the mixed zone.

B2 What processes govern the deposition of aeolian sediment in the deposition areas?

Aeolian sediment deposits at the Sand Motor are found in areas with either limited wind shear, due to the presence of vegetation (dunes) or morphological feedback with the wind (lee of the Sand Motor crest), or high shear velocity thresholds, due to high soil moisture contents or free water surfaces (dune lake, lagoon and offshore). Local deposits on the berm flat seem to act as temporary sediment source during high water or high soil moisture contents resulting in a continuous supply from the intertidal beach. Alongshore variations in sediment deposition seem to be caused by blockage of aeolian sediment transport pathways.

B3 What bed surface characteristics are related to aeolian sediment supply?

Significant changes in spatial gradients in aeolian sediment transport at the Sand Motor coincide with the presence of a beach armor layer. This suggests that beach armoring is a dominant process in the reduction of aeolian sediment supply. Spatial gradients in aeolian sediment transport also seem to be related to topographic features, like the transition from berm slope to berm flat. Such features seem to promote deposition of aeolian sediment (negative supply).

RESEARCH OBJECTIVE C Describe the generic influence of spatiotemporal variations in aeolian sediment availability on aeolian sediment transport in coastal environments (Chapter 4).

The research questions and answers related to this objective are:

C1 What are existing approaches to describe the influence of aeolian sediment availability on aeolian sediment transport, what are the similarities and differences among them and which approaches are mutually exclusive?

Three main approaches can be distinguished in literature: the shear velocity threshold, the critical fetch and the explicit formulation of sediment availability. All approaches are related, but differ in the amount of spatiotemporal variability in sediment availability they can allow. The approach based on critical fetch is mutually exclusive with the approach based on the explicit formulation of sediment availability as the latter provides the critical fetch as model result. The approach based on an explicit formulation of sediment availability is, in the form presented in this thesis, a spatiotemporal advection framework for the shear velocity threshold that in addition allows for feedback between aeolian sediment availability and transport as well as differentiation between the impact and fluid threshold.

C2 What processes that were identified to be relevant to aeolian sediment availability are not covered with sufficient accuracy by existing approaches?

Spatiotemporal variations in beach armoring is shown to be a governing process at the Sand Motor mega nourishment. Especially the spatiotemporal variations are not sufficiently accurately described in existing models for aeolian sediment transport.

C3 What are the requirements for an approach that harmonizes existing, mutual inclusive approaches and is conceptually able to describe the processes relevant to aeolian sediment availability and transport?

The approach is based on the legacy of aeolian research as relations between aeolian sediment availability and transport are abundantly available and should be used. The approach describes feedback between wind and transport as well as sediment availability and transport. It distinguishes between the fluid and impact threshold.

RESEARCH OBJECTIVE D Validate the numerical model approach to reproduce the location and size of sources for aeolian sediment at the Sand Motor mega nourishment (Chapter 5).

The research questions and answers related to this objective are:

D1 Can the calibrated numerical model reproduce the total aeolian sediment supply at the Sand Motor mega nourishment with any statistical significance?

Yes. The total aeolian sediment supply over the course of 4 years is represented with an R^2 value of 0.93 and an RMSE of $3 \cdot 10^4$ Mm^3.

D2 Can the calibrated numerical model reproduce the main source and deposition areas at the Sand Motor mega nourishment?

Yes. The relative contribution of the intertidal beach was estimated to be 55% based on the large scale sediment budget analysis, which is represented by the calibrated model.

D3 What implemented processes are significant to the model result?

Both the drying of the intertidal beach and sediment sorting and beach armoring are crucial for the model result. Moreover, both the spatial and temporal variations affect the model result significantly.

Part IV

APPENDICES

A

THEORETICAL SEDIMENT TRANSPORT VOLUMES

The cumulative theoretical sediment transport volume Q [m^3] in the Sand Motor domain between September 1, 2011 and September 1, 2015 is estimated from hourly averaged measured wind speed u_{10} [m/s] and direction θ_u [°] measured at 10 m height by the KNMI meteorological station in Hoek van Holland (Figure 2.2). The wind time series are used in conjunction with the formulation of Bagnold (1937b) to obtain the instantaneous theoretical sediment transport rate q [kg/m/s] following:

$$q = C\frac{\rho_a}{g}\sqrt{\frac{d_n}{D_n}}\,(u_* - u_{*th})^3 \tag{A.1}$$

with the shear velocity $u_* = \alpha \cdot u_{10}$ m/s, the shear velocity threshold $u_{*th} = \alpha \cdot 3.87$ m/s, the conversion factor from free-flow wind velocity to shear velocity $\alpha = 0.058$, the air density ρ_a = 1.25 kg/m^3, the particle density ρ_p = 2650.0 kg/m^3, the gravitational constant g = 9.81 m/s^2, the nominal grain size d_n = 335 μm and a reference grain size D_n = 250 μm.

The cumulative theoretical sediment transport volumes in onshore (Q_{os} [m^3]) and alongshore (Q_{as} [m^3]) direction are computed by time integration and conversion from mass to volume following:

$$\begin{array}{rcl} Q_{os} & = & \sum q \cdot \frac{\Delta t \cdot \Delta y}{(1-p)\cdot \rho_p} \cdot f_{\theta_u,os} \quad = \quad 110 \cdot 10^4 \text{ m}^3 \\ Q_{as} & = & \sum q \cdot \frac{\Delta t \cdot \Delta x}{(1-p)\cdot \rho_p} \cdot f_{\theta_u,as} \quad = \quad 3 \cdot 10^4 \text{ m}^3 \end{array} \tag{A.2}$$

where the temporal resolution Δt = 1 h, the alongshore span of the measurement domain Δy = 4 km, the approximate lateral beach width Δx = 100 m, the porosity p = 0.4 and $f_{\theta_u,os}$ and $f_{\theta_u,as}$ are factors to account for respectively the onshore and alongshore wind directions only, defined as:

$$\begin{array}{rcl} f_{\theta_u,os} & = & \max(0 \quad ; \quad \cos(312° - \theta_u)) \\ f_{\theta_u,as} & = & \sin(312° - \theta_u) \end{array} \tag{A.3}$$

where θ_u [°] is the hourly averaged wind direction and 312 ° accounts for orientation of the original coastline.

Note that the difference between the onshore and alongshore cumulative theoretical sediment transport volumes (Equation A.2) of a factor 40 is determined solely by the difference between the onshore and alongshore cross-sections of 4 km and 100 m respectively. The sediment transport volumes per meter width in onshore and alongshore direction are of the same order of magnitude (275 m^3/m and 267 m^3/m respectively).

B

NUMERICAL IMPLEMENTATION

The numerical implementation of the equations presented in Chapter 4 is explained in this appendix. The implementation is available as Python package through the OpenEarth GitHub repository at: github.com/openearth/aeolis-python/

B.1 ADVECTION EQUATION

The advection equation (Equation 4.6) is implemented in two-dimensional form following:

$$\frac{\partial c}{\partial t} + u_{z,x}\frac{\partial c}{\partial x} + u_{z,y}\frac{\partial c}{\partial y} = \frac{c_{sat} - c}{T} \tag{B.1}$$

in which c [kg/m^2] is the sediment mass per unit area in the air, c_{sat} [kg/m^2] is the maximum sediment mass in the air that is reached in case of saturation, $u_{z,x}$ and $u_{z,y}$ are the x- and y-component of the wind velocity at height z [m], T [s] is an adaptation time scale, t [s] denotes time and x [m] and y [m] denote cross-shore and alongshore distances respectively.

The formulation is discretized following a first order upwind scheme assuming that the wind velocity u_z is positive in both x-direction and y-direction:

$$\frac{c^{n+1}_{i,j,k} - c^{n}_{i,j,k}}{\Delta t^n} + u^n_{z,x}\frac{c^n_{i,j,k} - c^n_{i-1,j,k}}{\Delta x_{i,j}} + u^n_{z,y}\frac{c^n_{i,j,k} - c^n_{i,j-1,k}}{\Delta y_{i,j}} = \frac{\hat{w}^n_{i,j,k} \cdot c^n_{sat,i,j,k} - c^n_{i,j,k}}{T} \tag{B.2}$$

in which n is the time step index, i and j are the cross-shore and alongshore spatial grid cell indices and k is the grain size fraction index. w [-] is the weighting factor defined in Equation 4.10a and used for the weighted addition of the saturated sediment concentrations over all grain size fractions.

The discretization can be generalized for any wind direction as:

$$\frac{c^{n+1}_{i,j,k} - c^{n}_{i,j,k}}{\Delta t^n} + u^n_{z,x+}c^n_{i,j,k,x-} + u^n_{z,y+}c^n_{i,j,k,y-} + u^n_{z,x-}c^n_{i,j,k,x+} + u^n_{z,y-}c^n_{i,j,k,y+} = \frac{\hat{w}^n_{i,j,k} \cdot c^n_{sat,i,j,k} - c^n_{i,j,k}}{T} \tag{B.3}$$

in which:

$$\begin{array}{rclcrcl} u^n_{z,x+} & = & \max(0, u^n_{z,x}) & ; & u^n_{z,y+} & = & \max(0, u^n_{z,y}) \\ u^n_{z,x-} & = & \min(0, u^n_{z,x}) & ; & u^n_{z,y-} & = & \min(0, u^n_{z,y}) \end{array} \tag{B.4}$$

and

$$\begin{array}{rclcrcl} c^n_{i,j,k,x+} & = & \frac{c^n_{i+1,j,k} - c^n_{i,j,k}}{\Delta x} & ; & c^n_{i,j,k,y+} & = & \frac{c^n_{i,j+1,k} - c^n_{i,j,k}}{\Delta y} \\ c^n_{i,j,k,x-} & = & \frac{c^n_{i,j,k} - c^n_{i-1,j,k}}{\Delta x} & ; & c^n_{i,j,k,y-} & = & \frac{c^n_{i,j,k} - c^n_{i,j-1,k}}{\Delta y} \end{array} \tag{B.5}$$

Equation B.3 is explicit in time and adheres to the Courant-Friedrich-Lewis (CFL) condition for numerical stability. Alternatively, the advection equation can be discretized implicitly in time for unconditional stability:

$$\begin{aligned} \frac{c^{n+1}_{i,j,k} - c^n_{i,j,k}}{\Delta t^n} + u^{n+1}_{z,x+} c^{n+1}_{i,j,k,x-} + u^{n+1}_{z,y+} c^{n+1}_{i,j,k,y-} \\ + u^{n+1}_{z,x-} c^{n+1}_{i,j,k,x+} + u^{n+1}_{z,y-} c^{n+1}_{i,j,k,y+} = \frac{\hat{w}^{n+1}_{i,j,k} \cdot c^{n+1}_{sat,i,j,k} - c^{n+1}_{i,j,k}}{T} \end{aligned} \tag{B.6}$$

Equation B.3 and B.6 can be rewritten as:

$$\begin{aligned} c^{n+1}_{i,j,k} = c^n_{i,j,k} - \Delta t^n \Bigg[u^n_{z,x+} c^n_{i,j,k,x-} + u^n_{z,y+} c^n_{i,j,k,y-} \\ + u^n_{z,x-} c^n_{i,j,k,x+} + u^n_{z,y-} c^n_{i,j,k,y+} - \frac{\hat{w}^n_{i,j,k} \cdot c^n_{sat,i,j,k} - c^n_{i,j,k}}{T} \Bigg] \end{aligned} \tag{B.7}$$

and

$$\begin{aligned} c^{n+1}_{i,j,k} + \Delta t^n \Bigg[u^{n+1}_{z,x+} c^{n+1}_{i,j,k,x-} + u^{n+1}_{z,y+} c^{n+1}_{i,j,k,y-} \\ + u^{n+1}_{z,x-} c^{n+1}_{i,j,k,x+} + u^{n+1}_{z,y-} c^{n+1}_{i,j,k,y+} - \frac{\hat{w}^{n+1}_{i,j,k} \cdot c^{n+1}_{sat,i,j,k} - c^{n+1}_{i,j,k}}{T} \Bigg] = c^n_{i,j,k} \end{aligned} \tag{B.8}$$

and combined using a weighted average:

$$\begin{aligned} c^{n+1}_{i,j,k} + \Gamma \Delta t^n \Bigg[u^{n+1}_{z,x+} c^{n+1}_{i,j,k,x-} + u^{n+1}_{z,y+} c^{n+1}_{i,j,k,y-} \\ + u^{n+1}_{z,x-} c^{n+1}_{i,j,k,x+} + u^{n+1}_{z,y-} c^{n+1}_{i,j,k,y+} - \frac{\hat{w}^{n+1}_{i,j,k} \cdot c^{n+1}_{sat,i,j,k} - c^{n+1}_{i,j,k}}{T} \Bigg] \\ = c^n_{i,j,k} - (1-\Gamma) \Delta t^n \Bigg[u^n_{z,x+} c^n_{i,j,k,x-} + u^n_{z,y+} c^n_{i,j,k,y-} \\ + u^n_{z,x-} c^n_{i,j,k,x+} + u^n_{z,y-} c^n_{i,j,k,y+} - \frac{\hat{w}^n_{i,j,k} \cdot c^n_{sat,i,j,k} - c^n_{i,j,k}}{T} \Bigg] \end{aligned} \tag{B.9}$$

in which Γ is a weight that ranges from $0-1$ and determines the implicitness of the scheme. The scheme is implicit with $\Gamma = 0$, explicit with $\Gamma = 1$ and semi-implicit otherwise. $\Gamma = 0.5$ results in the semi-implicit Crank-Nicolson scheme.

Equation B.5 is back-substituted in Equation B.9:

$$\begin{aligned}
c_{i,j,k}^{n+1} + \Gamma\Delta t^n \Bigg[& u_{z,x+}^{n+1} \frac{c_{i,j,k}^{n+1} - c_{i-1,j,k}^{n+1}}{\Delta x} + u_{z,y+}^{n+1} \frac{c_{i,j,k}^{n+1} - c_{i,j-1,k}^{n+1}}{\Delta y} \\
& + u_{z,x-}^{n+1} \frac{c_{i+1,j,k}^{n+1} - c_{i,j,k}^{n+1}}{\Delta x} + u_{z,y-}^{n+1} \frac{c_{i,j+1,k}^{n+1} - c_{i,j,k}^{n+1}}{\Delta y} - \frac{\hat{w}_{i,j,k}^{n+1} \cdot c_{sat,i,j,k}^{n+1} - c_{i,j,k}^{n+1}}{T} \Bigg] \\
& = c_{i,j,k}^{n} - (1-\Gamma)\Delta t^n \Bigg[u_{z,x+}^{n} \frac{c_{i,j,k}^{n} - c_{i-1,j,k}^{n}}{\Delta x} + u_{z,y+}^{n} \frac{c_{i,j,k}^{n} - c_{i,j-1,k}^{n}}{\Delta y} \\
& + u_{z,x-}^{n} \frac{c_{i+1,j,k}^{n} - c_{i,j,k}^{n}}{\Delta x} + u_{z,y-}^{n} \frac{c_{i,j+1,k}^{n} - c_{i,j,k}^{n}}{\Delta y} - \frac{\hat{w}_{i,j,k}^{n} \cdot c_{sat,i,j,k}^{n} - c_{i,j,k}^{n}}{T} \Bigg]
\end{aligned} \tag{B.10}$$

and rewritten:

$$\begin{aligned}
& \left[1 + \Gamma \left(u_{z,x+}^{n+1} \frac{\Delta t^n}{\Delta x} + u_{z,y+}^{n+1} \frac{\Delta t^n}{\Delta y} - u_{z,x-}^{n+1} \frac{\Delta t^n}{\Delta x} - u_{z,y-}^{n+1} \frac{\Delta t^n}{\Delta y} + \frac{\Delta t^n}{T} \right) \right] c_{i,j,k}^{n+1} \\
& - \Gamma \left(u_{z,x+}^{n+1} \frac{\Delta t^n}{\Delta x} c_{i-1,j,k}^{n+1} + u_{z,y+}^{n+1} \frac{\Delta t^n}{\Delta y} c_{i,j-1,k}^{n+1} - u_{z,x-}^{n+1} \frac{\Delta t^n}{\Delta x} c_{i+1,j,k}^{n+1} - u_{z,y-}^{n+1} \frac{\Delta t^n}{\Delta y} c_{i,j+1,k}^{n+1} \right) \\
& = \left[1 - (1-\Gamma) \left(u_{z,x+}^{n} \frac{\Delta t^n}{\Delta x} + u_{z,y+}^{n} \frac{\Delta t^n}{\Delta y} - u_{z,x-}^{n} \frac{\Delta t^n}{\Delta x} - u_{z,y-}^{n} \frac{\Delta t^n}{\Delta y} + \frac{\Delta t^n}{T} \right) \right] c_{i,j,k}^{n} \\
& + (1-\Gamma) \left(u_{z,x+}^{n} \frac{\Delta t^n}{\Delta x} c_{i-1,j,k}^{n} + u_{z,y+}^{n} \frac{\Delta t^n}{\Delta y} c_{i,j-1,k}^{n} - u_{z,x-}^{n} \frac{\Delta t^n}{\Delta x} c_{i+1,j,k}^{n} - u_{z,y-}^{n} \frac{\Delta t^n}{\Delta y} c_{i,j+1,k}^{n} \right) \\
& \qquad + \Gamma \hat{w}_{i,j,k}^{n+1} \cdot c_{sat,i,j,k}^{n+1} \frac{\Delta t^n}{T} + (1-\Gamma) \hat{w}_{i,j,k}^{n} \cdot c_{sat,i,j,k}^{n} \frac{\Delta t^n}{T}
\end{aligned} \tag{B.11}$$

and simplified:

$$a_{i,j}^{0,0} c_{i,j,k}^{n+1} + a_{i,j}^{1,0} c_{i+1,j,k}^{n+1} + a_{i,j}^{0,1} c_{i,j+1,k}^{n+1} - a_{i,j}^{-1,0} c_{i-1,j,k}^{n+1} - a_{i,j}^{0,-1} c_{i,j-1,k}^{n+1} = y_{i,j,k} \tag{B.12}$$

where the implicit coefficients are defined as:

$$\begin{aligned}
a_{i,j}^{0,0} &= \left[1 + \Gamma \left(u_{z,x+}^{n+1} \tfrac{\Delta t^n}{\Delta x} + u_{z,y+}^{n+1} \tfrac{\Delta t^n}{\Delta y} - u_{z,x-}^{n+1} \tfrac{\Delta t^n}{\Delta x} - u_{z,y-}^{n+1} \tfrac{\Delta t^n}{\Delta y} + \tfrac{\Delta t^n}{T} \right) \right] \\
a_{i,j}^{1,0} &= \Gamma u_{z,x+}^{n+1} \tfrac{\Delta t^n}{\Delta x} \\
a_{i,j}^{0,1} &= \Gamma u_{z,y+}^{n+1} \tfrac{\Delta t^n}{\Delta y} \\
a_{i,j}^{-1,0} &= \Gamma u_{z,x-}^{n+1} \tfrac{\Delta t^n}{\Delta x} \\
a_{i,j}^{0,-1} &= \Gamma u_{z,y-}^{n+1} \tfrac{\Delta t^n}{\Delta y}
\end{aligned} \tag{B.13}$$

and the explicit right-hand side as:

$$
\begin{aligned}
y^n_{i,j,k} = &\left[1-(1-\Gamma)\left(u^n_{z,x+}\frac{\Delta t^n}{\Delta x}+u^n_{z,y+}\frac{\Delta t^n}{\Delta y}-u^n_{z,x-}\frac{\Delta t^n}{\Delta x}-u^n_{z,y-}\frac{\Delta t^n}{\Delta y}+\frac{\Delta t^n}{T}\right)\right]c^n_{i,j,k}\\
&+(1-\Gamma)\left(u^n_{z,x+}\frac{\Delta t^n}{\Delta x}c^n_{i-1,j,k}+u^n_{z,y+}\frac{\Delta t^n}{\Delta y}c^n_{i,j-1,k}-u^n_{z,x-}\frac{\Delta t^n}{\Delta x}c^n_{i+1,j,k}-u^n_{z,y-}\frac{\Delta t^n}{\Delta y}c^n_{i,j+1,k}\right)\\
&+\Gamma\hat{w}^{n+1}_{i,j,k}\cdot c^{n+1}_{sat,i,j,k}\frac{\Delta t^n}{T}+(1-\Gamma)\hat{w}^n_{i,j,k}\cdot c^n_{sat,i,j,k}\frac{\Delta t^n}{T} \qquad \text{(B.14)}
\end{aligned}
$$

The offshore boundary is defined to be zero-flux, the onshore boundary has a constant transport gradient and the lateral boundaries are circular:

$$
\begin{aligned}
c^{n+1}_{1,j,k} &= 0\\
c^{n+1}_{n_x+1,j,k} &= 2c^{n+1}_{n_x,j,k}-c^{n+1}_{n_x-1,j,k}\\
c^{n+1}_{i,1,k} &= c^{n+1}_{i,n_y+1,k}\\
c^{n+1}_{i,n_y+1,k} &= c^{n+1}_{i,1,k}
\end{aligned} \qquad \text{(B.15)}
$$

These boundary conditions can be combined with Equation B.12, B.13 and B.14 into a linear system of equations:

$$
\begin{bmatrix}
A^0_1 & A^1_1 & \mathbf{0} & \cdots & \mathbf{0} & A^{n_y+1}_1\\
A^{-1}_2 & A^0_2 & \ddots & \ddots & & \mathbf{0}\\
\mathbf{0} & \ddots & \ddots & \ddots & \ddots & \vdots\\
\vdots & \ddots & \ddots & \ddots & \ddots & \mathbf{0}\\
\mathbf{0} & & \ddots & \ddots & A^0_{n_y} & A^1_{n_y}\\
A^{-n_y-1}_{n_y+1} & \mathbf{0} & \cdots & \mathbf{0} & A^{-1}_{n_y+1} & A^0_{n_y+1}
\end{bmatrix}
\begin{bmatrix}
\vec{c}_1\\ \vec{c}_2\\ \vdots\\ \vdots\\ \vec{c}_{n_y}\\ \vec{c}_{n_y+1}
\end{bmatrix}
=
\begin{bmatrix}
\vec{y}_1\\ \vec{y}_2\\ \vdots\\ \vdots\\ \vec{y}_{n_y}\\ \vec{y}_{n_y+1}
\end{bmatrix} \qquad \text{(B.16)}
$$

where each item in the matrix is again a matrix A^l_j and each item in the vectors is again a vector $\vec{c}_j$ and $\vec{y}_j$ respectively. The form of the matrix A^l_j depends on the diagonal index l and reads:

$$
A^0_j = \begin{bmatrix}
0 & 0 & 0 & 0 & \cdots & \cdots & 0\\
a^{0,-1}_{2,j} & a^{0,0}_{2,j} & a^{0,1}_{2,j} & \ddots & & & \vdots\\
0 & a^{0,-1}_{3,j} & a^{0,0}_{3,j} & a^{0,1}_{3,j} & \ddots & & \vdots\\
\vdots & \ddots & \ddots & \ddots & \ddots & \ddots & \vdots\\
\vdots & & \ddots & a^{0,-1}_{n_x-1,j} & a^{0,0}_{n_x-1,j} & a^{0,1}_{n_x-1,j} & 0\\
\vdots & & & 0 & a^{0,-1}_{n_x,j} & a^{0,0}_{n_x,j} & a^{0,1}_{n_x,j}\\
0 & \cdots & \cdots & 0 & 1 & -2 & 1
\end{bmatrix} \qquad \text{(B.17)}
$$

for $l = 0$ and

$$A_j^l = \begin{bmatrix} 1 & 0 & \cdots & \cdots & \cdots & \cdots & 0 \\ 0 & a_{2,j}^{l,0} & \ddots & & & & \vdots \\ \vdots & \ddots & a_{3,j}^{l,0} & \ddots & & & \vdots \\ \vdots & & \ddots & \ddots & \ddots & & \vdots \\ \vdots & & & \ddots & a_{n_x-1,j}^{l,0} & \ddots & \vdots \\ \vdots & & & & \ddots & a_{n_x,j}^{l,0} & 0 \\ 0 & \cdots & \cdots & \cdots & \cdots & 0 & 1 \end{bmatrix} \tag{B.18}$$

for $l \neq 0$. The vectors $\vec{c}_{j,k}$ and $\vec{y}_{j,k}$ read:

$$\vec{c}_{j,k} = \begin{bmatrix} c_{1,j,k}^{n+1} \\ c_{2,j,k}^{n+1} \\ c_{3,j,k}^{n+1} \\ \vdots \\ c_{n_x-1,j,k}^{n+1} \\ c_{n_x,j,k}^{n+1} \\ c_{n_x+1,j,k}^{n+1} \end{bmatrix} \quad \text{and } \vec{y}_{j,k} = \begin{bmatrix} 0 \\ y_{2,j,k}^{n} \\ y_{3,j,k}^{n} \\ \vdots \\ y_{n_x-1,j,k}^{n} \\ y_{n_x,j,k}^{n} \\ 0 \end{bmatrix} \tag{B.19}$$

n_x and n_y denote the number of spatial grid cells in x- and y-direction.

B.2 IMPLICIT SOLVER

The linear system defined in Equation B.16 is solved by a sparse matrix solver for each sediment fraction separately in ascending order of grain size. Initially, the weights $\hat{w}_{i,j,k}^{n+1}$ are chosen according to the grain size distribution in the bed and the air following Equation 4.10b. The sediment availability constraint based on Equation 4.9 is checked after each solve:

$$m_{a,k} \geqslant \frac{\hat{w}_{i,j,k}^{n+1} c_{sat,i,j,k}^{n+1} - c_{i,j,k}^{n+1}}{T} \Delta t^n \tag{B.20}$$

If the constraint if violated, a new estimate for the weights is back-calculated following:

$$\hat{w}_{i,j,k}^{n+1} = \frac{c_{i,j,k}^{n+1} + m_{a,k} \frac{\Delta t^n}{T}}{c_{sat,i,j,k}^{n+1}} \tag{B.21}$$

The system is solved again using the new weights. This procedure is repeated until a weight is found that does not violate the sediment availability constraint. If the time step is not too large, the procedure typically converges in only a few iterations. Finally, the weights of the larger grains are increased proportionally as to ensure that the sum of all weights remains unity. If no larger grains are defined, not enough sediment is available for transport and the grid cell is truly availability-limited. This

situation should only occur occasionally as the weights in the next time step are computed based on the new bed composition and thus will be skewed towards the large fractions. If the situation occurs regularly, the time step is chosen too large compared to the rate of armoring.

B.3 SHEAR VELOCITY THRESHOLD

The shear velocity threshold represents the influence of bed surface properties in the saturated sediment transport equation (Equation 4.8). The shear velocity threshold is computed for each grid cell and sediment fraction separately based on local bed surface properties, like moisture, roughness elements and salt content. For each bed surface property supported by the model a factor is computed to increase the initial shear velocity threshold:

$$u_{*th} = f_{u_{*th},M} \cdot f_{u_{*th},R} \cdot f_{u_{*th},S} \cdot u_{*th,0} \tag{B.22}$$

The initial shear velocity threshold $u_{*th,0}$ [m/s] is computed based on the grain size following Bagnold (1937a):

$$u_{*th,0} = A\sqrt{\frac{\rho_p - \rho_a}{\rho_a} \cdot g \cdot d_n} \tag{B.23}$$

where A [-] is an empirical constant, ρ_p [kg/m^3] is the grain density, ρ_a [kg/m^3] is the air density, g [m/s^2] is the gravitational constant and d_n [m] is the nominal grain size of the sediment fraction.

B.3.1 *Moisture content*

The shear velocity threshold is updated based on moisture content following Belly (1964):

$$f_{u_{*th},M} = \max(1 \quad ; \quad 1.8 + 0.6 \cdot \log(p_g)) \tag{B.24}$$

where $f_{u_{*th,M}}$ [-] is a factor in Equation B.22, p_g [-] is the geotechnical mass content of water, which is the percentage of water compared to the dry mass. The geotechnical mass content relates to the volumetric water content p_V [-] according to:

$$p_g = \frac{p_V \cdot \rho_w}{\rho_p \cdot (1 - p)} \tag{B.25}$$

where ρ_w [kg/m^3] and ρ_p [kg/m^3] are the water and particle density respectively and p [-] is the porosity. Values for p_g smaller than 0.005 do not affect the shear velocity threshold (Pye and Tsoar, 1990). Values larger than 0.064 (or 10% volumetric content) cease transport (Delgado-Fernandez, 2010), which is implemented as an infinite shear velocity threshold.

Exploratory model runs of the unsaturated soil with the HYDRUS1D (Šimůnek et al., 1998) hydrology model show that the increase of the volumetric water content to saturation is almost instantaneous with rising tide. The drying of the beach surface through infiltration shows an exponential decay. In order to capture this behavior the volumetric water content is implemented according to:

$$p_V^{n+1} = \begin{cases} p & \text{if } \eta > z_b \\ p_V^n \cdot e^{\frac{\log(0.5)}{T_{dry}} \cdot \Delta t^n} - E_v \cdot \frac{\Delta t^n}{\Delta z} & \text{if } \eta \leqslant z_b \end{cases} \tag{B.26}$$

where η [m+MSL] is the instantaneous water level, z_b [m+MSL] is the local bed elevation, p_V^n [-] is the volumetric water content in time step n, Δt^n [s] is the model time step and Δz is the bed composition layer thickness. T_{dry} [s] is the beach drying time scale, defined as the time in which the beach moisture content halves. E_v [m/s] is the evaporation rate that is implemented through an adapted version of the Penman equation (Shuttleworth, 1993):

$$E_v = \frac{m_v \cdot R_n + 6.43 \cdot \gamma_v \cdot (1 + 0.536 \cdot u_2) \cdot \delta e}{\lambda_v \cdot (m_v + \gamma_v)} \cdot 9 \cdot 10^7 \tag{B.27}$$

where m_v [kPa/K] is the slope of the saturation vapor pressure curve, R_n [MJ/m^2/day] is the net radiance, γ_v [kPa/K] is the psychrometric constant, u_2 [m/s] is the wind speed at 2 m above the bed, δe [kPa] is the vapor pressure deficit (related to the relative humidity) and λ_v [MJ/kg] is the latent heat vaporization. To obtain an evaporation rate in [m/s], the original formulation is multiplied by $9 \cdot 10^7$.

B.3.2 *Roughness elements*

The shear velocity threshold is updated based on the presence of roughness elements following Raupach et al. (1993):

$$f_{u_{*th,R}} = \sqrt{(1 - m \cdot \sum_{k=k_0}^{n_k} \hat{w}_k^{bed})(1 + \frac{m\beta}{\sigma} \cdot \sum_{k=k_0}^{n_k} \hat{w}_k^{bed})} \tag{B.28}$$

by assuming:

$$\lambda = \frac{\sum_{k=k_0}^{n_k} \hat{w}_k^{bed}}{\sigma} \tag{B.29}$$

where $f_{u_{*th,R}}$ [-] is a factor in Equation B.22, k_0 is the sediment fraction index of the smallest non-erodible fraction in current conditions and n_k is the number of sediment fractions defined. The implementation is discussed in detail in section 4.4.4.

B.3.3 *Salt content*

The shear velocity threshold is updated based on salt content following Nickling and Ecclestone (1981):

$$f_{u_{*th,S}} = 1.03 \cdot \exp(0.1027 \cdot p_s) \tag{B.30}$$

where $f_{u_{*th,S}}$ [-] is a factor in Equation B.22 and p_s [-] is the salt content [mg/g]. Currently, no model is implemented that predicts the instantaneous salt content. The spatial varying salt content needs to be specified by the user, for example through the BMI interface.

B.3.4 *Masks*

To account for spatial differences in hydrodynamics without the necessity to run a separate hydrodynamic model, the model supports hydrodynamic masks. Without such mask the model imposes the still water levels and offshore wave heights uniformly to all grid cells where the bed level is below the instantaneous water level. The tidal range and mean water level are therefore uniform throughout the model domain. In addition, the still water level underestimates the local water level as wave runup is not taken into account. Only wave heights are maximized by a constant and uniform ratio between wave height and water depth (Equation 4.15).

For cases where the assumption of uniform hydrodynamics hydrodynamics, the uniformly imposed instantaneous still water level η [m+MSL] and offshore wave height H [m] can be converted to a local water level $\hat{\eta}$ [m+MSL] and wave height $\hat{H}$ [m] using a hydrodynamic mask, following:

$$\begin{aligned} \hat{H} &= H \cdot K^{\times} \\ \hat{\eta} &= \eta \cdot K^{\times} + K^{+} + R \end{aligned} \tag{B.31}$$

where K is the hydrodynamic mask, consisting of a multiplication mask ($K^{\times}$ [-]) and an addition mask (K^{+} [m]). The multiplication mask can be used to reduce the tidal range and the addition mask can subsequently be used to elevate the mean water level. The hydrodynamic mask is applied before the wave height is maximized by the maximum ratio between wave height and water depth (Equation 4.15). R [m] is an estimate for the wave runup height following Battjes (1974):

$$\frac{R}{H} = \xi \tag{B.32}$$

where ξ [-] is the surf similarity parameter with a value between 1.0 and 2.3.

B.4 BASIC MODEL INTERFACE (BMI)

A Basic Model Interface (BMI, Peckham et al., 2013) is implemented that allows interaction with the model during run time. The model can be implemented as a library within a larger framework as the interface exposes the initialization, finalization and time stepping routines. As a convenience functionality the current implementation supports the specification of a callback function. The callback function is called at the start of each time step and can be used to exchange data with the model, e.g. update the topography from measurements.

An example of a callback function, that is referenced in the model input file or through the model command-line options as "callback.py:update", is:

callback.py

```
1 import numpy as np
2
3 def update(model):
4     val = model.get_var('zb').copy()
5     val[:,:] = np.loadtxt('measured_topography.txt')
6     model.set_var('zb', val)
```

C

MODEL SETTINGS

Unless stated otherwise, the model schematizations presented in chapter 5 used the settings listed below. Some model settings belong to experimental features of the model and are not discussed in this thesis. These settings are listed for completeness only and marked with an asterisk (*). The model settings are chosen such that experimental features are disabled.

Parameter	Value
A	0.085
CFL	1.0
Cb	1.5
T	1.0
Tdry	5400.0
Tsalt*	0.0
accfac	1.0
bedupdate	False
beta	130.0
bi	0.05
boundary_lateral	circular
boundary_offshore	noflux
boundary_onshore	gradient
callback	None
cpair	0.0010035
csalt*	0.035
dt	3600.0
eps	0.001
evaporation	True
facDOD	0.1
g	9.81
gamma	0.5
grain_dist	0.005709 0.234708 0.608887 0.099666 0.001029 0.000001 0.010486 0.028503 0.010486 0.000522 0.000004
grain_size	0.000177 0.000250 0.000354 0.000500 0.000707 0.001000 0.002000 0.004000 0.008000 0.016000 0.032000
k	0.01
layer_thickness	0.01
m	0.5

Parameter	Value	(continued)
max_error	0.000001	
max_iter	1000	
method_moist	belly_johnson	
method_transport	bagnold	
mixtoplayer	True	
nfractions	11	
nlayers	10	
output_times	604800.0	
porosity	0.4	
restart	None	
rhoa	1.25	
rhop	2650.0	
rhow	1025.0	
runup	False	
scheme	euler_backward	
sigma	11.9	
th_bedslope	False	
th_grainsize	True	
th_humidity*	False	
th_moisture	True	
th_roughness	True	
th_salt*	False	
tstart	0.0	
tstop	126230400.0	
z	10.0	

BIBLIOGRAPHY

Aagaard, T. (2014). Sediment supply to beaches: Cross-shore sand transport on the lower shoreface. *Journal of Geophysical Research*, 119(4):913–926. doi:10.1002/2013JF003041. 2013JF003041.

Aagaard, T., Davidson-Arnott, R., Greenwood, B., and Nielsen, J. (2004). Sediment supply from shoreface to dunes: linking sediment transport measurements and long-term morphological evolution. *Geomorphology*, 60(1):205–224. doi:10.1016/j.geomorph.2003.08.002.

Anthony, E. J. (2013). Storms, shoreface morphodynamics, sand supply, and the accretion and erosion of coastal dune barriers in the southern north sea. *Geomorphology*, 199:8–21. doi:10.1016/j.geomorph.2012.06.007.

Arens, S., Baas, A., Van Boxel, J., and Kalkman, C. (2001). Influence of reed stem density on foredune development. *Earth Surface Processes and Landforms*, 26(11):1161–1176.

Arens, S., Van Boxel, J., and Abuodha, J. (2002). Changes in grain size of sand in transport over a foredune. *Earth Surface Processes and Landforms*, 27(11):1163–1175.

Arens, S. M. (1996). Patterns of sand transport on vegetated foredunes. *Geomorphology*, 17:339–350.

Bagnold, R. (1935). The movement of desert sand. *Geographical Journal*, pages 342–365.

Bagnold, R. (1937a). The size-grading of sand by wind. *Proceedings of the Royal Society of London. Series A, Mathematical and Physical Sciences*, pages 250–264.

Bagnold, R. (1937b). The transport of sand by wind. *Geographical journal*, pages 409–438.

Barchyn, T. E., Hugenholtz, C. H., Li, B., McKenna Neuman, C., and Sanderson, S. (2014a). From particle counts to flux: Wind tunnel testing and calibration of the "wenglor" aeolian sediment transport sensor. *Aeolian Research*, 15:311–318. doi:10.1016/j.aeolia.2014.06.009.

Barchyn, T. E., Martin, R. L., Kok, J. F., and Hugenholtz, C. H. (2014b). Fundamental mismatches between measurements and models in aeolian sediment transport prediction: The role of small-scale variability. *Aeolian Research*, 15:245–251. doi:10.1016/j.aeolia.2014.07.002.

Battjes, J. A. (1974). *Computation of set-up, longshore currents, run-up and overtopping due to wind-generated waves*. PhD thesis, TU Delft, Delft University of Technology.

Bauer, B. O. and Davidson-Arnott, R. G. D. (2002). A general framework for modeling sediment supply to coastal dunes including wind angle, beach geometry, and fetch effects. *Geomorphology*, 49:89–108. doi:10.1016/S0169-555X(02)00165-4.

Bauer, B. O., Davidson-Arnott, R. G. D., Hesp, P. A., Namikas, S. L., Ollerhead, J., and Walker, I. J. (2009). Aeolian sediment transport on a beach: Surface moisture, wind fetch, and mean transport. *Geomorphology*, 105:106–116. doi:10.1016/j.geomorph.2008.02.016.

Belly, P. Y. (1964). Sand movement by wind. Technical Report 1, U.S. Army Corps of Engineers CERC, Vicksburg, MS. 38 pp.

Borsje, B. W., van Wesenbeeck, B. K., Dekker, F., Paalvast, P., Bouma, T. J., van Katwijk, M. M., and de Vries, M. B. (2011). How ecological engineering can serve in coastal protection. *Ecological Engineering*, 37(2):113–122. doi:10.1016/j.ecoleng.2010.11.027.

Buscombe, D., Rubin, D. M., and Warrick, J. A. (2010). A universal approximation of grain size from images of noncohesive sediment. *Journal of Geophysical Research*, 115(F2). doi:10.1029/2009JF001477. F02015.

Cheng, H., Liu, C., Zou, X., Li, J., He, J., Liu, B., Wu, Y., Kang, L., and Fang, Y. (2015). Aeolian creeping mass of different grain sizes over sand beds of varying length. *Journal of Geophysical Research*. doi:10.1002/2014JF003367. 2014JF003367.

Darke, I. and McKenna Neuman, C. (2008). Field study of beach water content as a guide to wind erosion potential. *Journal of Coastal Research*, 24(5):1200–1208. doi:10.2112/00-000.1.

Davidson-Arnott, R. G., White, D. C., and Ollerhead, J. (1997). The effects of artificial pebble concentrations on eolion sand transport on a beach. *Canadian Journal of Earth Sciences*, 34(11):1499–1508.

Davidson-Arnott, R. G. D. and Bauer, B. O. (2009). Aeolian sediment transport on a beach: Thresholds, intermittency, and high frequency variability. *Geomorphology*, 105:117–126. doi:10.1016/j.geomorph.2008.02.018.

Davidson-Arnott, R. G. D. and Law, M. N. (1990). *Coastal Dunes: Form and Process*, chapter Seasonal patterns and controls on sediment supply to coastal foredunes, Long Point, Lake Erie, pages 177–200. Wiley Chichester.

Davidson-Arnott, R. G. D., MacQuarrie, K., and Aagaard, T. (2005). The effect of wind gusts, moisture content and fetch length on sand transport on a beach. *Geomorphology*, 68:115–129. doi:10.1016/j.geomorph.2004.04.008.

Davidson-Arnott, R. G. D., Yang, Y., Ollerhead, J., Hesp, P. A., and Walker, I. J. (2008). The effects of surface moisture on aeolian sediment transport threshold and mass flux on a beach. *Earth Surface Processes and Landforms*, 33(1):55–74. doi:10.1002/esp.1527.

De Schipper, M., De Vries, S., Ranasinghe, R., Reniers, A., and Stive, M. (2013). Alongshore topographic variability at a nourished beach. In *Coastal Dynamics 2013: 7th International Conference on Coastal Dynamics, Arcachon, France, 24-28 June 2013*. Bordeaux University.

de Schipper, M. A., de Vries, S., Ruessink, G., de Zeeuw, R. C., Rutten, J., van Gelder-Maas, C., and Stive, M. J. (2016). Initial spreading of a mega feeder nourishment: Observations of the sand engine pilot project. *Coastal Engineering*, 111:23–38. doi:10.1016/j.coastaleng.2015.10.011.

de Vriend, H. J., van Koningsveld, M., Aarninkhof, S. G., de Vries, M. B., and Baptist, M. J. (2015). Sustainable hydraulic engineering through building with nature. *Journal of Hydro-environment Research*, 9(2):159–171. doi:10.1016/j.jher.2014.06.004.

de Vries, S., Arens, S. M., de Schipper, M. A., and Ranasinghe, R. (2014a). Aeolian sediment transport on a beach with a varying sediment supply. *Aeolian Research*, 15:235–244. doi:10.1016/j.aeolia.2014.08.001.

de Vries, S., Radermacher, M., de Schipper, M., and Stive, M. (2015). Tidal dynamics in the Sand Motor lagoon. In *E-proceedings of the 36th IAHR World Congress*.

de Vries, S., van Thiel de Vries, J. S. M., van Rijn, L. C., Arens, S. M., and Ranasinghe, R. (2014b). Aeolian sediment transport in supply limited situations. *Aeolian Research*, 12:75–85. doi:10.1016/j.aeolia.2013.11.005.

Delft3D-FLOW Manual (2014). *Delft3D - 3D/2D modelling suite for integral water solutions - Hydro-Morphodynamics*. Deltares, Delft. Version 3.15.34158.

Delgado-Fernandez, I. (2010). A review of the application of the fetch effect to modelling sand supply to coastal foredunes. *Aeolian Research*, 2:61–70. doi:10.1016/j.aeolia.2010.04.001.

Delgado-Fernandez, I., Davidson-Arnott, R., Bauer, B. O., Walker, I. J., Ollerhead, J., and Rhew, H. (2012). Assessing aeolian beach-surface dynamics using a remote sensing approach. *Earth Surface Processes and Landforms*, 37(15):1651–1660. doi:10.1002/esp.3301.

Delgado-Fernandez, I. and Davidson-Arnott, R. A. (2011). Meso-scale aeolian sediment input to coastal dunes: The nature of aeolian transport events. *Geomorphology*, 126(1):217–232. doi:10.1016/j.geomorph.2010.11.005.

Donchyts, G., Baart, F., Winsemius, H., Gorelick, N., Kwadijk, J., and van de Giesen, N. (2016). Earth's surface water change over the past 30 years. *Nature Climate Change*, 6(9):810–813. doi:10.1038/nclimate3111.

Dong, Z., Wang, H., Liu, X., and Wang, X. (2004a). The blown sand flux over a sandy surface: a wind tunnel investigation on the fetch effect. *Geomorphology*, 57:117–127. doi:10.1016/S0169-555X(03)00087-4.

Dong, Z., Wang, H., Liu, X., and Wang, X. (2004b). A wind tunnel investigation of the influences of fetch length on the flux profile of a sand cloud blowing over a gravel surface. *Earth Surface Processes and Landforms*, 29(13):1613–1626. doi:10.1002/esp.1116.

Dupont, S., Bergametti, G., and Simoëns, S. (2014). Modeling aeolian erosion in presence of vegetation. *Journal of Geophysical Research*, 119(2):168–187. doi:10.1002/2013JF002875.

Dyer, K. R. (1986). *Coastal and estuarine sediment dynamics*. Wiley, Chichester.

Dymin (1954). quoted by Greeley and Iversen (1985).

Edwards, B. L. and Namikas, S. L. (2009). Small-scale variability in surface moisture on a fine-grained beach: implications for modeling aeolian transport. *Earth Surface Processes and Landforms*, 34:1333–1338. doi:10.1002/esp.1817.

Edwards, B. L., Namikas, S. L., and D'Sa, E. J. (2013). Simple infrared techniques for measuring beach surface moisture. *Earth Surface Processes and Landforms*, 38(2):192–197. doi:10.1002/esp.3319.

Gallagher, E. L., MacMahan, J., Reniers, A., Brown, J., and Thornton, E. B. (2011). Grain size variability on a rip-channeled beach. *Marine Geology*, 287(1):43–53. doi:10.1016/j.margeo.2011.06.010.

Gillette, D. A. and Stockton, P. H. (1989). The effect of nonerodible particles on wind erosion of erodible surfaces. *Journal of Geophysical Research: Atmospheres*, 94(D10):12885–12893. doi:10.1029/JD094iD10p12885.

Gillies, J. A., Nickling, W. G., and King, J. (2006). Aeolian sediment transport through large patches of roughness in the atmospheric inertial sublayer. *Journal of Geophysical Research: Earth Surface*, 111(F2). doi:10.1029/2005JF000434. F02006.

Grunnet, N. M. and Ruessink, B. (2005). Morphodynamic response of nearshore bars to a shoreface nourishment. *Coastal Engineering*, 52(2):119–137. doi:10.1016/j.coastaleng.2004.09.006.

Hamm, L., Capobianco, M., Dette, H., Lechuga, A., Spanhoff, R., and Stive, M. (2002). A summary of european experience with shore nourishment. *Coastal engineering*, 47(2):237–264. doi:10.1016/S0378-3839(02)00127-8.

Hesp, P. A. and Smyth, T. A. G. (2016). Surfzone-beach-dune interactions: Flow and sediment transport across the intertidal beach and backshore. *Journal of Coastal Research*, SI 75:8–12. doi:10.2112/SI75-002.1.

Hoonhout, B. M. (2013). Monitoring the process of aeolian transport. In *Proceedings of the NCK-days 2013*.

Hoonhout, B. M. (2016a). Aeolis model setups v2.0. GIT repository. doi:10.5281/zenodo.58837.

Hoonhout, B. M. (2016b). Aeolis v1.1: A process-based model for simulating availability-limited aeolian sediment transport. GIT repository. doi:10.5281/zenodo.58854.

Hoonhout, B. M., Baart, F., and Van Thiel de Vries, J. S. M. (2014a). Intertidal beach classification in infrared images. *Journal of Coastal Research*, SI 66:657–662.

Hoonhout, B. M., Cohn, N., de Vries, S., Roelvink, J. A., Ruggiero, P., Moore, L. J., Durán, O., and Goldstein, E. (2016a). How tides and waves enhance aeolian sediment transport at the Sand Motor. In *Proceedings of the Ocean Sciences Meeting 2016*, New Orleans, USA.

Hoonhout, B. M. and de Vries, S. (2014a). Modelling and monitoring of meso-scale supply-limited aeolian transport. In *Proceedings of the NCK-days 2014*.

Hoonhout, B. M. and de Vries, S. (2014b). Process-based modeling of supply-limited aeolian transport in coastal environments. In *Proceedings of the International Conference on Aeolian Research 2014*, Lanzhou, China.

Hoonhout, B. M. and de Vries, S. (2016a). Aeolis: A new model for aeolian sediment supply and transport. In *Proceedings of the NCK-days 2016*.

Hoonhout, B. M. and de Vries, S. (2016b). A process-based model for aeolian sediment transport and spatiotemporal varying sediment availability. *Journal of Geophysical Research: Earth Surface*. doi:10.1002/2015JF003692. 2015JF003692.

Hoonhout, B. M. and de Vries, S. (2017a). Aeolian sediment supply at a mega nourishment. *Coastal Engineering*. Submitted.

Hoonhout, B. M. and de Vries, S. (2017b). Field measurements on spatial variations in aeolian sediment availability at the Sand Motor mega nourishment. *Aeolian Research*, 24:93–104. doi:10.1016/j.aeolia.2016.12.003.

Hoonhout, B. M., de Vries, S., Baart, F., van Thiel de Vries, J. S. M., van der Weerd, L., and Wijnberg, K. M. (2013). Monitoring of beach surface properties with remote sensing. In *Proceedings of Coastal Dynamics*, Arcachon, France.

Hoonhout, B. M., de Vries, S., and Cohn, N. (2015a). The influence of spatially varying supply on coastal aeolian transport: a field experiment. In *Proceedings of Coastal Sediments*, San Diego, USA.

Hoonhout, B. M., de Vries, S., and Cohn, N. (2015b). The influence of spatially varying supply on coastal aeolian transport: A field experiment. In *Proceedings of the NCK-days 2015*.

Hoonhout, B. M., de Vries, S., and Cohn, N. (2016b). Field measurements on aeolian sediment transport at the Sand Motor mega nourishment during the MegaPeX field campaign. OpenDAP server. doi:10.4121/uuid:3bc3591b-9d9e-4600-8705-5b7eba6aa3ed.

Hoonhout, B. M. and den Heijer, C. (2010). Reliability of dune erosion assessment along curved coastlines. In *Proceedings of the 32nd International Conference on Coastal Engineering*, Shanghai, China.

Hoonhout, B. M. and Radermacher, M. (2015a). Annotated images of the dutch coast. FTP server. doi:10.4121/uuid:08400507-4731-4cb2-a7ec-9ed2937db119.

Hoonhout, B. M. and Radermacher, M. (2015b). Flamingo: a coastal image analysis toolbox. GIT repository. doi:10.5281/zenodo.14596.

Hoonhout, B. M., Radermacher, M., Baart, F., and Van der Maaten, L. J. P. (2015c). An automated method for semantic classification of regions in coastal images. *Coastal Engineering*, 105:1–12. doi:10.1016/j.coastaleng.2015.07.010.

Hoonhout, B. M. and van Thiel de Vries, J. S. M. (2012). Modeling dune erosion, overwash and inundation of barrier islands. In *Proceedings of the 33rd International Conference on Coastal Engineering*, Santander, Spain.

Hoonhout, B. M., van Thiel de Vries, J. S. M., Curto, V., and Stive, M. J. F. (2014b). Monitoring supply limiting conditions using imageing techniques. In *Proceedings of the 34th International Conference on Coastal Engineering*, Seoul, Korea.

Horikawa, K., Hotta, S., Kubota, S., and Katori, S. (1983). On the sand transport rate by wind on a beach. *Coastal Engineering in Japan*, 26:101–120.

Hotta, S., Kubota, S., Katori, S., and Horikawa, K. (1984). Sand transport by wind on a wet sand beach. In *Proceedings of the 19th Conference on Coastal Engineering*, pages 1264–1281, Houston, TX. ASCE.

Houser, C. (2009). Synchronization of transport and supply in beach-dune interaction. *Progress in Physical Geography*, 33(6):733–746. doi:10.1177/0309133309350120.

Houser, C. and Ellis, J. (2013). Beach and dune interaction. *Treatise on geomorphology. Academic, San Diego*. doi:10.1016/B978-0-12-374739-6.00283-9.

Howard, A. D. (1977). Effect of slope on the threshold of motion and its application to orientation of wind ripples. *Geological Society of America Bulletin*, 88(6):853–856. doi:10.1130/0016-7606(1977)88¡853:EOSOTT¿2.0.CO;2.

Hsu, S.-A. (1971). Wind stress criteria in eolian sand transport. *Journal of Geophysical Research*, 76(36):8684–8686.

Hugenholtz, C. H. and Barchyn, T. E. (2011). Laboratory and field performance of a laser particle counter for measuring aeolian sand transport. *Journal of Geophysical Research*, 116(F1). doi:10.1029/2010JF001822. F01010.

Iversen, J. D. and Rasmussen, K. R. (2006). The effect of surface slope on saltation threshold. *Sedimentology*, 41(4):721–728. doi:10.1111/j.1365-3091.1994.tb01419.x.

Jackson, D. W. T. and Cooper, J. A. G. (1999). Beach fetch distance and aeolian sediment transport. *Sedimentology*, 46:517–522. doi:10.1046/j.1365-3091.1999.00228.x.

Jackson, N. L. and Nordstrom, K. F. (1998). Aeolian transport of sediment on a beach during and after rainfall, wildwood, nj, usa. *Geomorphology*, 22(2):151–157. doi:10.1016/S0169-555X(97)00065-2.

Jackson, N. L. and Nordstrom, K. F. (2011). Aeolian sediment transport and landforms in managed coastal systems: a review. *Aeolian research*, 3(2):181–196. doi:10.1016/j.aeolia.2011.03.011.

Jackson, N. L., Nordstrom, K. F., Saini, S., and Smith, D. R. (2010). Effects of nourishment on the form and function of an estuarine beach. *Ecological Engineering*, 36(12):1709–1718. doi:10.1016/j.ecoleng.2010.07.016.

Johnson, J. W. (1965). Sand movement on coastal dunes. Technical Report 570, Symp. 3, Paper no. 75, U.S. Department of Agriculture, Washington. pp 747-755.

Kawamura, R. (1951). Study of sand movement by wind. Technical Report HEL-2-8, Hydraulics Engineering Laboratory, Univeristy of California, Berkeley.

King, C. A. M. (1951). Depth of disturbance of sand on sea beaches by waves. *Journal of Sedimentary Petrology*, 21(3):131–140.

King, J., Nickling, W. G., and Gillies, J. A. (2005). Representation of vegetation and other nonerodible elements in aeolian shear stress partitioning models for predicting transport threshold. *Journal of Geophysical Research*, 110(F4). doi:10.1029/2004JF000281. F04015.

Kocurek, G. and Lancaster, N. (1999). Aeolian system sediment state: theory and mojave desert kelso dune field example. *Sedimentology*, 46(3):505–515. doi:10.1046/j.1365-3091.1999.00227.x.

Kroy, K., Sauermann, G., and Herrmann, H. J. (2002). Minimal model for sand dunes. *Physical Review Letters*, 88(5):054301. doi:10.1103/PhysRevLett.88.054301.

Lancaster, N. and Baas, A. (1998). Influence of vegetation cover on sand transport by wind: field studies at owens lake, california. *Earth Surface Processes and Landforms*, 23(1):69–82.

Lettau, K. and Lettau, H. (1978). *Exploring the World's Driest Climate.*, chapter Experimental and micrometeorological field studies of dune migration., pages 110–147. University of Wisconsin - Madison. IES Report 101,.

Li, J., Okin, G. S., Herrick, J. E., Belnap, J., Miller, M. E., Vest, K., and Draut, A. E. (2013). Evaluation of a new model of aeolian transport in the presence of vegetation. *Journal of Geophysical Research*, 118(1):288–306. doi:10.1002/jgrf.20040.

Lynch, K., Jackson, D. W., and Cooper, J. A. G. (2016). The fetch effect on aeolian sediment transport on a sandy beach: a case study from magilligan strand, northern ireland. *Earth Surface Processes and Landforms*. doi:10.1002/esp.3930.

Lynch, K., Jackson, D. W. T., and Cooper, J. A. G. (2008). Aeolian fetch distance and secondary airflow effects: the influence of micro-scale variables on meso-scale foredune development. *Earth Surface Processes and Landforms*, 33(7):991–1005. doi:10.1002/esp.1582.

Martin, R. L. and Kok, J. F. (2016). Field measurements demonstrate distinct initiation and cessation thresholds governing aeolian sediment transport flux. Submitted.

Masselink, G., Auger, N., Russell, P., and O'Hare, T. (2007). Short-term morphological change and sediment dynamics in the intertidal zone of a macrotidal beach. *Sedimentology*, 54:39–53. doi:10.1111/j.1365-3091.2006.00825.x.

McKenna Neuman, C., Li, B., and Nash, D. (2012). Micro-topographic analysis of shell pavements formed by aeolian transport in a wind tunnel simulation. *Journal of Geophysical Research*, 117(F4). doi:10.1029/2012JF002381. F04003.

McKenna Neuman, C. and Nickling, W. (1995). Aeolian sediment flux decay: Non-linear behaviour on developing deflation lag surfaces. *Earth Surface Processes and Landforms*, 20(5):423–435.

McKenna Neuman, C. and Sanderson, S. (2008). Humidity control of particle emissions in aeolian systems. *Journal of Geophysical Research*, 113(F2). doi:10.1029/2007JF000780. F02S14.

Min. V&W (1990). A new coastal defence policy for the netherlands. Rijkswaterstaat.

Namikas, S. L., Edwards, B. L., Bitton, M. C. A., Booth, J. L., and Zhu, Y. (2010). Temporal and spatial variabilities in the surface moisture content of a fine-grained beach. *Geomorphology*, 114:303–310. doi:10.1016/j.geomorph.2009.07.011.

Nickling, W. and McKenna Neuman, C. (1995). Development of deflation lag surfaces. *Sedimentology*, 42(3):403–414.

Nickling, W. G. and Ecclestone, M. (1981). The effects of soluble salts on the threshold shear velocity of fine sand. *Sedimentology*, 28:505–510.

Ojeda, E., Ruessink, B., and Guillen, J. (2008). Morphodynamic response of a two-barred beach to a shoreface nourishment. *Coastal Engineering*, 55(12):1185–1196. doi:10.1016/j.coastaleng.2008.05.006.

Okin, G. S. (2008). A new model of wind erosion in the presence of vegetation. *Journal of Geophysical Research*, 113(F2). doi:10.1029/2007JF000758. F02S10.

Owen, P. R. (1964). Saltation of uniform grains in air. *J. Fluid Mech*, 20(2):225–242.

Peckham, S. D., Hutton, E. W. H., and Norris, B. (2013). A component-based approach to integrated modeling in the geosciences: The design of CSDMS. *Computers and Geosciences*, 53:3–12. doi:10.1016/j.cageo.2012.04.002.

Pye, K. and Tsoar, H. (1990). *Aeolian Sand and Sand Dunes*. Unwin Hyman, London.

Raupach, M., Gillette, D., and Leys, J. (1993). The effect of roughness elements on wind erosion threshold. *Journal of Geophysical Research: Atmospheres*, 98(D2):3023–3029. doi:10.1029/92JD01922.

Reniers, A., Gallagher, E., MacMahan, J., Brown, J., Rooijen, A., Thiel de Vries, J., and Prooijen, B. (2013). Observations and modeling of steep-beach grain-size variability. *Journal of Geophysical Research: Oceans*, 118(2):577–591.

Roelvink, J. A., Reniers, A., van Dongeren, A. P., van Thiel de Vries, J. S. M., McCall, R. T., and Lescinski, J. (2009). Modelling storm impacts on beaches, dunes and barrier islands. *Coastal Engineering*, 56(11):1133–1152. doi:10.1016/j.coastaleng.2009.08.006.

Scheidt, S., Ramsey, M., and Lancaster, N. (2010). Determining soil moisture and sediment availability at white sands dune field, new mexico, from apparent thermal inertia data. *Journal of Geophysical Research*, 115(F2). doi:10.1029/2009JF001378. F02019.

Sherman, D. J., Jackson, D. W., Namikas, S. L., and Wang, J. (1998). Wind-blown sand on beaches: an evaluation of models. *Geomorphology*, 22(2):113–133. doi:10.1016/S0169-555X(97)00062-7.

Sherman, D. J. and Li, B. (2012). Predicting aeolian sand transport rates: a reevaluation of models. *Aeolian Research*, 3(4):371–378. doi:10.1016/j.aeolia.2011.06.002.

Shuttleworth, W. J. (1993). Evaporation. In Maidment, D. R., editor, *Handbook of Hydrology*, pages 4.1–4.53. McGraw-Hill, New York.

Sørensen, M. (2004). On the rate of aeolian sand transport. *Geomorphology*, 59(1):53–62.

Spearman, C. (1904). The proof and measurement of association between two things. *American Journal of Psychology*, 15:72–101. doi:10.2307/1412159.

Stive, M. J. F., de Schipper, M. A., Luijendijk, A. P., Aarninkhof, S. G. J., van Gelder-Maas, C., van Thiel de Vries, J. S. M., de Vries, S., Henriquez, M., Marx, S., and Ranasinghe, R. (2013). A new alternative to saving our beaches from sea-level rise: the Sand Engine. *Journal of Coastal Research*, 29(5):1001–1008. doi:10.2112/JCOASTRES-D-13-00070.1.

Stockdon, H. F., Holman, R. A., Howd, P. A., and Sallenger, A. H. (2006). Empirical parameterization of setup, swash, and runup. *Coastal engineering*, 53(7):573–588. doi:10.1016/j.coastaleng.2005.12.005.

Stout, J. E. (2004). A method for establishing the critical threshold for aeolian transport in the field. *Earth Surface Processes and Landforms*, 29(10):1195–1207.

Tan, L., Zhang, W., Qu, J., Zhang, K., An, Z., and Wang, X. (2013). Aeolian sand transport over gobi with different gravel coverages under limited sand supply: a mobile wind tunnel investigation. *Aeolian Research*, 11:67–74. doi:10.1016/j.aeolia.2013.10.003.

Turpin, C., Badr, T., and Harion, J. L. (2010). Numerical modelling of aeolian erosion over rough surfaces. *Earth Surface Processes and Landforms*, 35(12):1418–1429. doi:10.1002/esp.1980.

Udo, K., Kuriyama, Y., and Jackson, D. W. T. (2008). Observations of wind-blown sand under various meteorological conditions at a beach. *Journal of Geophysical Research*, 113(F4). doi:10.1029/2007JF000936. F04008.

van der Wal, D. (1998). The impact of the grain-size distribution of nourishment sand on aeolian sand transport. *Journal of Coastal Research*, pages 620–631.

van der Wal, D. (2000). Grain-size-selective aeolian sand transport on a nourished beach. *Journal of Coastal Research*, pages 896–908.

van Genuchten, M. T. (1978). Mass transport in saturated-unsaturated media: one-dimensional solutions. Technical Report Research Report No. 78-WR-11, Univ. Princeton, NJ. Water Resources Program.

Van Slobbe, E., De Vriend, H., Aarninkhof, S., Lulofs, K., De Vries, M., and Dircke, P. (2013). Building with nature: in search of resilient storm surge protection strategies. *Natural hazards*, 65(1):947–966. doi:10.1007/s11069-012-0342-y.

Šimůnek, J., Šejna, M., and van Genuchten, M. T. (1998). *The HYDRUS-1D software package for simulating the one-dimensional movement of water, heat, and multiple solutes in variably- saturated media*. International Ground Water Modeling Center, Colorado School of Mines, Golden, Colorado, version 1.0. igwmc - tps - 70 edition. 186pp.

Walstra, D. J. R. (2016). *On the anatomy of nearshore sandbars: a systematic exposition of inter-annual sandbar dynamics*. PhD thesis, Delft University of Technology, Delft. doi:10.4233/uuid:3f86bf04-c6af-486f-b972-bd228d84ebed.

Waterman, R. E. (2010). *Integrated coastal policy via Building with Nature*. TU Delft, Delft University of Technology.

Weng, W. S., Hunt, J. C. R., Carruthers, D. J., Warren, A., and Wiggs, G. F. S. (1991). Air flow and sand transport over sand-dunes. *Acta Mechanica*, 2:1–22.

Wiggs, G. F. S., Baird, A. J., and Atherton, R. J. (2004). The dynamic effects of moisture on the entrainment and transport of sand by wind. *Geomorphology*, 59:13–30. doi:10.1016/j.geomorph.2003.09.002.

Williams, A. T. (1971). An analysis of some factors involved in the depth of disturbance of beach sand by waves. *Marine Geology*, 11(3):145–158. doi:10.1016/0025-3227(71)90003-X.

ACKNOWLEDGMENTS

In the spring of 2012 I was still convinced that I would never engage in a PhD research as it would be too specialized, too enduring and too lonely. Four years later, I learned that an enduring (but hardly lonely) specialization fits me rather well and is an experience I would not want to have missed. Now I'm indebted to Jaap for bringing the NEMO proposal to my attention. To Roos for convincing me to apply for a PhD position after I had been rambling on about the proposal for weeks, apparently. She was also the one that finally made me accept that it was time to wrap up and finish. I thank Jaap and Sierd for their enthusiastic supervision. I thank Marcel for accepting me on the NEMO project and providing me once again with the freedom to explore. I thank Deltares for their generous support in this personal endeavor and Noor and Jolijn for not keeping me up too many nights in the final year of my research.

I have a special memory towards the six week MegaPEX field campaign at the Sand Motor, which was a surrealistic experience that illustrates how a group of overly enthusiastic scientists is able to built a beautiful scientific dataset from a huge pile of sand. Either by Meagan's state-of-the-art equipment that apparently require American-sized *Freedom Poles* for appropriate mounting, or by the elegance of simple solutions to complex problems, like Nick "Topo is My Life" Cohn walking his daily transects accumulating to the equivalent of a proper pilgrimage. I will not easily forget the first time Sierd and I deployed the nails as low-tech measure for micro-topographic changes over a single tidal cycle. Due to unfortunate planning we had to measure and retrieve the first batch of nails (4 cm long, 3 mm thick) in the middle of the night in pitch-dark. Waving our torches over the beach it took us only about a few minutes to find a beautiful array of nails protruding proudly about 1 cm from the bed. Priceless! We learned so much these weeks. I thank the entire MegaPEX team for this exhausting experience, the assistance with our laborious subaerial measurements, the proliferation of American flags at the Sand Motor (U-S-A!) and the free pumpkins.

Except for the six weeks at the Sand Motor, I shared a room at the Faculty of Civil Engineering with my fellow NEMO promovendi Saulo and Bas, and Max, our adopted son from the NatureCoast project. It has been a highly fruitful and challenging environment to work in, despite our research was only superficially related. I much appreciated the discussions on what we all could do in our newly obtained and privileged position: the utter necessity of face recognition in our room, the benefits of having our own 4x4 and the possible improvements to our typical Dutch bread-and-cheese lunch. But soon we found ourselves juggling with an enormous amount of actual scientific ideas, international co-operations, measurement equipment stacked around our desks and an abundance of data. Scientific research appeared to be a very practical daily activity. Discussions started to shift accordingly: how to deploy equipment in the field, how to solder your own measurement devices, what Python package will get the most out of your data and when does data analysis become data torture? Finally, when it occurred to us that the NEMO project had produced more children than papers, the focus shifted once again to finalizing our research. I much

appreciated the weekly papers & coffee meetings with Saulo regarding our writing progress. We both needed it.

As said, these four years appeared not to be so lonely after all. Luckily, since the best ideas arise in conversation. Little pieces that fit together and make you understand. I thank Sierd de Vries, Saulo Meirelles Nunes da Rocha, Max Radermacher, Bas Huisman, Matthieu de Schipper, Martijn Henriquez, Ronald Brouwer, Marcel Stive, Jaap van Thiel de Vries, Bert van der Valk, Ad van der Spek, Arjen Luijendijk, Dano Roelvink, Fedor Baart, Kees den Heijer, Irv Elshoff, Mart Borsboom, Wiepke Jäger, Ad Reniers, Thom Bogaard, Martine Rutten, Susan Steele, Laurens van der Maaten, Thea Vuik, Duncan van der Heul, Lianne van der Weerd, Kathelijne Wijnberg, Leonardo Duarte Campos, Filipe Galiforni Silva, Isaac Williams, Gerben Ruessink, Winnie de Winter, Pam Hage, Yvonne Smit, Jasper Donker, Timothy Price, Maarten Kleinhans, Sebastian Huizer, Marc Bierkens, Corjan Nolet, Joep Keijsers, Ate Poortinga, Michel Riksen, Nick Cohn, Peter Ruggiero, Laura Moore, Orencio Durán, Evan Goldstein, Edie Gallagher, Daniel Buscombe, Andrew Cooper, Irene Delgado-Fernandez, Robert Davidson-Arnott, Tom Barchyn, Giovanni Coco, Gerd Masselink, Bonnie Ludka, Meagan Wengrove, Caroline Fredriksson, Bas Arens, Roeland de Zeeuw, Gideon Maillette de Buy Wenniger, Tom Janssen, Rufus Velhorst, Leon Roessen, Bert Bakker, Jos van Meurs, Henk Tiggeloven, Giel Hermans, Steve van Herk, Sander de Vree, Frank Kalkman, Jaap van Duin and the anonymous reviewers for all the little pieces that made up this thesis.

Bas Hoonhout
Delft, September 2016

CURRICULUM VITAE

PERSONALIA

Bas Hoonhout

26-06-1983, Amsterdam, Nederland

EDUCATION

1995 – 2001	Montessori Lyceum Amsterdam, VWO Natuur & Techniek (1995-2001)
2002 – 2009	Delft University of Technology, MSc Civil Engineering: Dune Erosion along Curved Coastlines (cum laude)

EMPLOYMENT

2001–2009	Freelance web developer
2009–	Deltares

PUBLICATIONS

PEER-REVIEWED ARTICLES

Hoonhout, B. M. and de Vries, S. (2016b). A process-based model for aeolian sediment transport and spatiotemporal varying sediment availability. *Journal of Geophysical Research: Earth Surface*. doi:10.1002/2015JF003692. 2015JF003692.

Hoonhout, B. M. and de Vries, S. (2017a). Aeolian sediment supply at a mega nourishment. *Coastal Engineering*. Submitted.

Hoonhout, B. M. and de Vries, S. (2017b). Field measurements on spatial variations in aeolian sediment availability at the Sand Motor mega nourishment. *Aeolian Research*, 24:93–104. doi:10.1016/j.aeolia.2016.12.003.

Hoonhout, B. M., Radermacher, M., Baart, F., and Van der Maaten, L. J. P. (2015c). An automated method for semantic classification of regions in coastal images. *Coastal Engineering*, 105:1–12. doi:10.1016/j.coastaleng.2015.07.010.

Hoonhout, B. M., Baart, F., and Van Thiel de Vries, J. S. M. (2014a). Intertidal beach classification in infrared images. *Journal of Coastal Research*, SI 66:657–662.

CONFERENCES

Hoonhout, B. M. and de Vries, S. (2016a). Aeolis: A new model for aeolian sediment supply and transport. In *Proceedings of the NCK-days 2016*.

Hoonhout, B. M., Cohn, N., de Vries, S., Roelvink, J. A., Ruggiero, P., Moore, L. J., Durán, O., and Goldstein, E. (2016a). How tides and waves enhance aeolian sediment transport at the Sand Motor. In *Proceedings of the Ocean Sciences Meeting 2016*, New Orleans, USA.

Hoonhout, B. M., de Vries, S., and Cohn, N. (2015a). The influence of spatially varying supply on coastal aeolian transport: a field experiment. In *Proceedings of Coastal Sediments*, San Diego, USA.

Hoonhout, B. M., de Vries, S., and Cohn, N. (2015b). The influence of spatially varying supply on coastal aeolian transport: A field experiment. In *Proceedings of the NCK-days 2015*.

Hoonhout, B. M. and de Vries, S. (2014b). Process-based modeling of supply-limited aeolian transport in coastal environments. In *Proceedings of the International Conference on Aeolian Research 2014*, Lanzhou, China.

Hoonhout, B. M., van Thiel de Vries, J. S. M., Curto, V., and Stive, M. J. F. (2014b). Monitoring supply limiting conditions using imageing techniques. In *Proceedings of the 34th International Conference on Coastal Engineering*, Seoul, Korea.

Hoonhout, B. M. and de Vries, S. (2014a). Modelling and monitoring of meso-scale supply-limited aeolian transport. In *Proceedings of the NCK-days 2014*.

Hoonhout, B. M., de Vries, S., Baart, F., van Thiel de Vries, J. S. M., van der Weerd, L., and Wijnberg, K. M. (2013). Monitoring of beach surface properties with remote sensing. In *Proceedings of Coastal Dynamics*, Arcachon, France.

Hoonhout, B. M. (2013). Monitoring the process of aeolian transport. In *Proceedings of the NCK-days 2013*.

Hoonhout, B. M. and van Thiel de Vries, J. S. M. (2012). Modeling dune erosion, overwash and inundation of barrier islands. In *Proceedings of the 33rd International Conference on Coastal Engineering*, Santander, Spain.

Hoonhout, B. M. and den Heijer, C. (2010). Reliability of dune erosion assessment along curved coastlines. In *Proceedings of the 32nd International Conference on Coastal Engineering*, Shanghai, China.

SOFTWARE AND DATA

Hoonhout, B. M. (2016b). Aeolis v1.1: A process-based model for simulating availability-limited aeolian sediment transport. GIT repository. doi:10.5281/zenodo.58854.

Hoonhout, B. M. (2016a). Aeolis model setups v2.0. GIT repository. doi:10.5281/zenodo.58837.

Hoonhout, B. M., de Vries, S., and Cohn, N. (2016b). Field measurements on aeolian sediment transport at the Sand Motor mega nourishment during the MegaPeX field campaign. OpenDAP server. doi:10.4121/uuid:3bc3591b-9d9e-4600-8705-5b7eba6aa3ed.

Hoonhout, B. M. and Radermacher, M. (2015b). Flamingo: a coastal image analysis toolbox. GIT repository. doi:10.5281/zenodo.14596.

Hoonhout, B. M. and Radermacher, M. (2015a). Annotated images of the dutch coast. FTP server. doi:10.4121/uuid:08400507-4731-4cb2-a7ec-9ed2937db119.

COLOPHON

Measurement data presented in this thesis is open-source and can be obtained through the 4TU.ResearchData initiative at:
data.4tu.nl
The AEOLIS model presented in this thesis is open-source and can be obtained through the OpenEarth GitHub repository at:
github.com/openearth/aeolis-python/
The model schematizations presented in this thesis are open-source and can be obtained through the OpenEarth GitHub repository at:
github.com/openearth/aeolis-models/
The technical documentation of the AEOLIS model can be found at:
aeolis.readthedocs.io
All scripts that are used for analysis of measurement data, model setup and the generation of figures and tables, including an ANSIBLE playbook that generates this thesis from raw data, are published through the author's private GitHub repository at:
github.com/hoonhout/phd/

This document was typeset using the typographical look-and-feel `classicthesis` developed by André Miede.